15/3-14-96 J-SC1

DOE/BC/14897-10
(DE96001216)

ANISOTROPY AND SPATIAL VARIATION OF RELATIVE PERMEABILITY AND LITHOLOGIC CHARACTER OF TENSLEEP SANDSTONE RESERVOIRS IN THE BIGHORN AND WIND RIVER BASINS, WYOMING

Annual Report for the Period
October 1, 1994 to September 30, 1995

By
Thomas L. Dunn

March 1996

Performed Under Contract No. DE-AC22-93BC14897

The University of Wyoming
Laramie, Wyoming

Bartlesville Project Office
U. S. DEPARTMENT OF ENERGY
Bartlesville, Oklahoma

DOE/BC/14897-10
Distribution Category UC-122

Anisotropy and Spatial Variation of Relative Permeability and Lithologic Character of Tensleep Sandstone Reservoirs in the Bighorn and Wind River Basins, Wyoming

Annual Report for the Period
October 1, 1994 to September 30, 1995

By
Thomas L. Dunn

March 1996

Work Performed Under Contract No. DE-AC22-93BC14897

Prepared for
U.S. Department of Energy
Assistant Secretary for Fossil Energy

Robert Lemmon, Project Manager
Bartlesville Project Office
P.O. Box 1398
Bartlesville, OK 74005

Prepared by
The University of Wyoming
P.O. Box 4068
Laramie, WY 82071-4068

List of Figures 1

List of Tables 3

TASK 1.0 - REGIONAL FRAMEWORKS.
M. Crabaugh, Task Leader 6
OBJECTIVES 6
INTRODUCTION 6
OREGON BASIN NORTH DOME STUDY 9
Objectives 9
Methods 9
Results to Date 10
FLOW UNIT CHARACTERIZATION 10
STRATIGRAPHIC AND PALEOGEOGRAPHIC BACKGROUND 14
TENSLEEP DEPOSITIONAL MODEL 17
CONTROLS ON RESERVOIR HETEROGENEITY 20
Accumulation Processes 21
Conclusions: Effects of Accumulation Processes on Reservoir Heterogeneity 28
Preservation Processes 34
Conclusion: Effects of Preservation Processes on Reservoir Heterogeneity 34
FUTURE PLANS 36

TASK 2.0 - RELATIVE PERMEABILITY MEASUREMENTS.
W. Iverson, Task Leader 38
OBJECTIVES 38
RELATIVE PERMEABILITY MEASUREMENTS 38
Introduction 38
Measured Data 41
Interpretation of Results 45
Summary 49
Future Plans 50
RESERVOIR SIMULATION 50
Introduction 50
Curve Fitting 51
Buckley-Leverett Simulator 54
Summary 59
Future Plans 59
RELATIVE PERMEABILITY AND IMAGE ANALYSIS 60
SUMMARY 62

TASK 3.0 - CO_2 FLOOD - FORMATION ALTERATION AND WELLBORE DAMAGE.
R. Shiraki, Task Leader 65
OBJECTIVES 65
FUTURE PLANS 66
FORMATION WATER CHEMISTRY 67
(1) Tensleep Formation water chemistry 67
(2) Tensleep Formation water chemistry at Teapot Dome oil field 75
(3) Madison Formation water chemistry 78
(4) Phosphoria Formation water chemistry 83
COMPUTER SIMULATION OF ARAGONITE SCALE FORMATION DUE TO CO_2 FLOODING 86
Aspects of CO_2 -flooding 86
Method of simulation 89
Results and Discussion 91
CO_2 CORE-FLOODING EXPERIMENT 96

Experimental 97
Results and Discussion 98

TASK 4.0 - PROJECT MANAGEMENT AND TECHNICAL TRANSFER.
T. Dunn, Task Leader **108**
OBJECTIVES 108

REFERENCES **110**

List of Figures

Task 1.0

Figure 1. Schematic drawing of well-bore superimposed on outcrop photo
Figure 2. Location map of North Oregon Basin study
Figure 3. Core description of Gov't Tract 3B #8
Figure 4. FMS log of Gov't Tract 3B #8
Figure 5. Location map of data sources for the Tensleep
Figure 6. Mississippian through Permian correlation
Figure 7. Idealized Upper Tensleep eolian-marine cycle
Figure 8. Generalized Pennsylvanian to Early Permian paleogeography
Figure 9. Tensleep depositional model
Figure 10. Tensleep cycles related to sequence stratigraphic terminology
Figure 11. Illustration of bedform dynamics
Figure 12. Scaled drawings of outcrop photomosaics
Figure 13. Schematic drawing of internal eolian stratification
Figure 14. Photograph of annual cycles bounded by third-order surfaces
Figure 15. Scaled drawing of a portion of the Alkali Flats outcrop
Figure 16. Idealized compound crescentic bedform for the Tensleep Sandstone
Figure 17. Modern analog for the Tensleep bedforms
Figure 18. Tensleep flow-unit dimensions
Figure 19. Bounding surface photographs
Figure 20. West-east cross-section across the Bighorn Basin
Figure 21. Comparison of core description with petrophysical characteristics

Task 2.0

Figure 22. Relative permeability curves computed for Sample A
Figure 23. Ratio of water to oil permeabilities plotted against water saturation
Figure 24. Ratio of permeabilities taken at water breakthrough saturations
Figure 25. Gas permeabilities for each Tensleep sample
Figure 26. Fraction oil produced before water breakthough
Figure 27. Relative permeability versus dimensionless water saturation
Figure 28. Assumed relative permeability curves input to Buckley-Leverett simulator
Figure 29. Oil production versus time output
Figure 30. WOR versus time.
Figure 31. Schematic diagram showing relative permeability sampling scheme
Figure 32. Graph showing effects of grain plucking no pore-size distribution

Task 3.0

Figure 33. Chemical composition of Tensleep Formation waters
Figure 34. Ca versus SO_4 for types A1 and A2 of Tensleep waters
Figure 35. Mg versus SO_4 for types A1 and A2 of Tensleep waters
Figure 36. HCO_3 versus SO_4 for types A1 and A2 of Tensleep waters
Figure 37. Na + K vesus SO_4 for types A3 and B of Tensleep waters
Figure 38. Distribution of Tensleep waters in the Bighorn Basin

Figure 39. Chemical composition of Tensleep and Madison waters at Teapot Dome
Figure 40. Chemical composition of Madison Formation waters
Figure 41. Ca or Mg versus SO_4 for types A1 and A2 of Madison waters
Figure 42. HCO_3 versus SO_4 for types A1 and A2 of Madison waters
Figure 43. Distribution of Madison waters in the Bighorn Basin
Figure 44. Chemical composition of Phosphoria Formation waters
Figure 45. Na + K vesus SO_4 for types A3 and B of Phosphoria waters
Figure 46. Distribution of Phosphoria waters in the Bighorn Basin
Figure 47. Histograms of total dissolved solids for Tensleep, Madison and Phosphoria formations
Figure 48. Schematic representations of well-to-well CO_2 flooding and pressure profile
Figure 49. Saturation index of dolomite as a function of P_{CO2}
Figure 50. Saturation index of aragonite as a function of P_{CO2}
Figure 51. Relation between P_{CO2} at which solution becomes saturated with respect to aragonite and the amount of dolomite dissolved.
Figure 52. Concentrations of Ca, Mg, and SO_4 vs. reaction time of CO_2
Figure 53. pH and concentration of SiO_2 and K vs. reaction time of CO_2
Figure 54. Saturation indices of dolomite, anhydrite, and quartz vs. reaction time of CO_2
Figure 55. Saturation indices of celestite and barite vs. reaction time of CO_2
Figure 56. Change of saturation index of dolomite through CO_2 core flooding
Figure 57. Change of saturation index of aragonite through CO_2 core flooding

List of Tables

Task 2.0

Table 1. Relative permeability sample status
Table 2. Buckley-Leverett simulator sample
Table 3. List of samples taken for relative permeability studies in the second year
Table 4. List of samples taken for image analysis studies

Task 3.0

Table 5. Saturation index of minerals for Tensleep and Madison water at Teapot Dome
Table 6. Chemical composition of Tensleep waters used in simulation
Table 7. Thermodynamic data for speciation at 80°C
Table 8. Chemical composition of nutrient solutions used in CO_2 experiment
Table 9. Porosity and permeability of samples before and after CO_2 experiment

EXECUTIVE SUMMARY

Background

Permeability variations in reservoirs include the spatial variation (heterogeneity) of absolute and relative permeability and the directional variation (anisotropy) of absolute and relative permeability. Absolute permeability has been extensively studied by other research teams in academia and the petroleum industry. However, relative permeability anisotropy and spatial variations have yet to be considered as to the effects on oil and gas production. The principal focus of this project is to evaluate the importance of relative permeability anisotropy with respect to other known geologic and engineering production concepts.

This research is to provide improved strategies for enhanced oil recovery from the Tensleep Sandstone oil reservoirs in the Bighorn and Wind River basins, Wyoming. The Tensleep Sandstone contains the largest potential reserves within reservoirs which are candidates for EOR processes in the State of Wyoming. Although this formation has produced billions of barrels of oil, in some fields, as little as one in seven barrels of discovered oil is recoverable by current primary and secondary techniques. Because of the great range of °API gravities of the oils produced from the Tensleep Sandstone reservoirs, the proposed study concentrates on establishing an understanding of the spatial variation and anisotropy of relative permeability within the Tensleep Sandstone. This research will associate those spatial distributions and anisotropies with the depositional subfacies and zones of diagenetic alteration found within the Tensleep Sandstone.

The associations between depositional lithofacies, diagenetic alteration, and pore geometry will strongly link relative permeability with the distinct and measurable dimensions of lithofacies and authigenic mineral facies. Hence, the study is to provide criteria for scaling this parameter on a range of scales — from the volume of laboratory investigation to the basin-wide scale of subfacies distribution. Effects of both the depositional processes and the burial diagenesis will be investigated. Image analysis of pore systems will be performed so as to produce algorithms for estimating relative permeability from petrographic analyses of core and well cuttings.

In addition, these studies are being coupled with geochemical modeling and coreflood experiments to investigate the potential for wellbore scaling and formation damage anticipated during EOR processes (e.g., CO_2 flooding). This multidisciplinary project will provide a regional basis for EOR strategies which can be clearly mapped and efficiently applied to the largest potential target reservoir in the State of Wyoming. Additionally, the results of this study have application to all eolian reservoirs through the correlations of relative permeability variation and anisotropy with eolian depositional lithofacies.

Results

The second year of the project has included the efforts of eleven individuals working on three research tasks and one administrative task. Discussions of the accomplishments of each of the tasks can be found in the sections which follow. There are six principle accomplishments which the work has demonstrated:

1) Anisotropy in relative permeability has been consistently observed in the subsurface and outcrop Tensleep samples examined.

2) The development of the regional depositional framework has produced a sequence stratigraphic relationship between reservoir quality and preservation (sea-level rise) processes.

3) We have applied our process-oriented approach to help optimize production for a horizontal well infill drilling program in the Bighorn Basin.

4) We observe air permeability anisotropy only in subsurface samples. This difference is the result of diagenetic alteration.

5) The regional Tensleep water chemistry variation is clearly related to variable mixing and flushing from Laramide related meteoric recharge.

6) The potential for carbonate mineral scale and formation damage which could accompany CO_2 treatment is not strongly influenced by the observed regional formation water chemistry. Sulfate mineral scale and formation damage potential is currently being investigated.

TASK 1.0 - REGIONAL FRAMEWORKS.

Mary Crabaugh - Task Leader

OBJECTIVES

This research will associate spatial distribution and anisotropy of relative permeability with the depositional subfacies and zones of diagenetic alteration found within the Tensleep Sandstone. The associations between depositional lithofacies, diagenetic alteration, and pore geometry will link relative permeability with the distinct and measurable dimensions of lithofacies and with authigenic mineral facies. Effects of the depositional processes and burial diagenesis will be investigated.

INTRODUCTION

The primary objective of this task is to define the geometries of the reservoir flow-units occurring in the Tensleep Sandstone, and to place them into a regional depositional model that can be used as a predictive tool to increase oil recovery. Because these compartments have a distinct asymmetry—their long axis is parallel to the crestline of the bedforms and their short axis perpendicular to the crestline—this study has immediate application to horizontal well completions. Figure 1 is a scaled drawing of a horizontal well trace superimposed on an outcrop photomosaic illustrating how a horizontal well drilled perpendicular to the crestline of the bedform would encounter as many flow-unit compartments as possible.

There have been 12 horizontal wells drilled in the Tensleep in the Bighorn Basin over the past year, which is a significant increase over past years. Horizontal wells are actively being pursued as a means to optimize the amount of the well-bore in contact with productive portions of the Tensleep Sandstone. Marathon Oil Co., which is a cost-share partner on the contract, is currently drilling a series of horizontal wells in the North Dome of Oregon Basin. As a part of the subsurface study of the Tensleep, a detailed study is underway utilizing core and FMS (Formation MicroScanner) and FMI (Formation MicroImager) log data in the area surrounding the horizontal well completions (Figure 2).

Lateral Flow Compartmentalization Defined by Erosional Bounding Surfaces

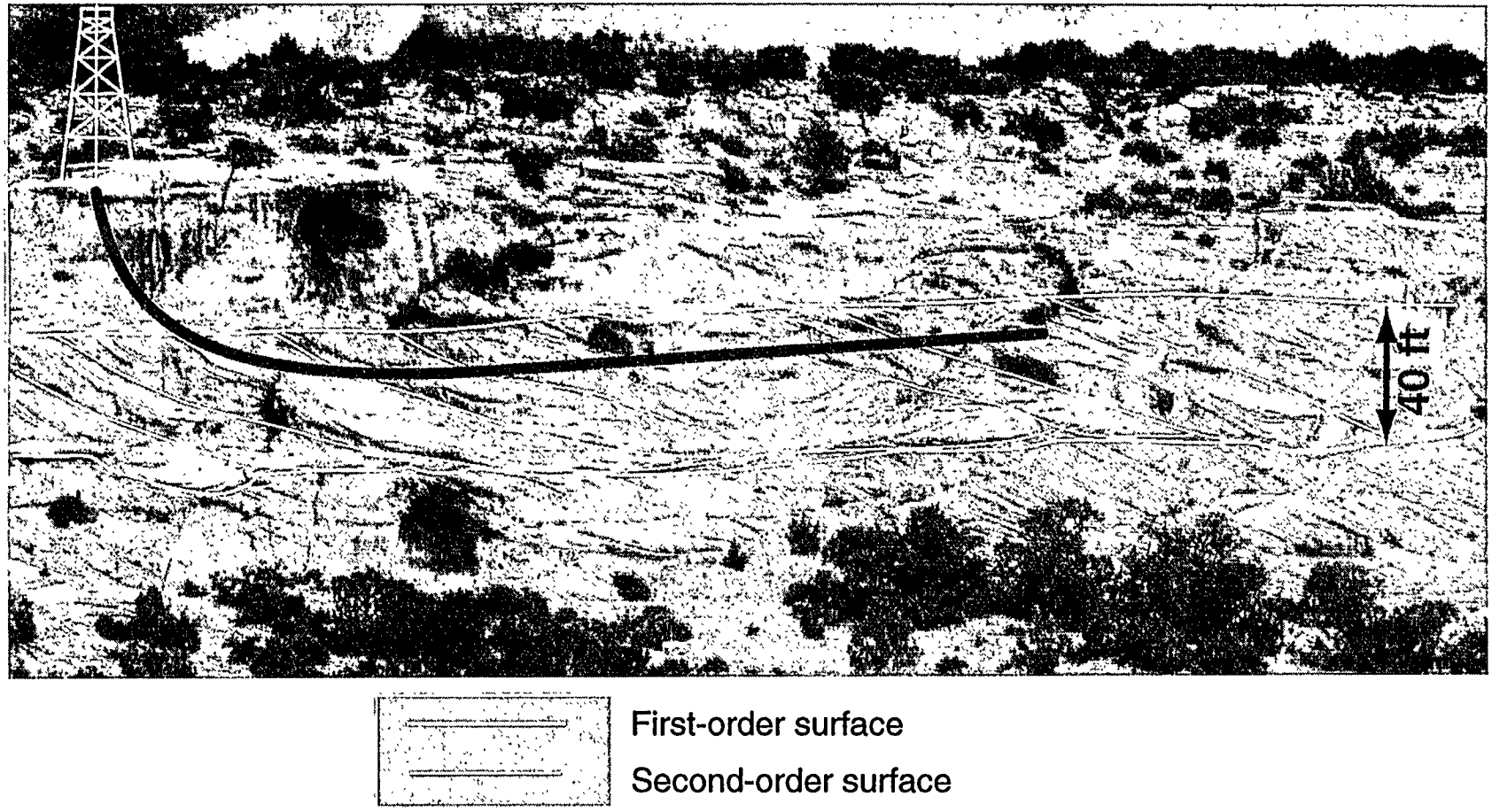

Figure 1. Schematic drawing of a horizontal borehole superimposed on a photo of the Alkali Flats outcrop (Fig. 5). Borehole penetrates a series of compartments created by accumulation processes during Tensleep formation.

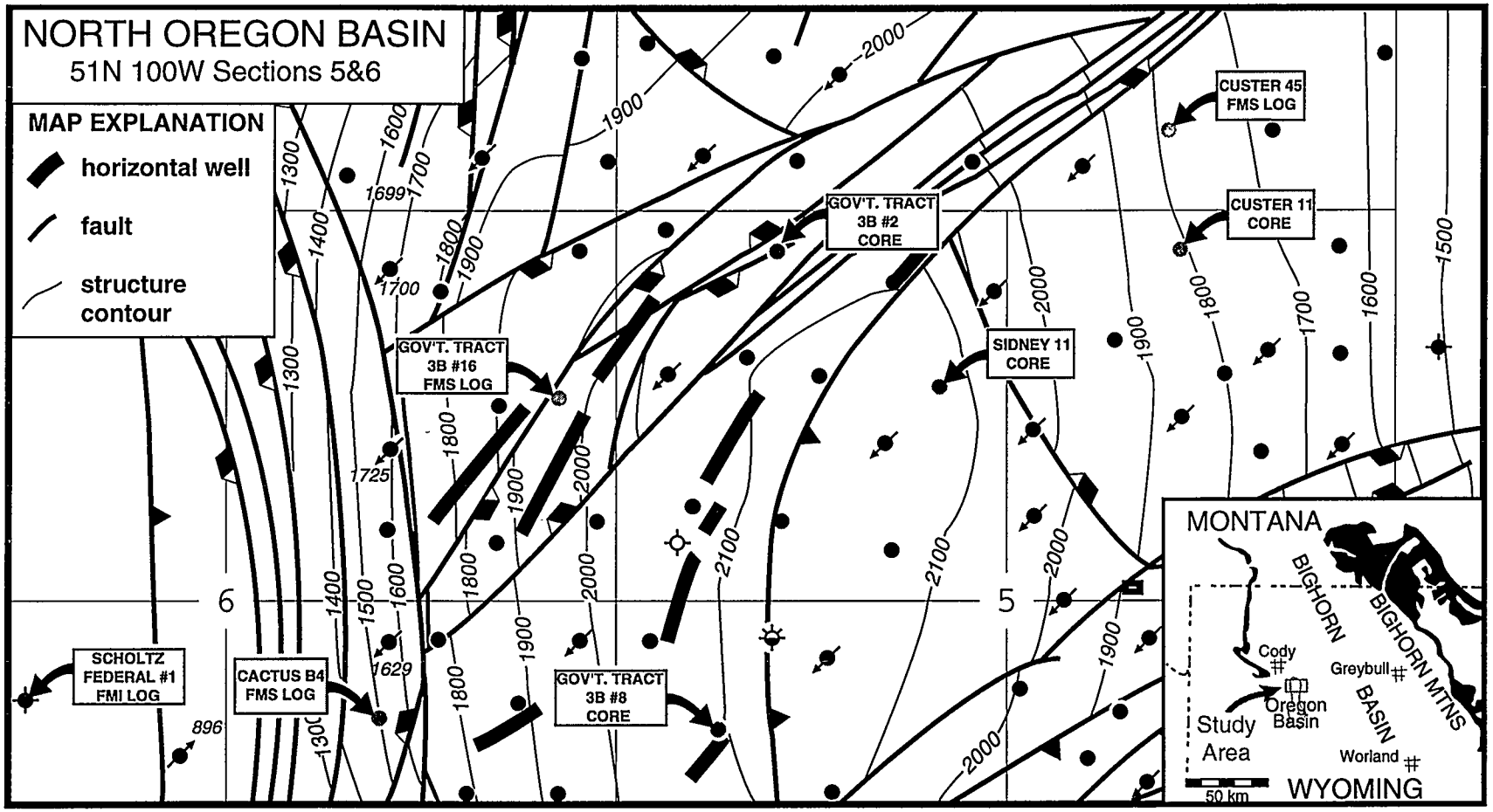

Figure 2. Map of core and well log locations to be used in the North Oregon Basin field study. The Oregon Basin field is located on the western side of the Bighorn Basin.

OREGON BASIN NORTH DOME STUDY

Objectives

Because of the compartmentalization and directional permeability associated with the compound cross-strata of the Tensleep Sandstone, Marathon Oil Co. considers that horizontal wells are the key to incremental oil recovery in the Tensleep. To help direct future drilling efforts, an improved understanding of these directional characteristics is needed. This will be accomplished through a synthesis and analysis of the existing core and FMS database. Improved quantification of the reservoir flow-units will also provide improved input into ongoing STRATAMODEL simulations.

Methods

Three to four closely spaced cores are to be described and correlated with three FMS and one FMI log (Figure 2). The FMS and FMI logs allow interpretation of the sandstone depositional facies as well as determination of the orientation of the cross-strata within cross-stratified units. This detailed information will allow more precise interpretation of the type of facies affecting reservoir quality than would normally be allowed by standard electric logs. In the description of the core, emphasis is being placed on distinguishing marine carbonates from tightly cemented interdune accumulations. The core descriptions as well as the FMI and FMS logs will potentially allow identification of first-, second-, and third-order erosional bounding surfaces which will facilitate interpretation of flow-unit geometry. The core and log description are to be tied into a grid of cross-sections.

Results to Date

As of October 1995, the Gov't Tract 3B #8 and Sidney #11 cores as well as the Gov't Tract 3B #16 FMS and Scholtz Federal #1 FMI logs have been described. Comparison of the core and the FMS log indicate that the highest permeability zones are associated with disturbed zones, while the more compartmentalized "C" sand has overall lower permeabilities (Figure 3). The correlation also indicates that some of the tight zones thought to be lithologically controlled are actually associated with cement-filled fractures. The FMS and FMI logs have made it possible to delineate the thickness of flow-units bounded by erosional surfaces in the subsurface and to distinguish bounding surface types (Figure 4). Additional core and log description will clarify the small- scale and large-scale compartmentalization occurring in the subsurface of North Oregon Basin.

FLOW UNIT CHARACTERIZATION

The spatial dimensions of the Tensleep Sandstone fluid-flow units have been defined, and these units have been sampled in order to distinguish their relative permeability characteristics. This has been accomplished through the integration of surface and subsurface data in the Wind River and Bighorn basins. As of October 1995, the Tensleep well log database in Production Analyst© for the Bighorn and Wind River basins at the Institute for Energy Research has expanded to 330 wells and 80 core analyses. This database now consists of 8,000 feet of core analysis, and approximately 112,000 feet each of the digitized well logs (GR, Neu, Den) (Figure 5). In addition, 11 cores covering the entire Bighorn Basin have been described and integrated into the subsurface correlations.

Field work in the summer of 1995 (28 days, 2 person field party) was conducted in the mountains surrounding the Wind River Basin, and was concentrated on outcrops in the Wind River Mountains. A series of five sections were examined along the length of the Wind River Mountains (Figure 5). The study involved measuring and describing three vertical sections and the construction and detailed descriptions of six photomosaics. This

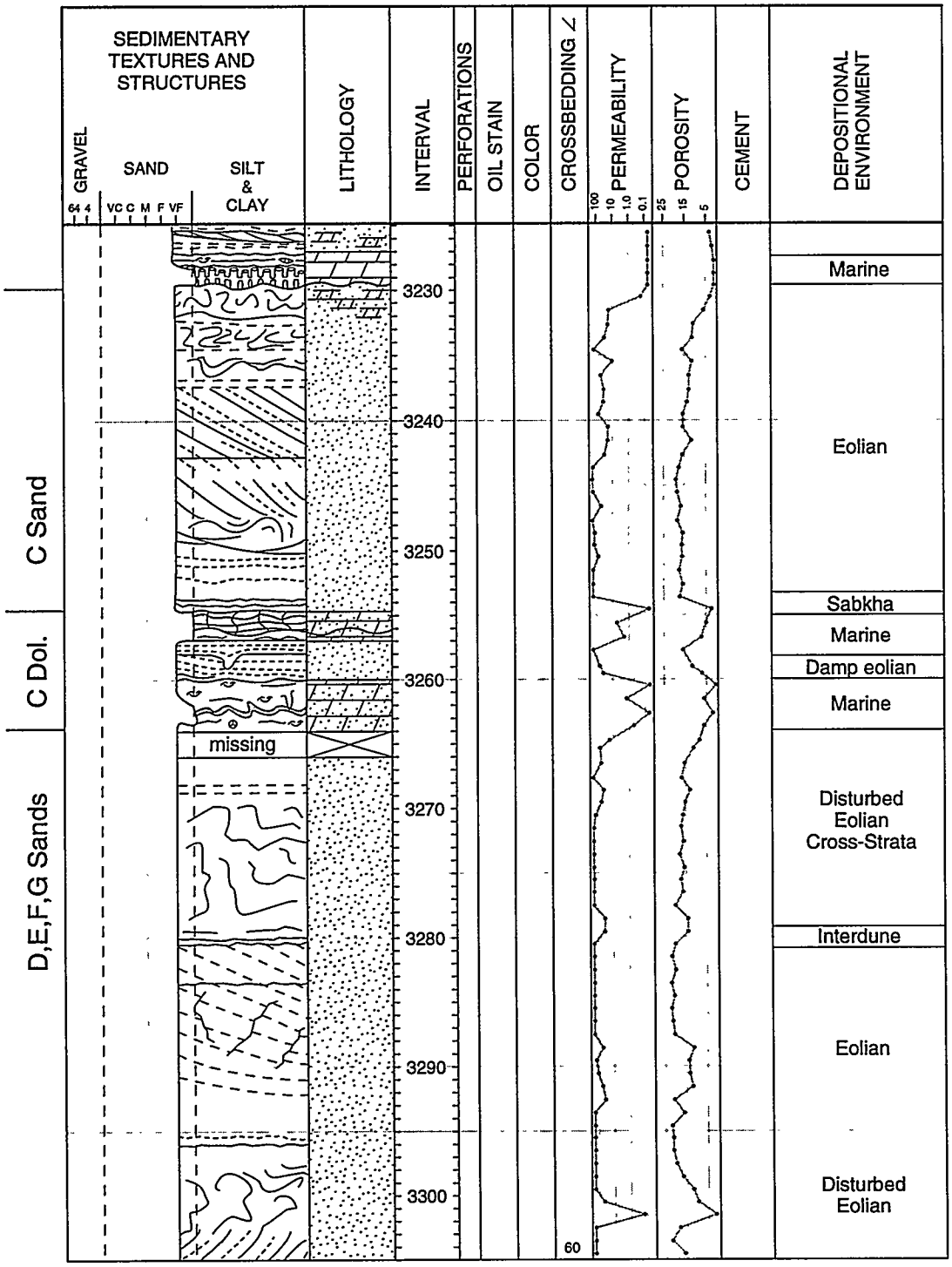

Figure 3. Core description of Gov't Tract 3B #8, indicating that the areas that show disturbed cross-strata in the D,E,F,G sands have higher permeability on average than the well-stratified C sand.

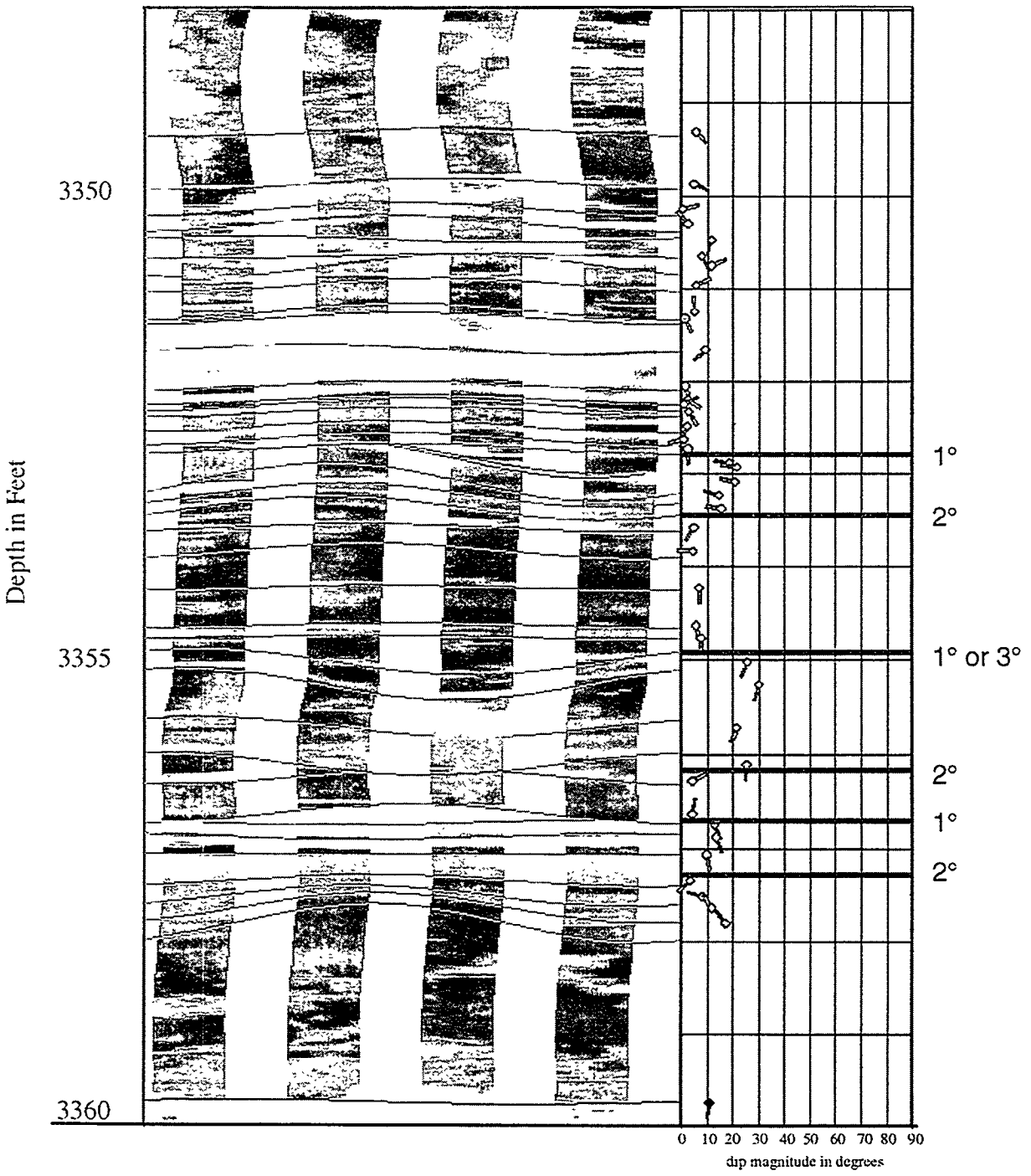

Figure 4. FMS log from the Gov't Tract 3B #8, well with lines tracing the intersection of foresets with the borehole. The green tadpoles indicate the direction and dip magnitude of the foresets. 1°, 2°, and 3° represent the interpretation of the type of erosional bounding surfaces occuring at that depth. These surfaces would inhibit fluid flow.

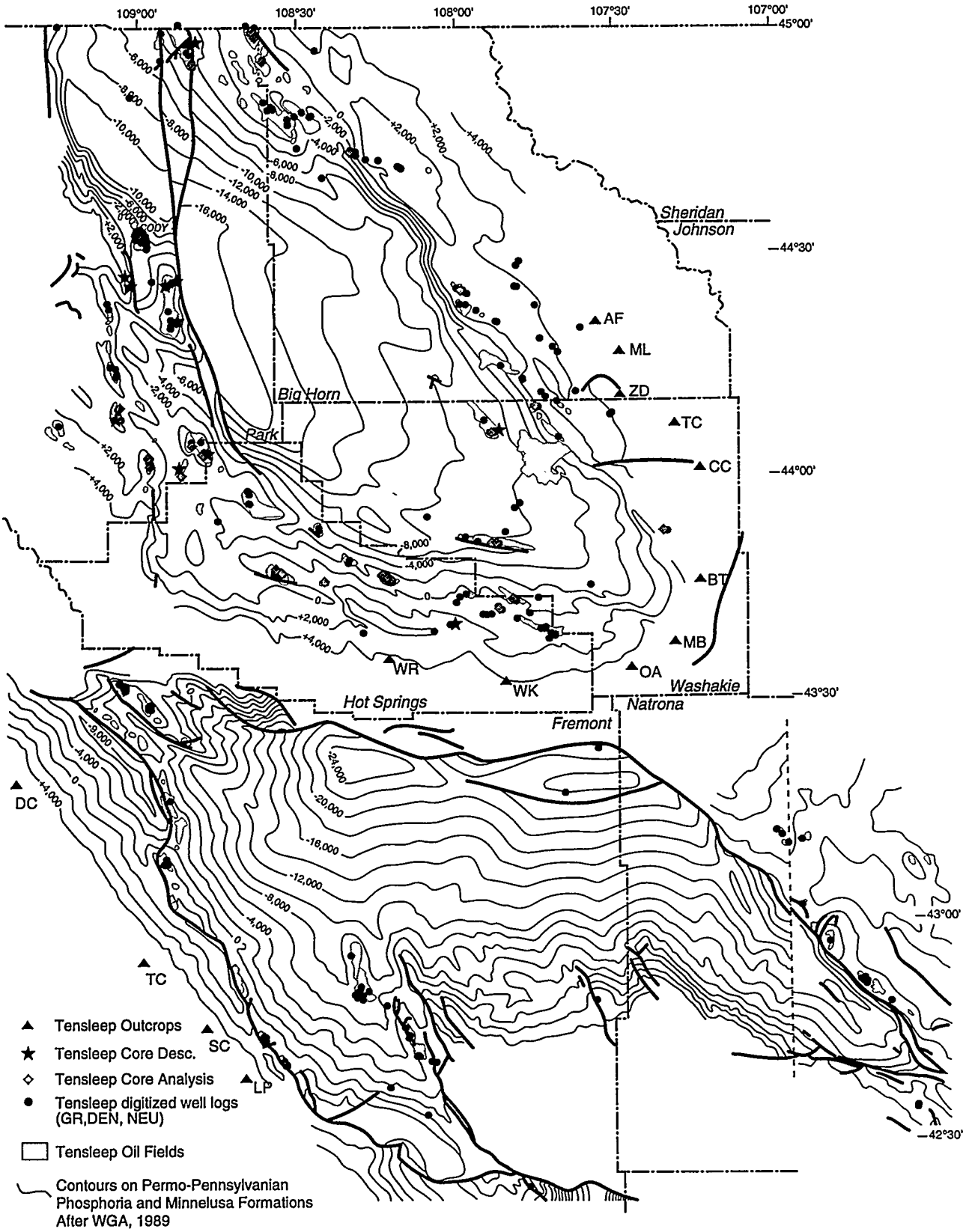

Figure 5. Location of Tensleep oil fields and digitized well log and core analyses for the Bighorn and Wind River basins as of October 15, 1995. Section and photomosaic locations: AF=Alkali Flats, ML=Medicine Lodge, ZD=Ziesman Dome, TC= Tensleep Canyon, CC= Canyon Creek, BT=Big Trails, MB=Mohagany Butte, OA=Orchard Anticline, WK= West Kirby Creek, WR=Wind River Canyon, LP=Little Popo Agie Canyon, SC=Sinks Canyon, TC=Trout Creek, and DC=Dinwoody Canyon.

study has confirmed that the style of stratification observed in the Wind River Mountains is consistent with that observed in the Bighorn Mountains. Use of the photomosaics, which conjunction with extend to over 2500 feet laterally, to quantify the lateral variability of flow units in horizontal well plays drilled in 1995 in the western Bighorn Basin has proved fruitful. In conjunction with the description and interpretation at the outcrop, samples were taken in Tensleep outcrops of both the Bighorn and Wind River Mountains for relative permeability study and pore geometry evaluation of bounding surfaces.

STRATIGRAPHIC AND PALEOGEOGRAPHIC BACKGROUND

The Tensleep Sandstone is Middle Pennsylvanian (Desmoinesian) to Lower Permian (Wolfcampian) in age—primarily on the basis of fusulinids (Branson, 1939; Henbest, 1954, 1956; and Verville, 1957) and corroborated by brachiopod (Brainerd and Keyte, 1927; Hoare and Burgess, 1960) and conodont studies (Rhodes, 1963) (Figure 6). Verville et al., (1970) also demonstrated differential truncation of the Tensleep along the eastern flank of the southern Bighorn Mountains, with Wolfcampian strata exposed at the top of the Tensleep in southern areas and Desmoinesian strata exposed at the top in the northern areas. Differential erosion across the top of the Tensleep Sandstone in the Bighorn Basin, resulting in significant variations in unit thickness, has also been demonstrated through physical stratigraphic relationships by Wheeler (1986), Kerr et al. (1986), and Kerr (1989).

The Tensleep has been informally divided into lower and upper units using the top of a widespread fusulinid, coral-bearing, dolomitic sandstone, following the method of Agatston (1952, 1954) and Wheeler (1986). This sandstone is recognized in well logs as a high density, low porosity bed that separates the serrated porosity and gamma-ray log signature of the lower Tensleep from the more blocky signature of the upper Tensleep. The upper Tensleep eolian-marine cycles are composed of compound sets of eolian cross-strata gradationally overlain by sandy to fossiliferous dolomites capped by a sharp to erosional

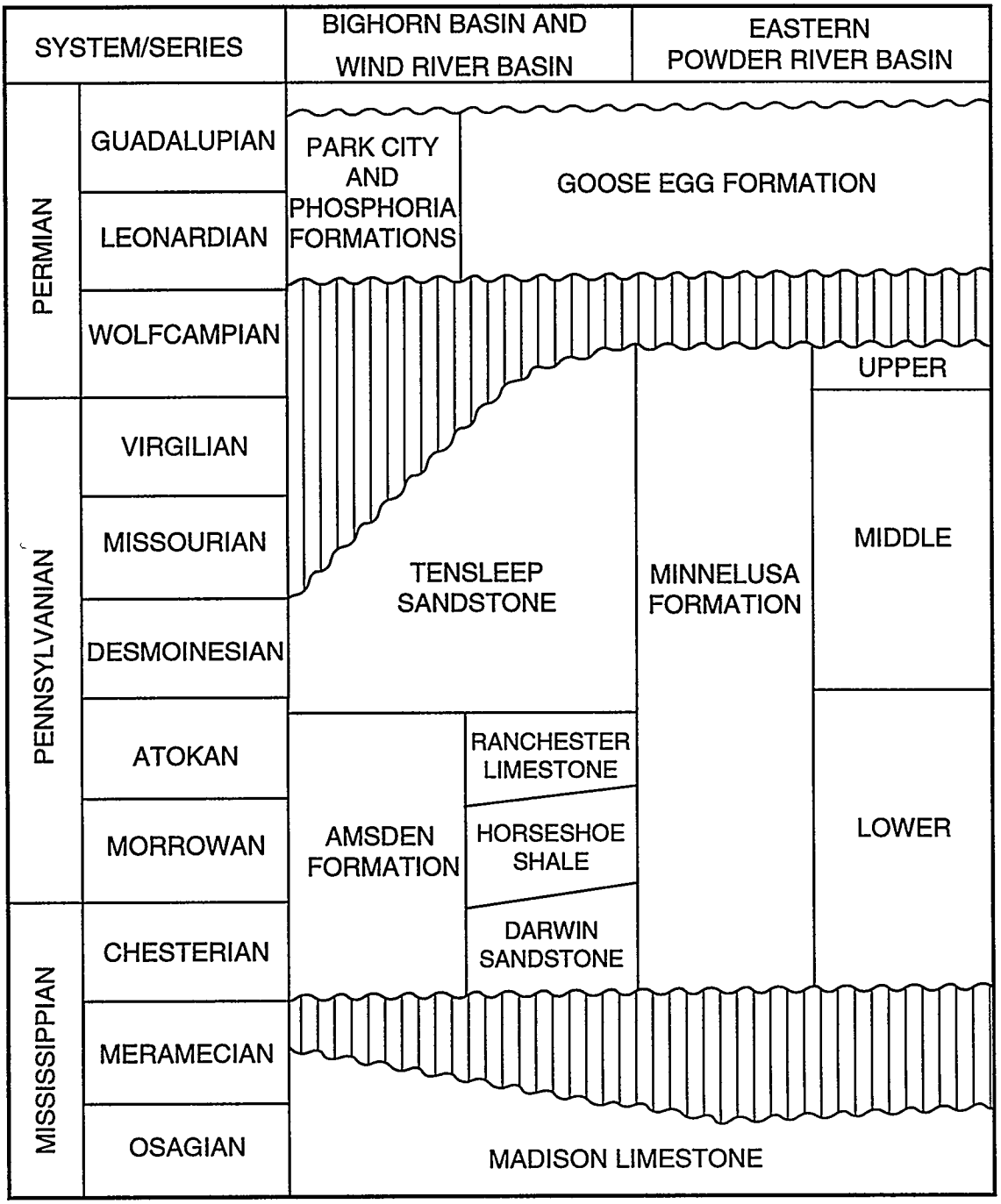

Figure 6. Correlation chart showing Mississippian throught Permian units in the Bighorn and Wind River basins. After Wheeler (1986).

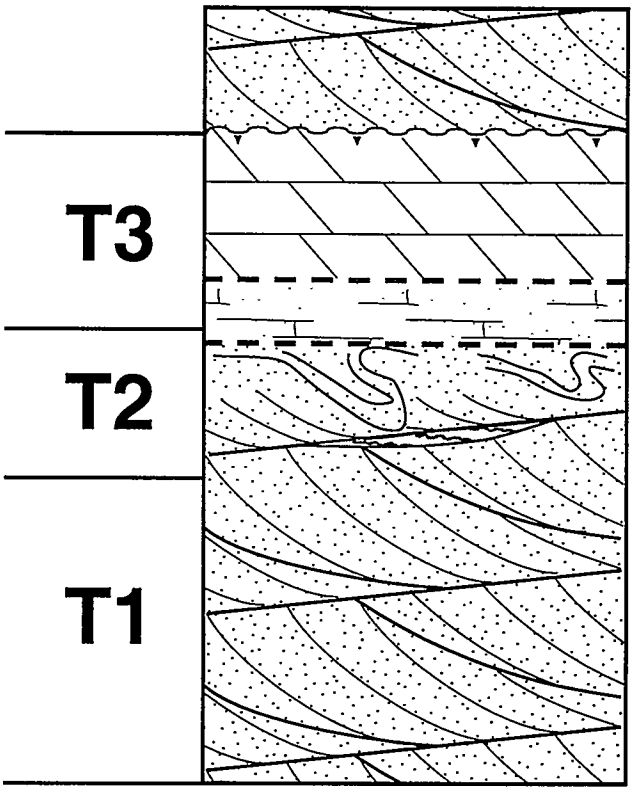

Figure 7. Idealized Upper Tensleep eolian-marine cycle. Eolian sandstone accumulation shows a thin, discontinuous interdune accumulation toward the top. The eolian sands are gradationally overlain by sandy marine dolomites, which are capped by an erosional surface. The labels T1, T2 and T3 correspond to time slices illustrated in Figure 9.

contact (Figure 7). The Tensleep eolian units of the Bighorn and Wind River basins are characterized by very fine to fine sandstones with varying amounts of quartz, dolomite and anhydrite cements.

Figure 8 illustrates the general paleogeography for the Late Pennsylvanian to Early Permian during sea-level lowstand. The study area was at approximately 10° north latitude during accumulation of the Tensleep Sandstone (Scotese et al., 1979). Paleocurrent measurements from eolian cross-strata indicate a predominance of southwest dips. This corresponds well with paleowindflow reconstructions for this time period shown in Figure 8, which indicate that winds out of the present day north and northeast were dominant

(Parrish and Peterson, 1988; Peterson, 1988). The global circulation models of Parrish and Peterson (1988) also indicate a monsoonal climate that had annual fluctuations in wind direction such that the summer winds were northerly and the winter winds were northeasterly.

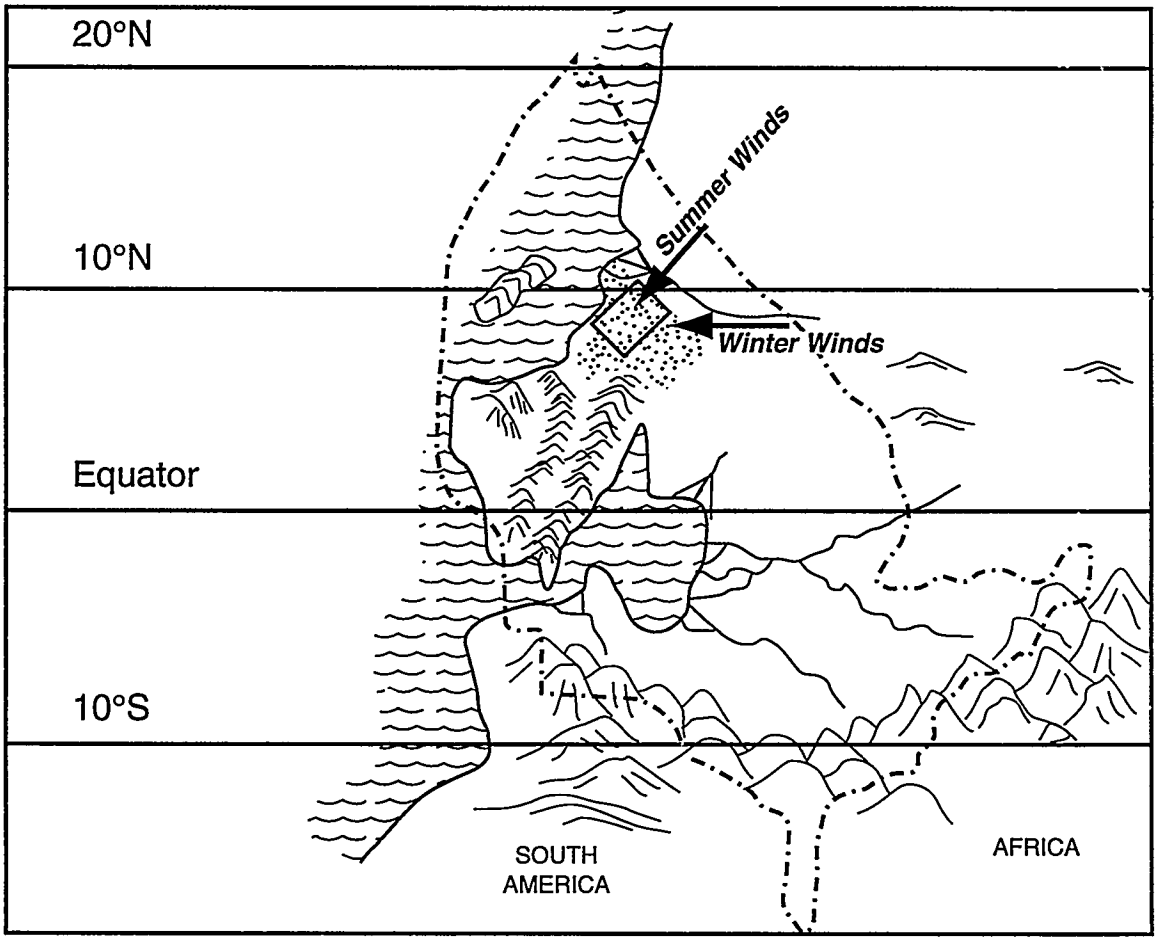

Figure 8. Generalized Pennsylvanian to Early Permian paleogeography during a low sea-level stand. Stipple pattern indicates area of eolian development. Arrows depict paleowind directions from Parrish and Peterson (1988). Modified from Kerr and Dott, 1988. Dashed line indicates United States border.

TENSLEEP DEPOSITIONAL MODEL

The accumulation and preservation dynamics of the Tensleep eolian system heavily influenced the development of the subsurface Tensleep Sandstone reservoirs. In eolian

systems, accumulation of sediments and their subsequent preservation can result from completely independent processes. Accumulation represents the net deposition of sediment through time resulting in a three-dimensional body of sediment (Kocurek and Havholm, 1993). Preservation refers to the placing of an accumulation below some regional baseline of erosion. Accumulation of the Tensleep Sandstone occurred in a dry eolian system, that is, one in which the water table is at a depth below the sediment surface such that it has no stabilizing influence on the sediment, and that accumulation therefore takes place strictly for aerodynamic reasons (Kocurek and Havholm, 1993). Regional relative sea-level rise resulted in flooding of this broad shelf and placed the Tensleep eolian system below the regional baseline of erosion resulting in its preservation. Figure 9 illustrates the accumulation and preservation processes that influenced the formation of the Tensleep Sandstone.

The sandstone-dolomite cycles of the Tensleep are related to regional fluctuations in the relative sea level. Time 1 in Figure 9 depicts a time shortly after initial sea-level fall and the development of a dry eolian system with bedforms migrating to the southwest. As the bedforms migrated and climbed they produced an accumulation of cross-stratified lee-face deposits. The local water table was well below the depositional surface and did not affect the depositional processes of the eolian system. As relative sea level began to rise, it caused the local water table to rise as well. As the local water table rose, it began to encounter the deepest portions of the interdune areas and formed wavy bedded interdune deposits (Time 2, Figure 9). (In outcrop the interdune deposits are lens-shaped and laterally discontinuous.) With continued relative sea-level rise the eolian system was flooded and reworked by the marine environment (Time 3, Figure 9). Marine flooding commonly resulted in soft-sediment deformation of the upper eolian units. Following flooding of the shelf, the marine system deposited sandy, fossiliferous carbonates, which overlie the eolian sandstones. Subsequent relative sea-level fall resulted in exposure of the marine sediments and the formation of an erosional surface that capped the cycle.

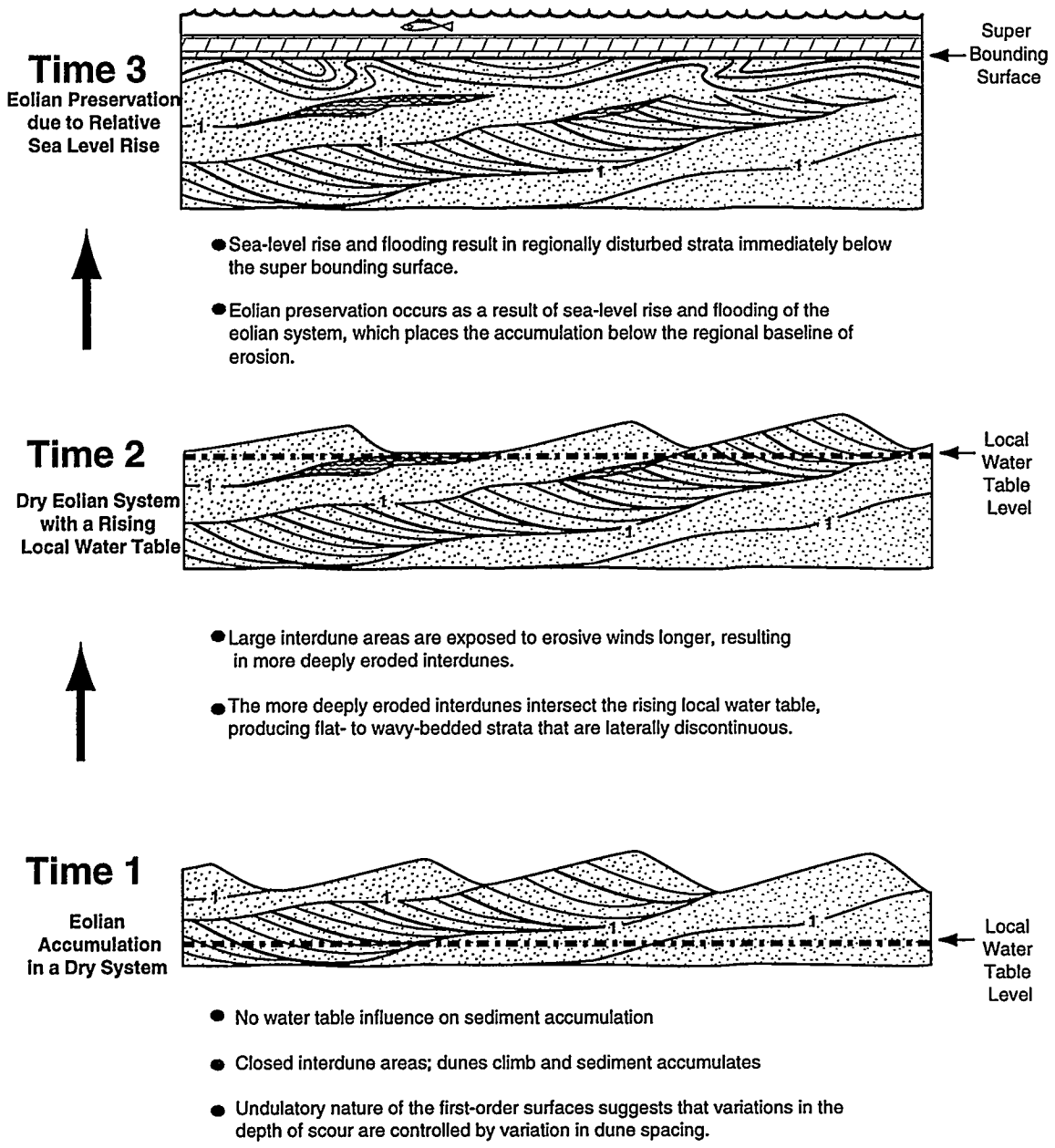

Figure 9. Model illustrating accumulation and preservation style of the Tensleep Sandstone.

Figure 10 illustrates how the Tensleep eolian-marine cycles would be placed into a sea-level controlled, sequence stratigraphic framework. The erosional surface that caps the eolian-marine sequences corresponds to a sequence boundary, which is a time-transgressive surface between the basin margin and the basin center accumulations.

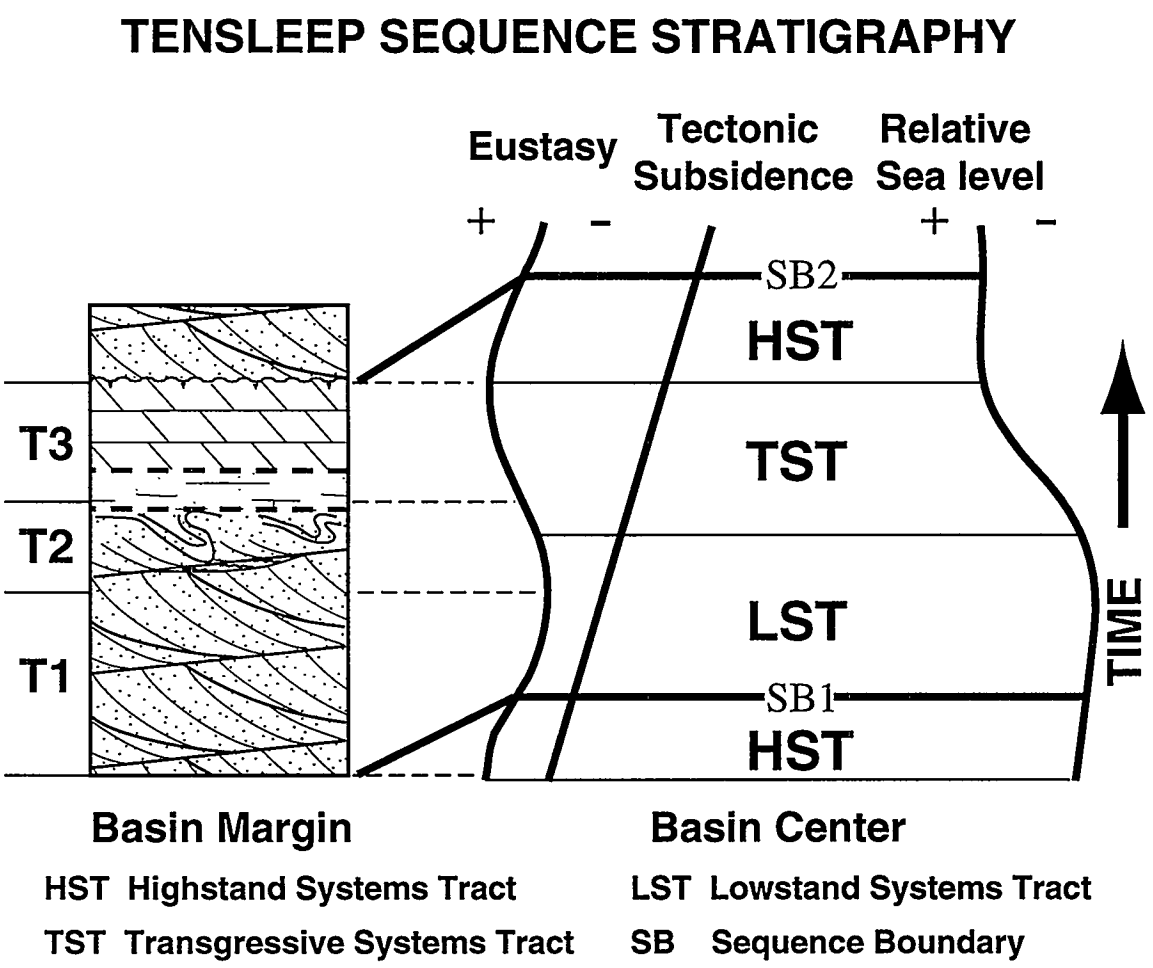

Figure 10. Idealized Tensleep eolian-marine cycle and its relationship to sea-level change.

Figure 10 places the Tensleep into a more regional context from which inferences about the timing of events in the basin can be related to their resultant effects on the basin margin shelf. Discussion below will relate the systems tracts to resulting facies changes and their petrophysical log responses.

CONTROLS ON RESERVOIR HETEROGENEITY

With these depositional processes in mind, reservoir heterogeneity within the Tensleep Sandstone can be divided into small-scale and large-scale heterogeneities. The small-scale heterogeneities, such as variations in stratification type, are directly related to the depositional processes that took place during accumulation of the eolian units. The sea-

level-driven sandstone-dolomite cycles represent the large-scale heterogeneities formed by preservation processes.

Accumulation Processes

As previously stated the Tensleep is composed of a series of eolian sandstone - marine dolomite cycles (Figure 7). The eolian sandstone units are composed of one to several sets of compound cross-strata. Individual sets of cross-strata represent the accumulation created by the migration of a single large bedform through the area. The erosional surface that separates one set of cross-strata from another is referred to as a first-order surface, and it is produced by the erosional processes taking place out ahead of a migrating bedform in the interdune area (Brookfield, 1977; Kocurek, 1981; Rubin and Hunter, 1982; Figure 11). The Tensleep first-order surfaces are commonly undulatory, and have been observed to show up to 20 feet of relief over a lateral distance of approximately 300 feet (Figure 12a).

First-order surfaces show the depth of scour in a particular interdune area through time. The depth of scour in a dry eolian system is controlled by how long a particular area is exposed to erosion, and this in turn is controlled by the width of the interdune, or dune spacing (Crabaugh, 1994). The larger the interdune area the greater the depth of scour. However, dune spacing can change through time, so that the depth of scour could also change, resulting in an undulatory surface, as illustrated in Figure 12a.

The undulatory nature of the first-order surfaces resulted in the formation of laterally discontinuous, lens-shaped interdune accumulations. The Tensleep eolian system was primarily a dry system in which accumulation processes were unaffected by the local water. However, as the relative sea level rose, it caused the local water table to gradually rise as well (Time 2, Figure 9). When the rising water table encountered the depositional surface in a deeply scoured interdune area, the interdune surface became damp and sand grains tended to become trapped in the capillary fringe of the water table and resist the

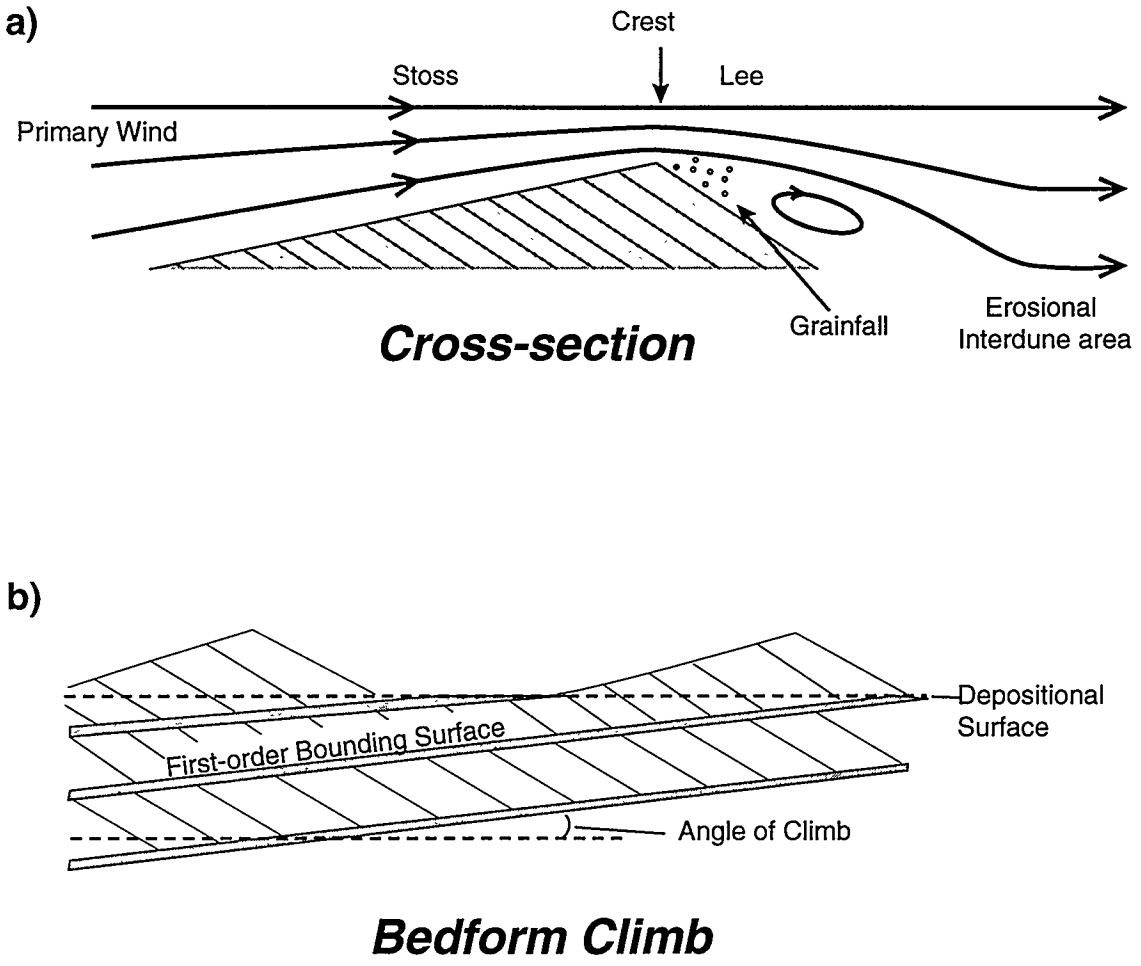

Figure 11. a) Bedform cross-section indicating general air flow patterns. Flow separation at the crest results in flow deceleration on the lee side and deposition of sand grains as grainfall deposits. As the upper lee face oversteepens the sediments overcome the coefficient of friction and flow down the lee face forming grainflows. The interdune area is characterized by flow acceleration and sediment erosion resulting in the formation of a first-order bounding surface. b) Illustration of bedforms climbing through time and space along first-order bounding surfaces.

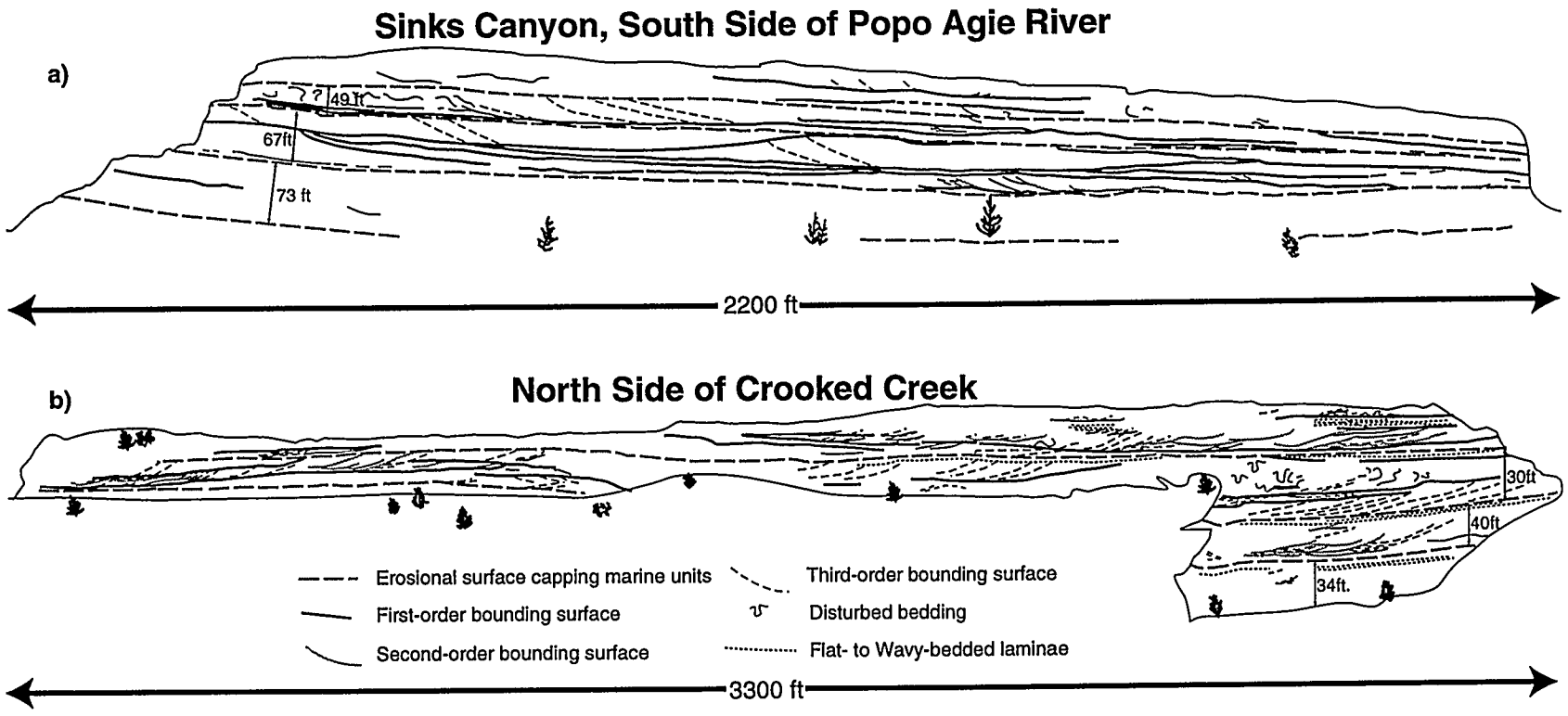

Figure 12. Scaled line drawing of outcrop photomosaics, illustrating complexity of stratification within the Tensleep Sandstone. a) Scaled drawing of outcrop photomosaic from the south side of the Popo Agie River in the Sinks Canyon State Park. Note the undulatory nature of the first-order surfaces. b) Scaled drawing of the outcrop of the north side of Crooked Creek inllustration the abundance of second-order surfaces in some portions of the Tensleep Sandstone.

erosive effects of the wind. The dampness of the interdune surface also led to the formation of evaporitic cements such as dolomite and anhydrite (Crabaugh, 1994). Biological activity in the form of bacterial and fungal growth would also have increased. All these factors led to the formation of interdune strata characterized as evaporite-cemented, mud-cracked, and wavy-bedded. Tensleep interdune accumulations tend to stand out in outcrop relief because they are more heavily cemented than the surrounding cross-stratified sets.

A set of cross-strata is defined as compound if it contains internal erosional surfaces. These internal erosional bounding surfaces indicate that erosion was taking place on the lee face of the bedform. According to Rubin and Hunter (1983) erosion on the lee face is caused by two processes: "(1) flow changes, such as shifting winds or reversing currents, that change bedform morphology and produce relatively synchronous bounding surfaces that are called reactivation surfaces, and (2) local erosion that may occur continuously in the troughs or on the stoss slopes of small bedforms that migrate across the lee slope of a larger bedform." The reactivation surfaces are referred to as third-order surfaces and the erosional surfaces caused by small superimposed bedforms migrating along the lee face of a larger bedform are called second-order surfaces (Brookfield, 1977; Kocurek, 1981). These surfaces have been identified in the Tensleep using the criteria set forth in the literature (Rubin and Hunter, 1983; Brookfield, 1977; Kocurek, 1981; Rubin, 1987; Crabaugh and Kocurek, 1993). Figure 13 is a schematic drawing of the compound cross-strata observed in Tensleep Sandstone outcrops.

The most common type of bounding surface in the Tensleep is the third-order or reactivation surface. These surfaces bound units that are characterized by a basal unit of low-angle wind-ripple laminae that roughly parallel the bounding surface they overlie. These wind-ripple laminae are overlain by higher-angle wind-ripple or grainflow laminae, which are in turn truncated by the next third-order surface (Figure 14). These third-order bounded units are related to annual fluctuations in air flow that occur in this monsoonal

Internal Bounding Surface Geometries: Barriers to Fluid Flow

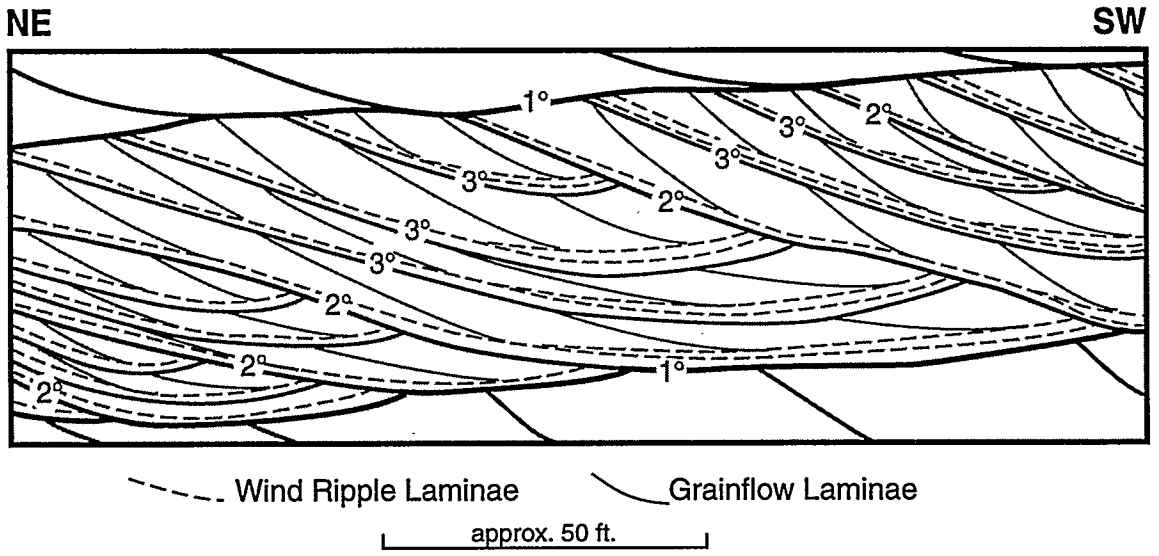

Figure 13. Schematic drawing of internal stratification within the Tensleep Sandstone. Illustration shows the cross-cutting relationships of the first-, second-, and third-order bounding surfaces.

setting. Such fluctuations in flow would have resulted in changes in the bedform morphology and that would be reflected in the resulting stratification.

While second-order surfaces are less common than third-order surfaces, their occurrence has had a significant impact on the reservoir quality of the rock. Second-order surfaces have been documented in outcrop exposures in both the Bighorn and Wind River basins as well as in core. As illustrated in Figures 12 and 13, second-order surfaces are capped by wind-ripple laminae and truncate the toes of annual packages bounded by third-order surfaces. As stated previously, second-order surfaces are the erosional surfaces created by the passage of superimposed bedforms along the lee face of the main bedform.

The complexity of the cross-stratified sets differs from one locality to another and laterally within the same set of cross-strata. Figure 15 illustrates the lateral change that can

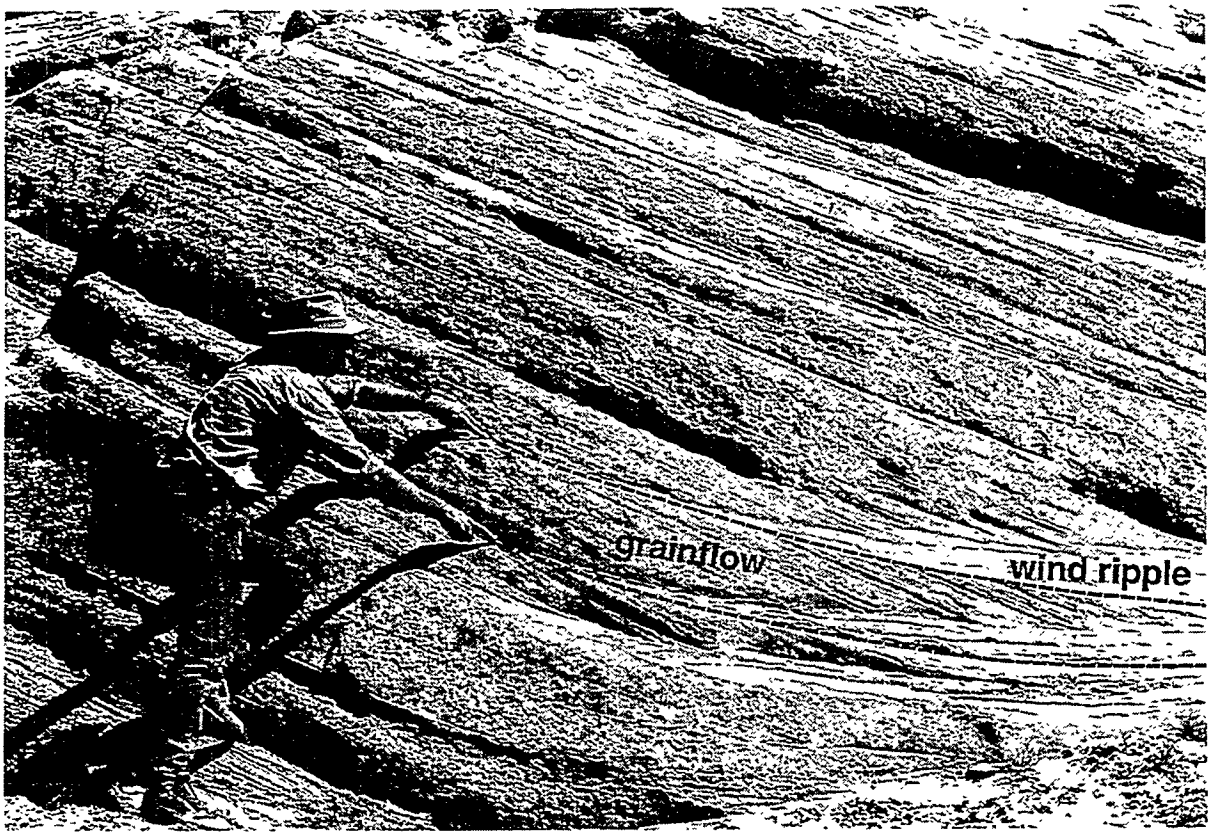

Figure 14. Outcrop photograph of flow-units bounded by third-order bounding surfaces. Dashed lines follow the erosional traces of the third-order surfaces. The surfaces are overlain by tightly packed low angle wind-ripple laminae which are overlain by higher-angle grainflow and wind-ripple laminae. Note the color difference between the grainflow laminae and the wind-ripple laminae. Man is 6 feet 6 inches tall and the photograph was taken at the Medicine Lodge measured section (Fig. 5).

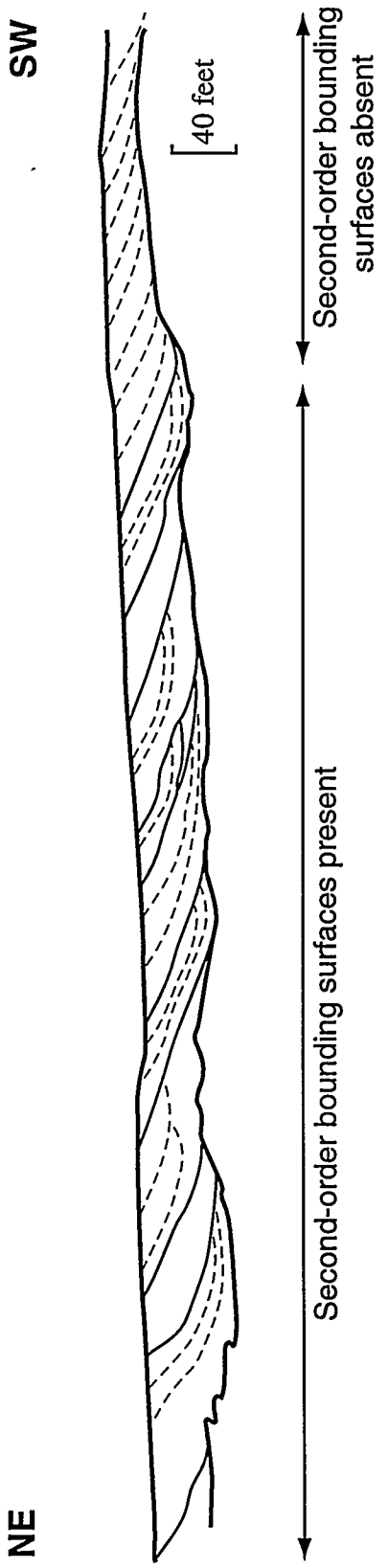

Figure 15. Scaled drawing of a portion of the Alkali Flats outcrop (Fig. 1), illustrating the lateral variation in the style of stratification. The section dominated by second order surfaces corresponds to that portion of the bedform in Figure 12 that is oblique to the dominant wind and has superimposed bedforms. The section lacking second-order surfaces and dominated by third-order surfaces, corresponds to that portion of the bedform in Figure 12 that is perpendicular to the dominant wind.

occur within a single set of cross-strata. In the northeastern portions of the set, second-order surfaces clearly occur, while 300 feet to the south, the same set of cross-strata does not exhibit second order surfaces. Only third-order surfaces are observed in the remainder of the set exposed in the outcrop. This lateral change reflects a lateral change in the overall geometry of the bedform that produced the cross-strata. Using the foreset and bounding surface orientations and following the method of Rubin and Hunter (1983) for bedform reconstruction, a bedform that reflects these variations in Tensleep Sandstone stratification was constructed (Figure 16).

A modern analog for the type of bedform that dominated the Tensleep erg is shown in Figure 17, which shows a Landsat image of a portion of the Cherchen Desert, northern Takla Makan Desert in northwestern China. The image is dominated by compound crescentic bedforms separated by discontinuous interdune areas. These large bedforms are 260 to 320 feet high and an average of 1.4 miles from base of stoss to base of lee. The distance along their lee face from horn to horn averages 2.0 miles (Breed et al., 1979). The interdune areas, like those postulated for the Tensleep, are laterally discontinuous. Parallel to the crestline of the bedforms, the interdune areas average 0.75 miles and across the interdune areas the average distance is 1.0 mile.

Conclusions: Effects of Accumulation Processes on Reservoir Heterogeneity

The Tensleep eolian units are composed primarily of wind-ripple laminae with lesser amounts of grainflow laminae. Wind-ripple laminae migrating across a lee face are formed by saltation processes that result in very tightly packed sand grains within each coarsening-upward wind-ripple laminae. By contrast, grainflow laminae result from avalanching processes on a lee face of the bedform, and are less tightly packed laminae. For this reason, wind-ripple laminae tend to be less porous than grainflow laminae (Goggin et al., 1988). This becomes important when considering how fluids flow through Tensleep reservoirs.

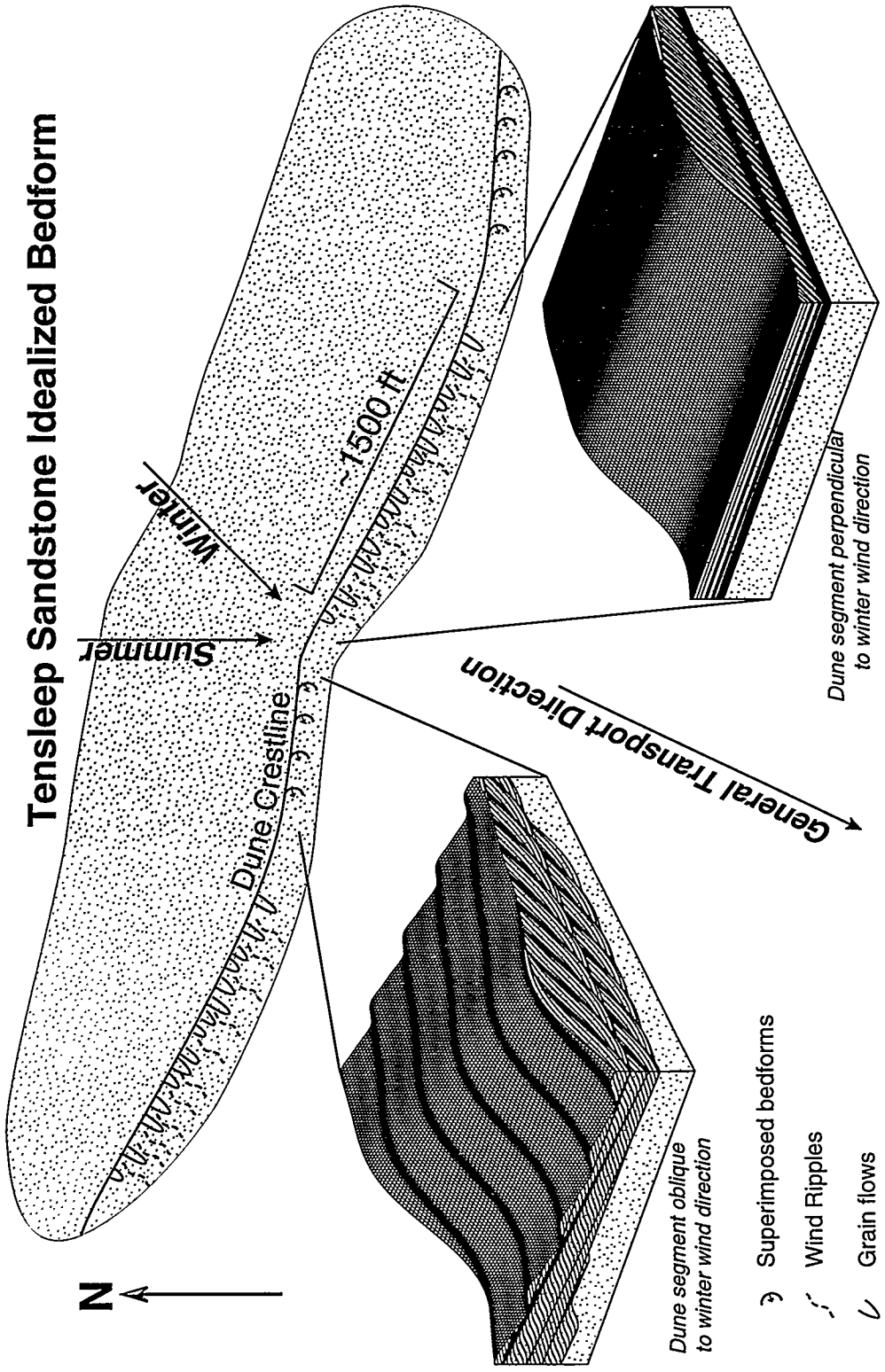

Figure 16. Idealized compound crescentic bedform for the Tensleep Sandstone. Bedform reconstruction made using bounding surface and stratification orientations, and the method of Rubin and Hunter (1983) to determinine orientations of superimposed bedforms. Main bedform is migrating to the south-southwest, and the superimposed bedforms are migrating to the west along the arms of the main bedform oriented more oblique to the dominant winter wind.

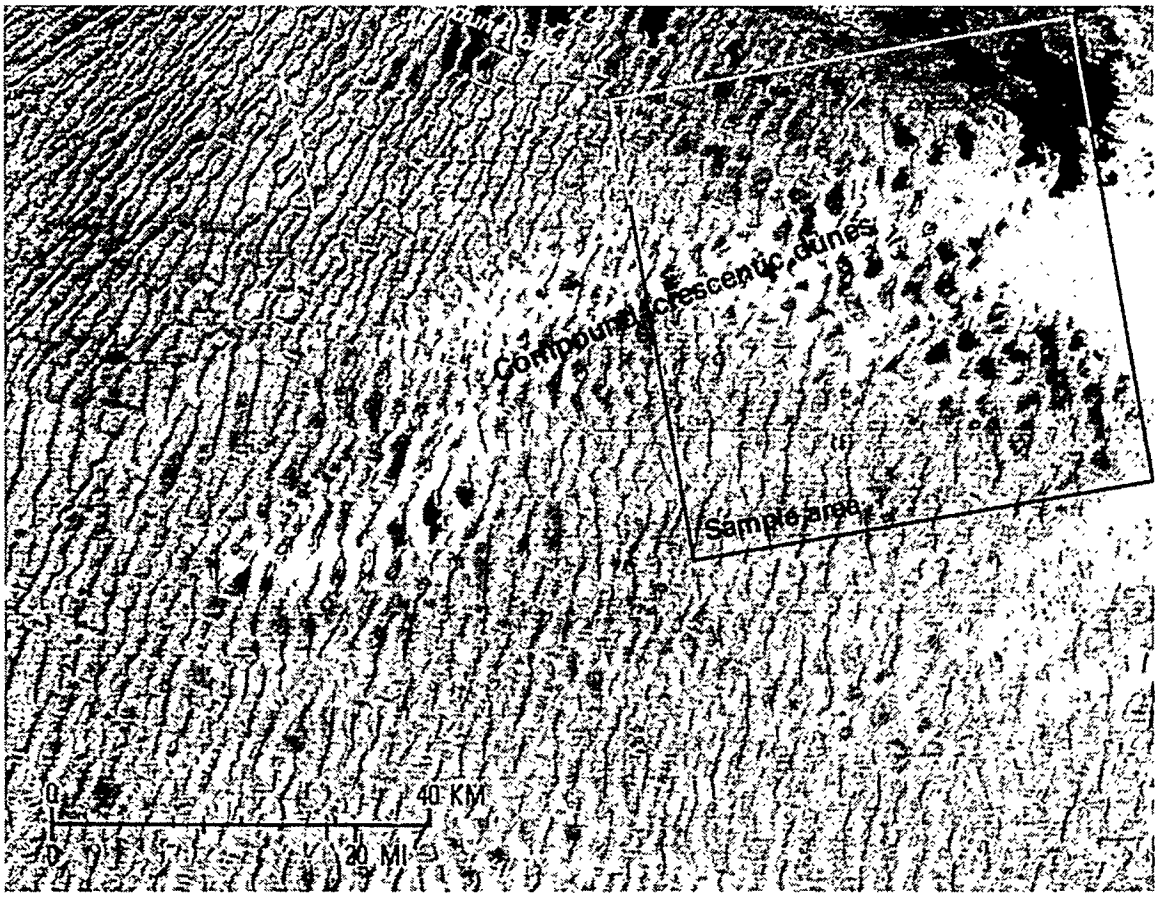

Figure 17. Landsat image of a portion of the Cherchen Desert northern Takla Makan Desert in northwestern China. The bedforms in this area are suggested as modern analogs for the Tensleep bedforms. Dune dimensions given in text were taken from the sample area. From, Breed et al., 1979.

The first-, second-, and third-order surfaces are all capped by tightly packed stratification and overlie more loosely packed stratification (Figure 13). Thin, tightly packed wind-ripple laminae overlie the bounding surfaces and below the bounding surfaces are grainflow laminae and thicker, less tightly packed wind-ripple laminae. The contrast in packing across a bounding surface tends to inhibit fluid flow across it; rather, fluids would tend to move parallel to the bounding surface. Figure 13 illustrates the general geometry of the internal erosional bounding surfaces and the flow-units they define. Figure 18a illustrates the general dimensions of the flow units perpendicular to the crestline of the Tensleep bedforms. The third dimension parallel to the crestline of the bedforms is much more difficult to measure because of the paucity of planview outcrop exposures of the Tensleep cross-strata. However, using the computer program of Rubin (1987) it is possible to reconstruct the bedforms and their internal geometries and estimate the third dimension of these flow units (Figure 18b). Improved definition of these units should have a positive impact on improving strategies for waterflood recovery in the Tensleep reservoirs.

There are several indications that the bounding surfaces serve as barriers to fluid flow in outcrop and in core. In outcrop, the strata above and below a bounding surface are of different color, suggesting that the two areas have experienced somewhat different diagenetic histories (Figure 19a). Increased carbonate and anhydrite cementation is also noted along bounding surfaces in Tensleep cores (Figure 19b). The cementation increase is presumably a result of greater fluid flow along the bounding surface rather than across it.

In order to determine relative permeability characteristics of these flow-units and their erosional bounding surfaces, a series of samples have been taken over the past two summers. Last year, sampling concentrated on stratification types (wind-ripple and grainflow laminae) observed in the Tensleep. This year, sampling concentrated on the bounding surfaces and their relative permeability characteristics. A further discussion of sample treatment and results follows in Task 2.0.

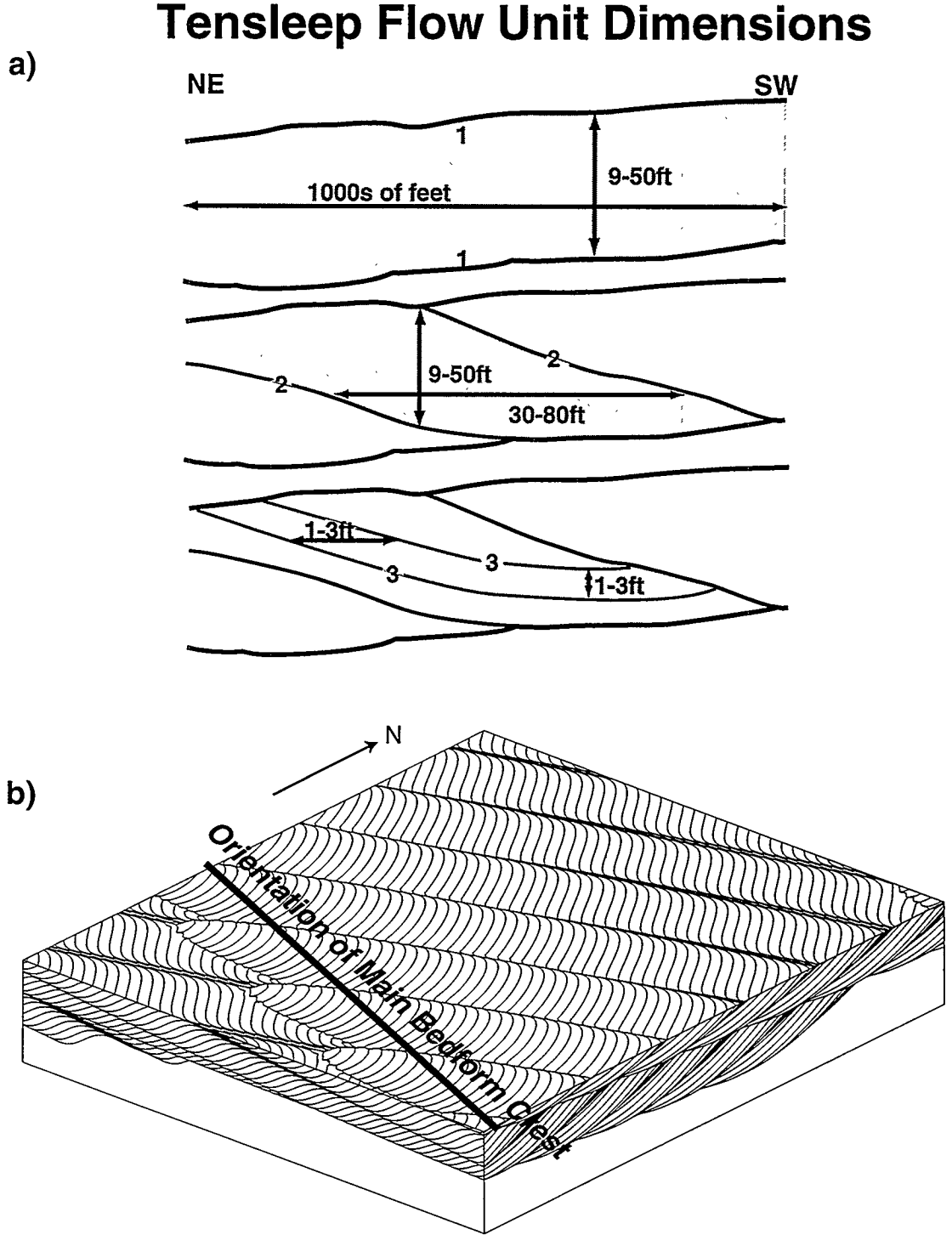

Figure 18. a) Dimensions of first-, second-, and third-order bounded flow units perpendicular to main bedform crestline. b) Bedform reconstruction shows plan view appearance of flow units. This view allows estimates of flow unit geometry generally parallel to main bedform crestline. Figure 16 shows the same bedform with surface features restored.

a)

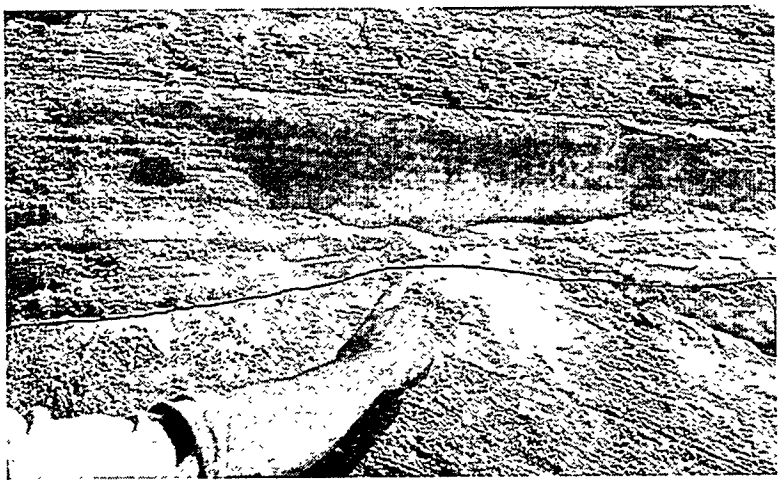

b)

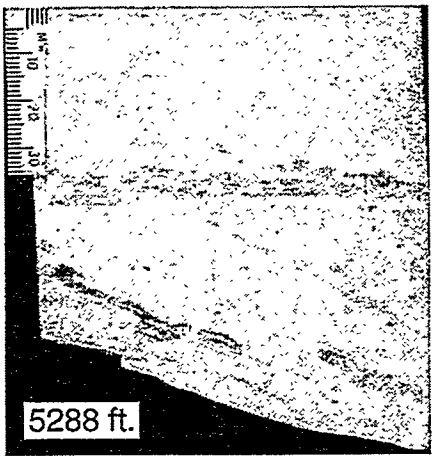

Figure 19. Diagenetic features associated with bounding surfaces. a). Outcrop photo from the Medicine Lodge section (Figures 5 and 14). Major color change across a first-order bounding surface. Note low-angle wind-ripple laminae above surface and higher-angle grainflow and wind-ripple laminae below. b) Incerased cementation along a first-order bounding surface in a core sample from the EBET #217 located in the Elk Basin field (Fig. 1). Scale bar in millimeters.

Preservation Processes

In order for sediments to be preserved and enter the rock record, they must be placed below some baseline of erosion. In the case of the Tensleep, this was accomplished through cyclic relative sea-level rises probably related to glacial activity in the southern hemisphere (Wanless and Shepard, 1936; Crowell and Frakes, 1972; Ramsbottom, 1979). As the sea transgressed, the low interdune areas were first inundated, but with time the entire dune field would have been flooded (Figure 9). The uppermost portions of the eolian units frequently show soft-sediment deformation that is related to flooding of the dune field. This deformation is in some way related to flooding of the area and fluid escape, but the exact mechanism of deformation is not well understood. With complete flooding, the uppermost eolian sediments were reworked into burrowed, dolomitic sandstones, and with further flooding an open marine environment developed, ultimately resulting in the formation of sandy, fossiliferous dolomites (Figure 9).

Conclusion: Effects of Preservation Processes on Reservoir Heterogeneity

It has been recognized for some time that the heavily cemented marine dolomitic units can act to compartmentalize the Tensleep by acting as vertical barriers to fluid flow between the eolian cross-stratified units. Well-log stratigraphic correlation work indicates that the marine dolomitic units can be correlated over large areas. Three of the dolomitic units are correlated from the western to the eastern side of the Bighorn Basin (Figure 20). Individual eolian units generally thicken to the west and show significant local variation in thickness across the basin. These local variations in thickness are caused by subtle differences in local subsidence rate. The dolomitic units also vary in thickness in response

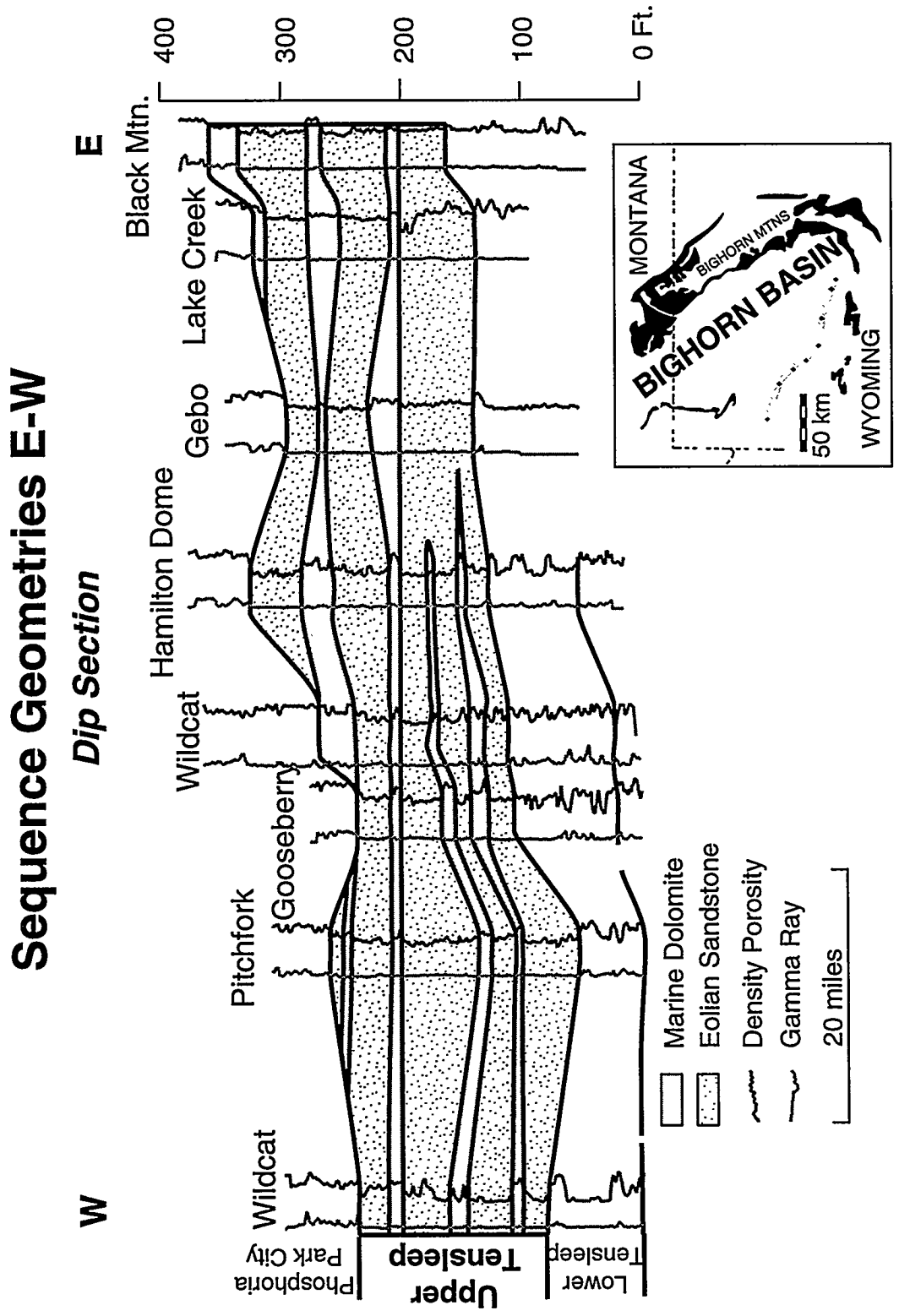

Figure 20. West to east cross-section across the southern Bighorn Basin. Individual marine dolomites can be traced across the entire basin. Line of section is indicated on inset map.

to variations in subsidence rate and differential erosion along the upper surface of the dolomitic units during lowstand exposure.

Soft-sediment deformation as a result of relative sea-level rise also appears to have an impact on permeability distribution in the Tensleep Sandstones. Study of cores with core analysis (porosity and permeability measurements) reveals there is an increase in permeability associated with uppermost portions of individual eolian units and in particular the disturbed zones (Figure 21). Disturbed zones generally occur toward the top of individual eolian units and are associated with the transgressive systems tracts (TST) (Figure 10). It is postulated that this increase in permeability is a result of soft-sediment deformation causing a change in the pore geometry. The homogenization of the strata caused by the soft-sediment deformation would also tend to lessen the effects of the compartmentalization formed by the erosional bounding surfaces. However, more core and core analysis data must be acquired in order to statistically determine if the transgressive systems tracts can be recognized in well logs.

FUTURE PLANS

Work in the fall of 1995 will concentrate on completing the subsurface study of the North Dome of the Oregon Basin field. This will involve completing core and FMS descriptions. Also in the fall of 1995 the subsurface correlations of the Wind River Basin will be completed. Once the subsurface studies are complete then all the data will be integrated together to form a cohesive picture of the process-oriented controls on reservoir heterogeneity. Specifically the geometry and distribution of different types of reservoir flow-units will be further documented.

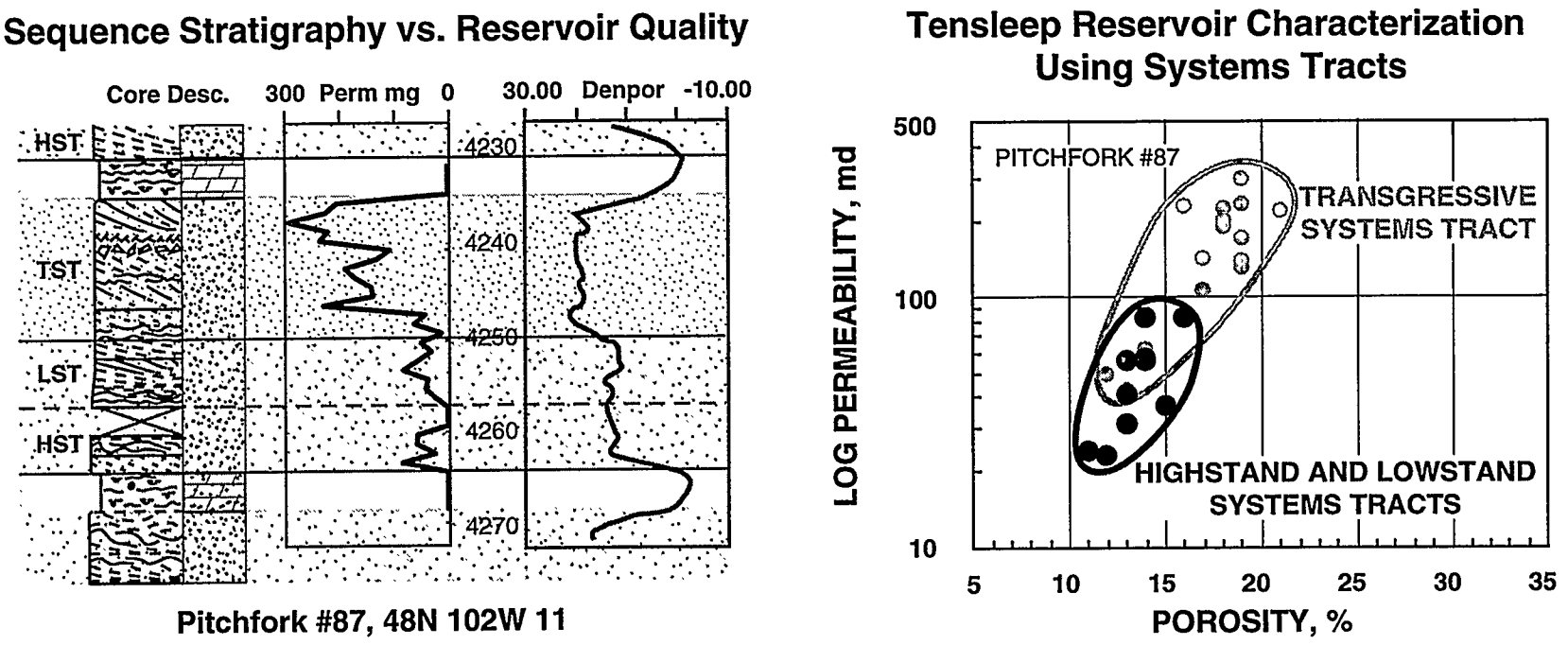

Figure 21. a) Comparison of Pitchfork #87 core description with its permeability and density porosity log showing the increase in permeabiliy and porosity in the transgressive systems tract (TST, Figure 10). b) Log permeability versus percent porosity for the same sandstone-dolomite cycle in the Pitchfork 87 well. Note that permeability and porosity are higher for the transgressive systems tract than for the highstand and lowstand systems tracts.

TASK 2.0 - RELATIVE PERMEABILITY MEASUREMENTS.

William Iverson - Task Leader

OBJECTIVES

The focus of this task is to obtain quantitative laboratory data on the magnitude and variability of relative permeability anisotropy and spatial variation of the dominant reservoir and boundary surface lithologies of the Tensleep Sandstone. Existing data will be collected, compiled, and placed within the regional frameworks constructed in Task 1.0. Relative permeability will be measured at UW using the unsteady-state technique. An additional objective of this study is to provide algorithms for calculating relative permeability from quantitative pore imagery data.

RELATIVE PERMEABILITY MEASUREMENTS

Introduction

An additional 24 cut and prepared core samples reached the laboratory for relative permeability measurements during the past (second) year of work. (Forty-eight samples were collected during the first year.) Table 1 summarizes the status of all samples examined to date in the laboratory. Sample collection continues at present, and procedures are continuously assessed to produce the most useable and unbiased dataset. Quality control standards have remained high, so many samples have not actually produced useable data points for the final relative permeability anisotropy plots to be described below. In fact, of the approximately 100 samples collected, only 72 sized cores reached the laboratory, and a final 17 data points are used on the relative permeability plots. There are two core samples required (one vertical and one horizontal, v and h in Table 1) for each set of data points, but a substantial number of cores were omitted due to channeling, cracks, size, or being simply too "tight" for the apparatus. We have attempted to present data points of high reliability.

The procedure used to determine relative permeability, commonly called the unsteady state technique, is one described in detail by Ajdari (1995). Complete permeability calculations for one sample were presented in our first annual report (Dunn,

Table 1. Relative permeability sample status.

Core	air perm	brine perm	oil perm	status
Samples from surface blocks:				
1v	423 (md)	190	182	complete Kr measurements
1h	469	405	182	complete
2v	470	368	192	complete
2h	427	127	240	complete
3v	0.65			too tight for apparatus
4h	155	122	103	no pair orthogonal
5h	461	361	196	no pair
6h	618	504	264	no pair
Samples cut in field from outcrop:				
Ah	161	114	88	complete
Av	104	89	56	complete
Bv	14	7	3	channel of water during flood
Bh	78	51	38	channel
Cv	158	136	70	complete
Ch	138	108	74	complete
Dv	101	68	37	complete
Dh2	162	121	55	complete
Dh3	244	205	78	complete
Ev	547	503	203	complete
Eh1	344	256	131	complete
Eh2	443	394	197	complete
F&G				shape problems
Hv	690			no pair
Hh1	795			shape problems
Hh2				shape problems
Iv	664	702	383	complete
Ih1	744	898	487	complete
Ih2	863		293	shape problems

Table 1. (continued)

Core	air perm	brine perm	oil perm	status
Samples from subsurface oil well cores (number corresponds to depth of core):				
3248h	172	152	65	complete
3248v	158	152	64	complete
4014h	73	70	27	complete
4014v	60	41	19	complete
3217v	2			too tight
3217h	12			no pair
3248v	158	152	64	complete
3248h	172	166	65	complete
3289v	36	22	11	complete
3289h	142	92	66	complete
3962v	31	24	9	complete
3962h	57	52	20	complete
3980v	46	37	12	complete
3980h	65	77	22	complete
3986v	12	6	3	complete
3986h	103	93	34	complete
4014v	60	41	19	complete
4014h	73	70	27	complete
6726v	37	25	10	complete
6726h	48	33	24	complete
6727v	40	32	9	complete
6727h	84	89	23	complete
6815v	5			in progress
6815h	50			in progress
6871v	6			in progress
6871h	118			in progress
6872v	50			in progress
6872h	127			in progress

1995), and the same calculations have been performed on all samples reported here. We now have a sufficient amount of data to demonstrate our observations of relative permeability anisotropy. It remains to be determined, however, which measure of relative permeability best describes the observed anisotropy.

Measured Data

Relative permeability data is shown for Sample A in Figure 22. The letter A represents the geographic sampling locality; Av is a core cut with the long axis perpendicular to bedding, and Ah is a core cut parallel to bedding (such that water flooding is directed along the observed bedding planes). Note that most of these data cluster in one spot and the contrast between vertical and horizontal orientations is small (Figure 22). Alternatively, the ratio of water permeability to oil permeability may be plotted on semi-log paper versus water saturation, as shown in Figure 23. A similar plot is used by Willhite (1986) to display relative permeability data. This plot shows clearly the difference between vertical and horizontal cores, and represents the point in our investigation that we reached at the time of the first annual report (Dunn, 1995). Since that time, numerous cores have been carried through this complete procedure. Each set of samples shows a similar trend, best described qualitatively as the curve for the vertical core falling above and to the left of the curve for the horizontal core. Such a descriptive approach is useful for recognizing a consistent trend, but is more useful when refined quantitatively as a single point for each pair of cores. Then all cores can be compared on one summary plot.

One measure of relative permeability anisotropy is the deviation from equality of the relative permeability ratios (krw/kro) in paired vertical and horizontal cores at the water saturation corresponding to water breakthrough during the experiment. For sample A, water breakthrough occurs when the outlet end of the core is at 62% water saturation; the horizontal relative permeability ratio is 0.9, and the vertical relative permeability is 10.0 (see Figure 24). These coordinates can be used to summarize the "above and to the left"

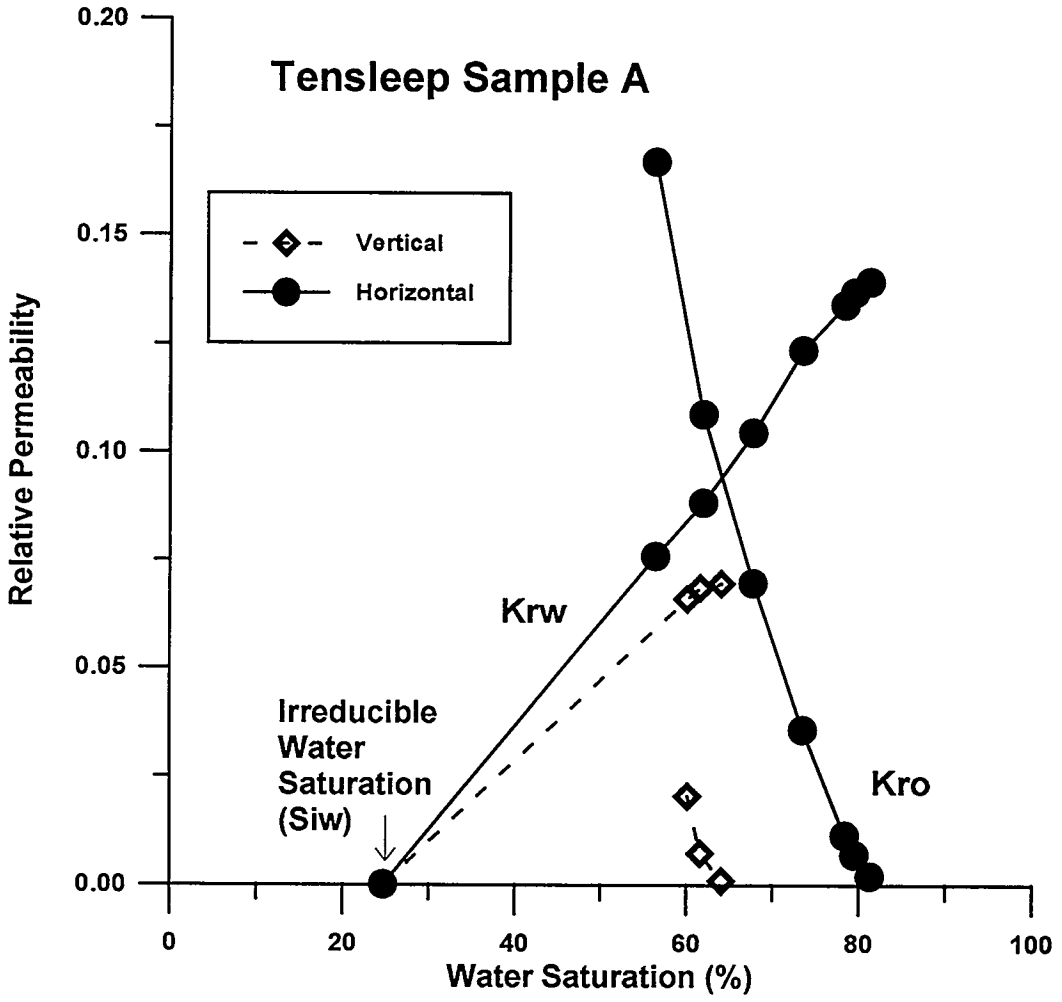

Figure 22. Relative permeability curves computed for Sample A. Procedure described by Dunn et al (1995). Unsteady-state laboratory technique only allows a limited range of water saturations to be investigated.

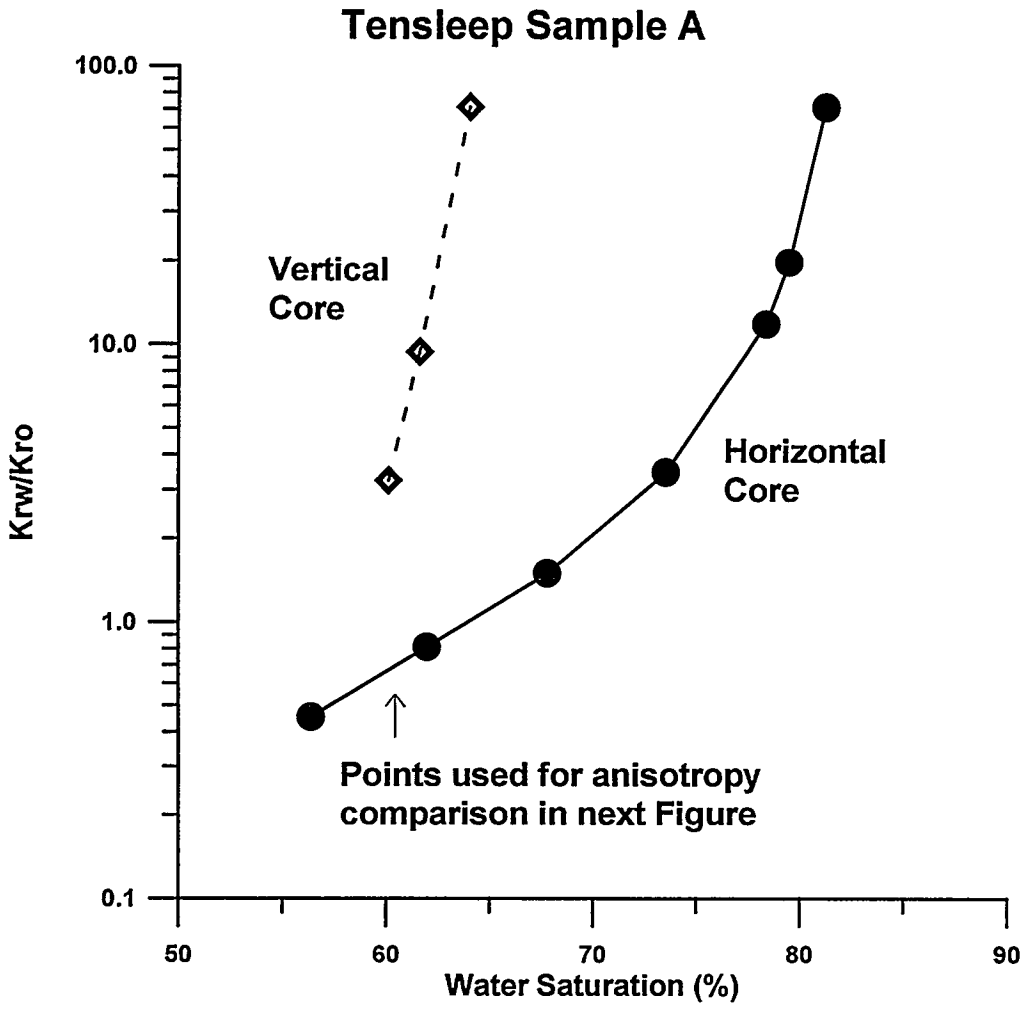

Figure 23. Ratio of water to oil permeabilities plotted against water saturation to show distinct anisotropy trend observed in many of the Tensleep samples.

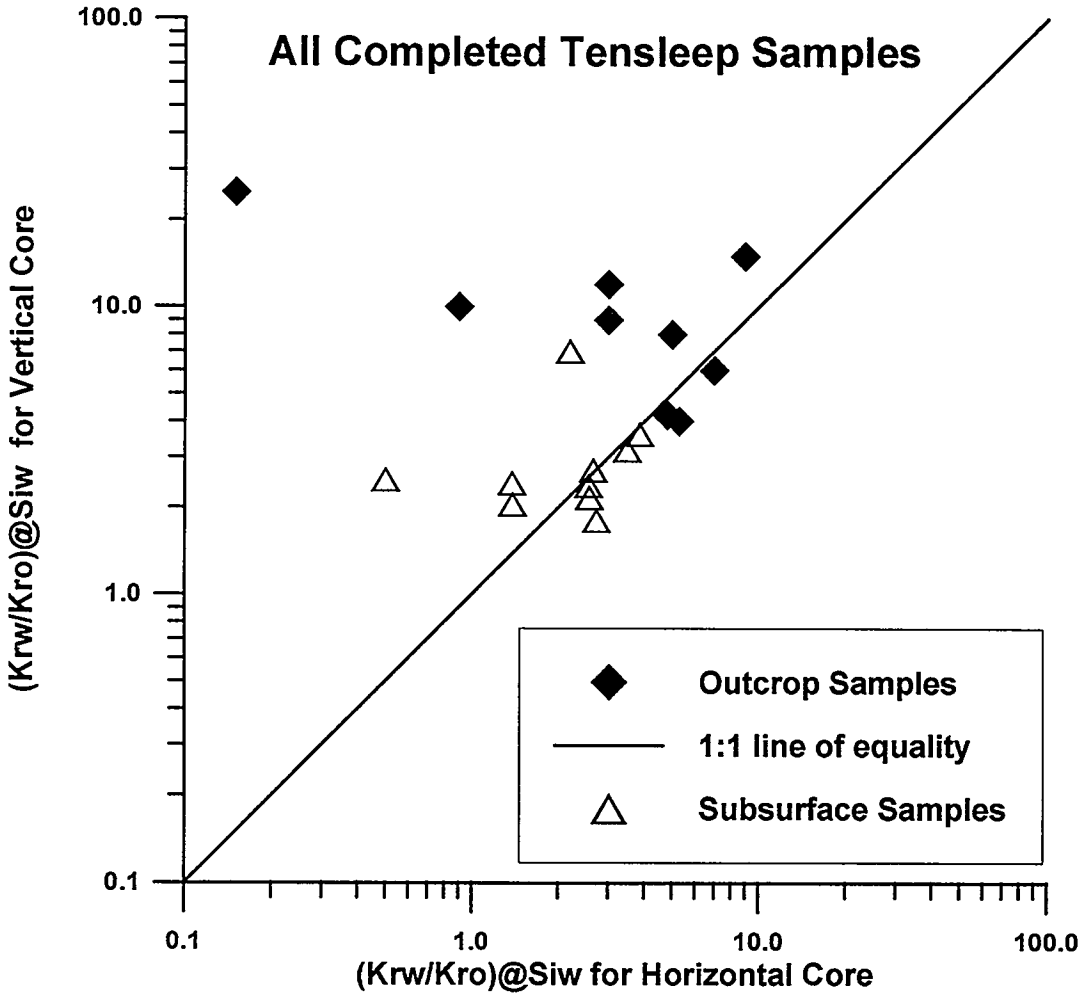

Figure 24. Ratio of permeabilities (as in Figure 23) is taken at water breakthrough saturation (left end of curve in Figure 23) for each Tensleep sample, and the vertical ratio is plotted against the horizontal ratio as shown above. The anisotropy trend is for a generally larger ratio from the vertical core.

deviation from equality indicating anisotropy, as observed in Figure 24. Similar calculations have been completed on sufficient cores to yield a total of the 17 summary data points shown in Figure 24. The solid data points in the figure represent the initial dataset of cores cut from outcrop samples of Tensleep sandstone, and the open points from plugs cut from subsurface cores. The subsurface samples all have generally lower absolute permeability, but both show the same trend of relative permeability anisotropy.

Prior to relative permeability measurements, absolute gas permeability was measured for each core sample. Figure 25 shows the expected trend of absolute permeability anisotropy. In general, the horizontal core samples show slightly greater permeability, as the gas flows easier when flowing parallel to bedding. This was expected for absolute gas permeability (single-phase). Prior to this research work, the trend for relative permeability (two-phase flow) was unknown because both phases might experience the same resistance. We observe consistent relative permeability anisotropy.

Interpretation of Results

In general, Figure 24 demonstrates that the vertical permeability ratio (krw/kro) is greater than the horizontal permeability ratio, on average. There are samples that do not follow this trend, and some lie on the line of equality, but the definite trend of a skew towards anisotropy is as described above. Physically, this trend can be understood by considering the ease or difficulty with which oil is pushed out of a core by waterflooding. A larger krw/kro ratio indicates a generally smaller oil relative permeability, kro. Oil is more difficult to push when this ratio is large. In other words, after water breakthrough occurs, it becomes difficult to push any more oil out of the core. In the field, the largest share of oil to be recovered, when flooding vertically, comes out prior to water breakthrough. Flooding vertically, perpendicular to bedding, acts more like piston-type displacement, in which oil is displaced in front of the waterflood front and residual oil remains behind the front.

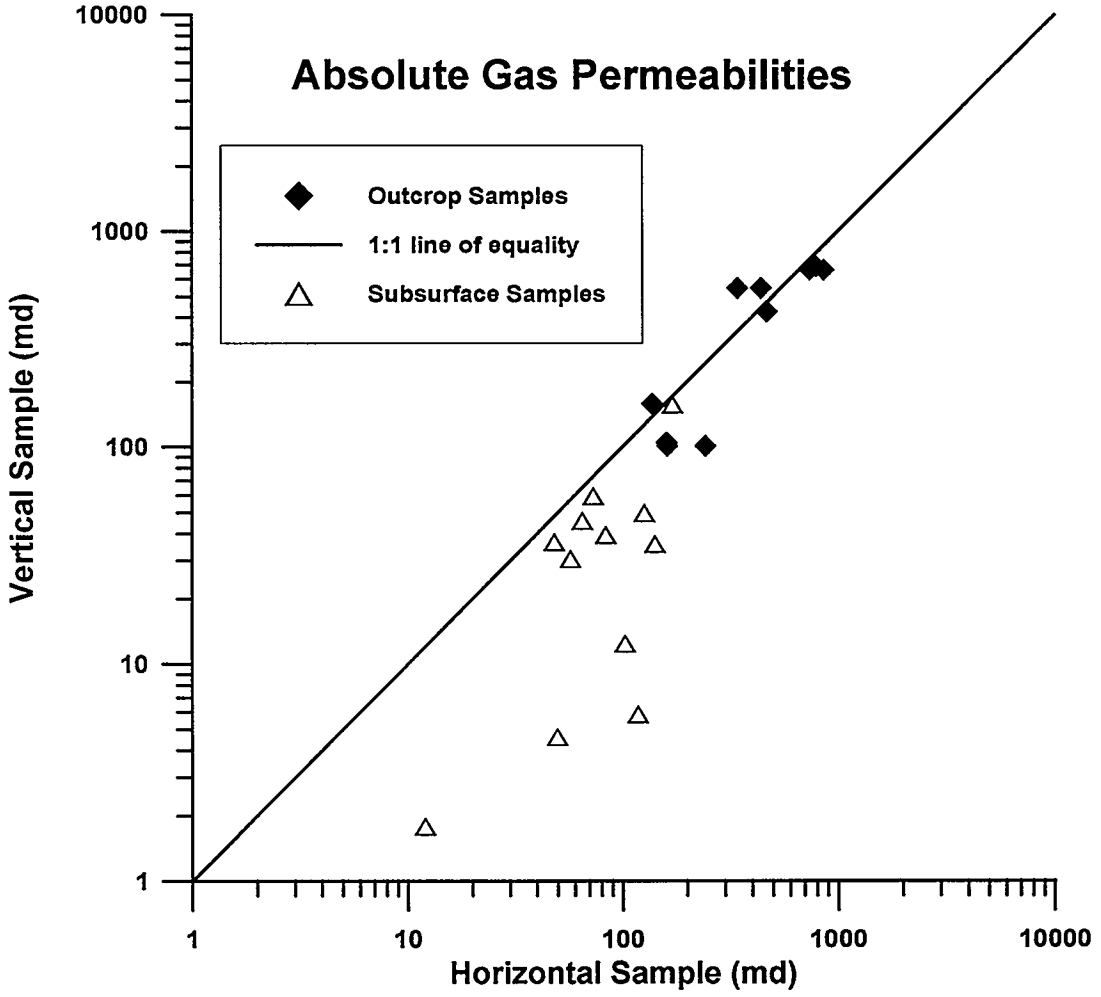

Figure 25. Gas permeabilities (absolute single-phase) for each Tensleep sample. Trend in absolute anisotropy is for slightly higher permeability in the horizontal direction when flow is parallel to bedding.

The piston-like displacement argument seems to be the best way to conceptually understand the character of relative permeability anisotropy observed in these experiments. Piston-like, in this context, refers to the old model of all oil flowing in front of the injected water and all water flowing behind the flood front. Although this piston-like idea is an extreme concept, and certainly not the actual process going on here, it is instructional to tie together the processes modeled from these data. A vertical flood is more piston-like in oil displacement, while the horizontal flood is more gradual. This might be expected if we consider the channeling effect that bedding planes can have when flooding horizontally and parallel to bedding. First of all, remember that the cores being tested are small and designed to minimize fingering and channeling effects. In fact, fairly uniform displacement is obtained throughout all these cores. But apparently the horizontal waterfloods do help bring the water through more easily, and leave a considerable amount of oil to be displaced after water breakthrough. Such a concept can be verified by reservoir simulation, as covered in the following section.

An important concept based on general relative permeability anisotropy is the prediction of when most of the oil will be produced from an oriented waterflood. For classic piston-like displacement, all of the oil to be produced is extracted prior to water breakthrough, and then all water is produced. Insofar as vertical flooding is similar to piston-like behavior, we should expect a larger fraction of oil to be produced prior to water breakthrough. Each sample must be normalized individually to the total oil produced after flooding completely to residual oil, as each sample has a slightly different pore volume of oil in place. Figure 26 shows such a comparison, which again verifies the relative permeability anisotropy concepts developed above.

To produce Figure 26, we took, for each sample, the volume of oil produced prior to breakthrough and divided that volume by the volume of oil produced to the end of the experiment at 100% water flow. For example, Sample A has been detailed through previous reports.

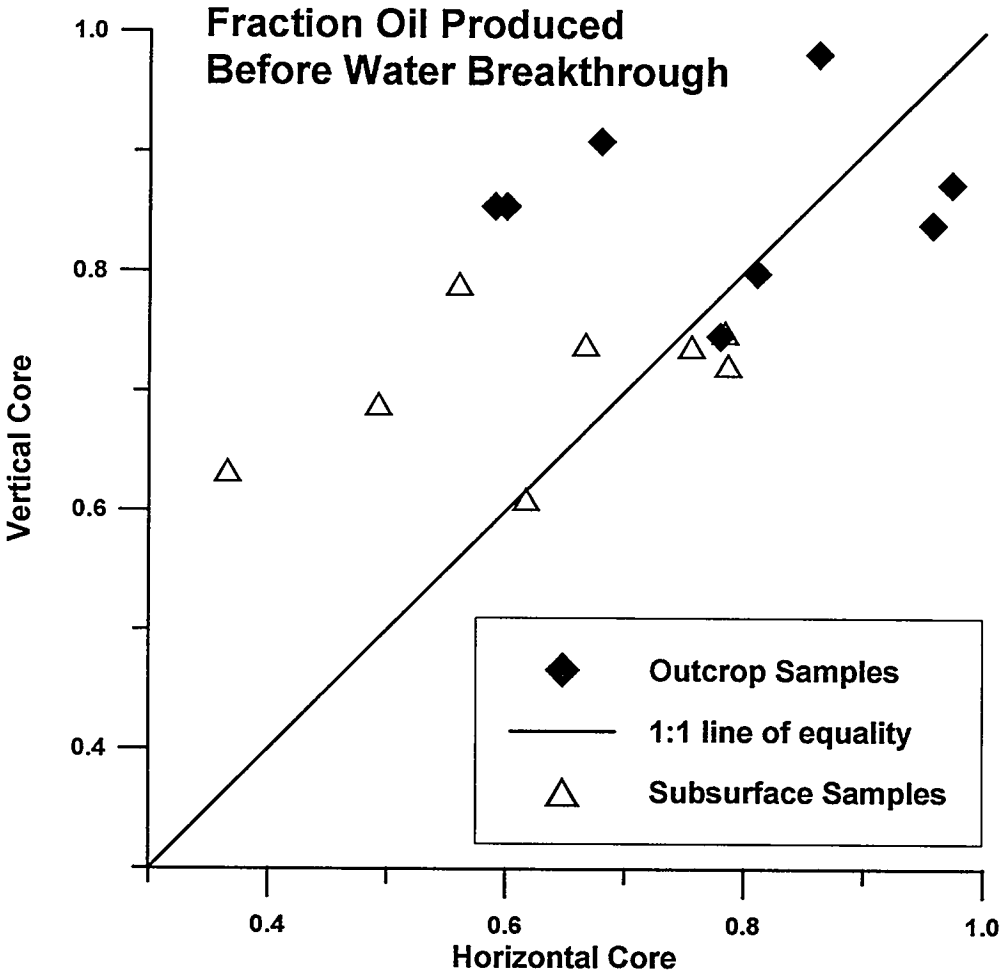

Figure 26 . Of the total oil produced by waterflooding each core, the vertical cores tend to yield a greater fraction of that oil prior to water breakthrough. A fraction of 1.0 in this plot would be total "piston-like" displacement where all the oil is produced in front of the flood front.

The raw laboratory data for Sample A is:

Core	Time (min)	Oil (cc)	Fw	% Oil
Vertical Core:				
Av	6.6	3.5	0.0	91
	(many intermediate points)			
Av	85	3.85	1.0	100
Horizontal Core:				
Ah	6	3.5	0.0	68
	(many intermediate points)			
An	75	5.15	1.0	100

Many data points are taken over the course of the two-hour relative permeability experiment on each sample, and only the two end-points are listed in the table above. For sample A, both initial points were about six minutes into the experiment, just prior to water breakthrough, when the fraction flow of water (fw) was zero. Both vertical and horizontal samples had recovered 3.5 cc of oil up to that time. The vertical core, however, recovered very little additional oil, so that 3.5 cc represents 91% of the total oil flooded out of the core when flooding was carried to flow of just water (fw = 1). For the horizontal core, the 3.5 cc of oil recovered prior to breakthrough is only 68% of the total oil recovered to flood-out. These data result in a single data point at (0.68, 0.91), plotted in Figure 26 for Sample A. The procedure was repeated for all completed samples to complete the plot.

Summary

As more data is collected, the trend of relative permeability anisotropy becomes more clearly defined. As with any geological sampling, many cores must be compared and contrasted before the trends are established. Individual data points might fall counter to the overall skew established by many samples, but an average deviation away from an isotropic case can be defined. After water breakthrough has occurred (and other parameters

held constant), the oil relative permeability is less in the vertical direction and greater in the horizontal direction. This causes a generally higher krw/kro ratio for vertical flooding than for horizontal flooding, and implies that a larger fraction of the total oil flooded from a sample will be recovered prior to water breakthrough, generally largest when flooding vertically.

Future Plans

Implications of this research on horizontal drilling will be considered as progress continues in reservoir simulation and field history matching. Particular attention will be paid to applications to mature waterflood projects, which are common in the United States. Additional samples will be added to the basic database to refine and verify the trends observed to date for relative permeability anisotropy.

RESERVOIR SIMULATION

Introduction

Reservoir simulation work has considered four computer programs already available at University of Wyoming. These programs are based on theories published by Stiles (1949), Dykstra-Parsons (1950), and Buckley-Leverett (1942), and a copyrighted program, TETRAD. Each is operational on IBM-compatible PCs, and each has been considered for applicability to this relative permeability anisotropy study. The Buckley-Leverett program was selected for reasons outlined in our previous report.

The Buckley-Leverett program is a simple one-dimensional program that follows accurately the complete relative permeability behavior as predicted by Buckley-Leverett theory. The major disadvantage of the program is the fact that it is one-dimensional. Its advantage is its adaptability to variable relative permeability characteristics of oil/water systems. Each relative permeability curve is input to the Buckley-Leverett program by characterizing the residual end-point saturations, and then by characterizing behavior

between end-points by a power-law relationship against dimensionless saturation. As all our results appear to follow power-law relationships quite well, the program seems well suited for this project.

Curve Fitting

As discussed under the relative permeability measurements task, vertical cores yield a generally higher krw/kro ratio than horizontal cores. One way to quantitatively represent this observation, while holding all other variables constant, is to model relative permeability with a slightly higher slope in a power law equation for the vertical core. Figure 27 shows the relative permeability points for Sample A, fit with the best-fit power-law functions. The procedure is that described by Willhite (1986). Note that a limited range of data is used to determine an equation for the entire range of water saturations. This is one disadvantage of the unsteady-state displacement technique, where all data points fall naturally in just the range of water saturations between water breakthrough and floodout of the core. Regardless of the range of data used, or the type of curve fit used, the general trend is to fit a slightly steeper slope to vertical cores.

Each set of cores yields a different power-law fit to the observed data. A single universal set of equations cannot be determined. The span of changing variables (residuals, end-points, slope, rate, porosity, viscosity, and many other physical constants) is too great for isolating the effects of just the newly observed phenomena in relative permeability anisotropy. So, it was decided to approach a reservoir simulator by holding all variables constant, and then slightly varying just the slope of the relative permeability power law function. Figure 28 shows the power-law equations input to a Buckley-Leverett simulator. Note that residual saturations and end-points are held constant so that both vertical and horizontal cores are modeled as having the same initial oil in place, the same irreducible water saturation, and the same residual oil saturation. A run through the

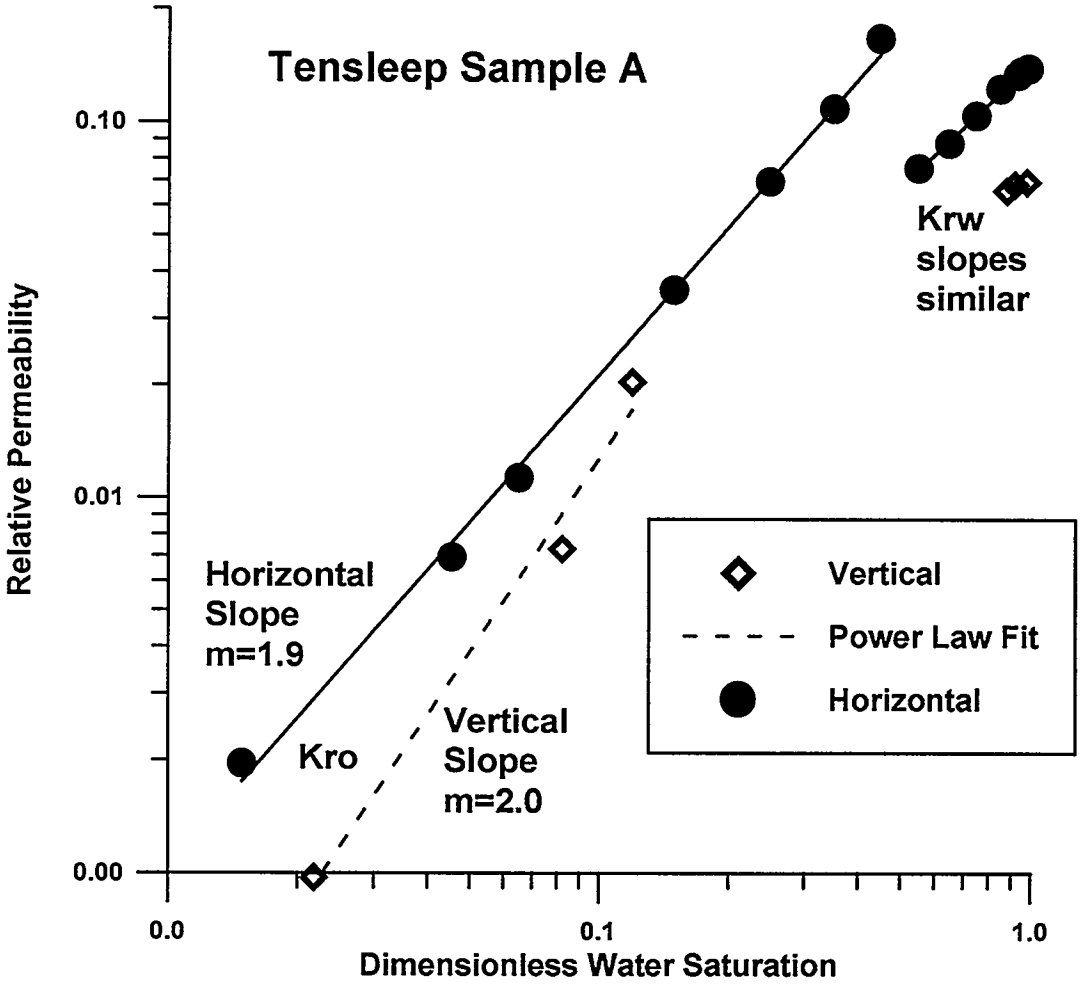

Figure 27. Same data points as shown in Figure 22, but now plotted against dimensionless water saturation as defined by Willhite (1986). Lines are best-fit power law functions to yield an analytic function of relative permeability for input to the Buckley-Leverett simulator.

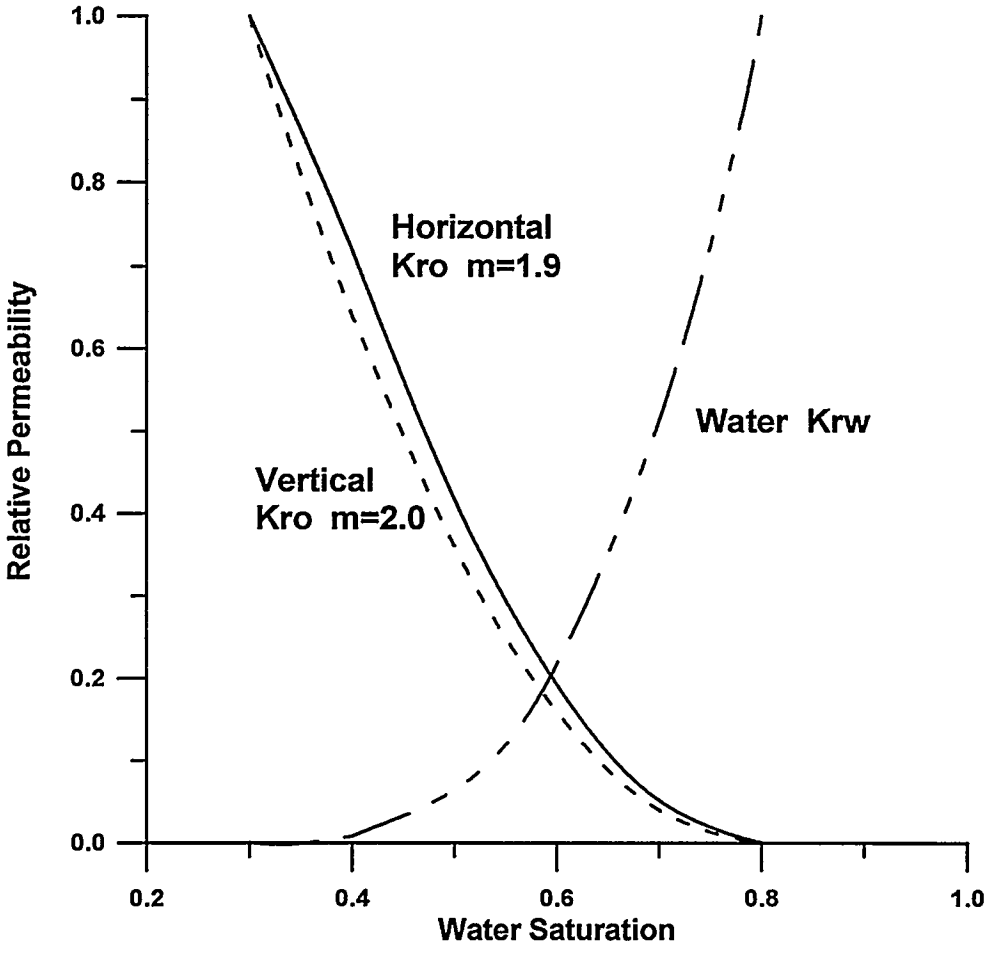

Figure 28. Assumed relative permeability curves (power laws) input to Buckley-Leverett simulator. Water Krw curve, and end-points of curves are all held constant. Only the exponent (slope in Figure 27) is allowed to vary between vertical and horizontal comparisons.

simulator will demonstrate the effects of only a small change in the slope of a power-law fit.

Buckley-Leverett Simulator

The program basically follows the technique outlined by Willhite (1986), where a power-law relative permeability equation is used to derive a fractional flow curve. A derivative is computed at each water saturation to determine the extrapolation to average water saturation as a function of the pore volume of water injected. By providing a constant pressure drop, absolute permeability, and reservoir geometry, the flow rates and thus the times to each point are finally calculated. For one case representing horizontal flow, the complete list of input constants is shown in Table 2. Then all parameters are held constant and the power-law exponent is increased very slightly. The entire simulator is run again for vertical flow; such a set of runs is plotted in Figure 29 for oil production rate versus time. In the runs plotted in Figure 29, the vertical and horizontal core simulations produced similar results, the major difference being the rate of drop in oil production following breakthrough. Oil production falls more rapidly in the horizontal case, primarily reflecting the rapid increase in water production that occurs.

These simulators are both for completely homogeneous one-dimensional flooding processes; no channeling or fingering effects can possibly be introduced. Yet, the results are somewhat similar to what might be predicted when water channeling occurs parallel to bedding. Once water breaks through on the horizontal simulation, the oil production falls rapidly and water production rises. This can be demonstrated by plotting results of the same simulation runs, but this time looking at the water-oil ratio versus time, as shown in Figure 30. As the waterflood matures over years, a distinct difference in water-oil ratios occurs. At a given time, the vertical flood has a much lower water-oil ratio. Such a result is simulated by a lower slope on the oil relative permeability power-law curve.

Table 2. Buckley-Leverett simulator sample.

Input Parameters:

width: 300 feet
length: 1000 feet
thickness: 20 feet
porosity: 0.2

Swc: 0.3
Swi: 0.3
Sor: 0.2
kro: alpha1 = 1.
m = 1.9
krw: alpha2 = 1.
n = 3.

Oil viscosity: 2 cp.
Water viscosity: 1 cp.
Oil FVF: 1 bbl/STB
Water FVF: 1 bbl/STB

Constant pressure drop case:
delta P = 500 psi
kabs = 200 md.

Calculated Parameters:

pore volume: 213713 bbl

Swf: 0.6466
Swbar: 0.7017
Wid @ bt: 0.40159 PV
Npd @ bt: 0.40170 PV
initial fw: 0

Msbar: 1.037
Msend: 2

Disp Eff @ bt: 80.34%

Simulation Results:

time (days)	Qt	Qo (STB/day)	Qw	dP (psi)	WOR	Wid (pv)	Npd	vis. (cp)	Edisp (%)	Esweep (%)
0	338	338	0	500	0	0	0	2	80	0
25	340	340	0	500	0	.04	.04	1.99	80	10
51	341	341	0	500	0	.08	.08	1.98	80	20
76	343	343	0	500	0	.12	.12	1.97	80	30
101	345	345	0	500	0	.16	.16	1.96	80	40
125	347	347	0	500	0	.20	.20	1.95	80	50
150	348	348	0	500	0	.24	.24	1.94	80	60
175	350	350	0	500	0	.28	.28	1.93	80	70
199	352	352	0	500	0	.32	.32	1.92	80	80

Table 2. (continued)

time (days)	Qt	Qo (STB/day)	Qw	dP (psi)	WOR	Wid (pv)	Npd	vis. (cp)	Edisp (%)	Esweep (%)
223	354	354	0	500	0	.36	.36	1.91	80	90
247.6	356	356	0	500	0	.40	.40	1.90	80	100
248	356	49	307	500	6	.40	.40	1.90	80	100
300	382	39	343	500	9	.49	.41	1.77	83	100
367	411	31	380	500	12	.62	.42	1.65	85	100
453	441	23	418	500	18	.79	.43	1.53	87	100
566	474	17	457	500	27	1.03	.45	1.43	89	100
722	508	12	496	500	42	1.39	.46	1.33	91	100
948	542	8	535	500	71	1.94	.47	1.25	93	100
1305	577	4	572	500	134	2.88	.47	1.17	95	100

Qt = total flow (STB/day)

Qo = flow of oil

Qw = flow of water

dP = pressure differential

WOR = water-oil ratio

Wid = cumulative water injected

Npd = oil produced by displacement

vis = viscosity

Edisp = displacement efficiency

Esweep = sweep efficiency

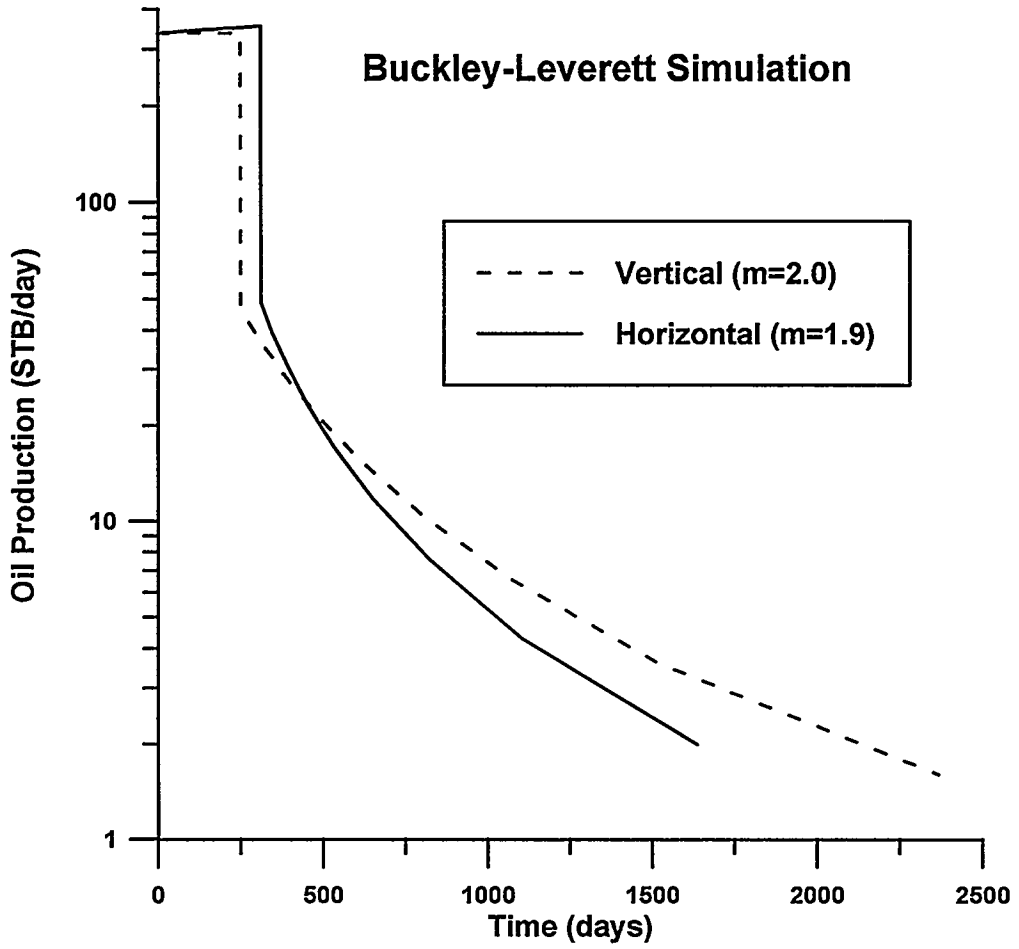

Figure 29. Oil production versus time output from Buckley-Leverett simulator run to a time when the water-oil-ratio (WOR) exceeds 300. Vertical and horizontal runs through simulator were identical in every parameter except for the exponent on the oil relative permeability power law function.

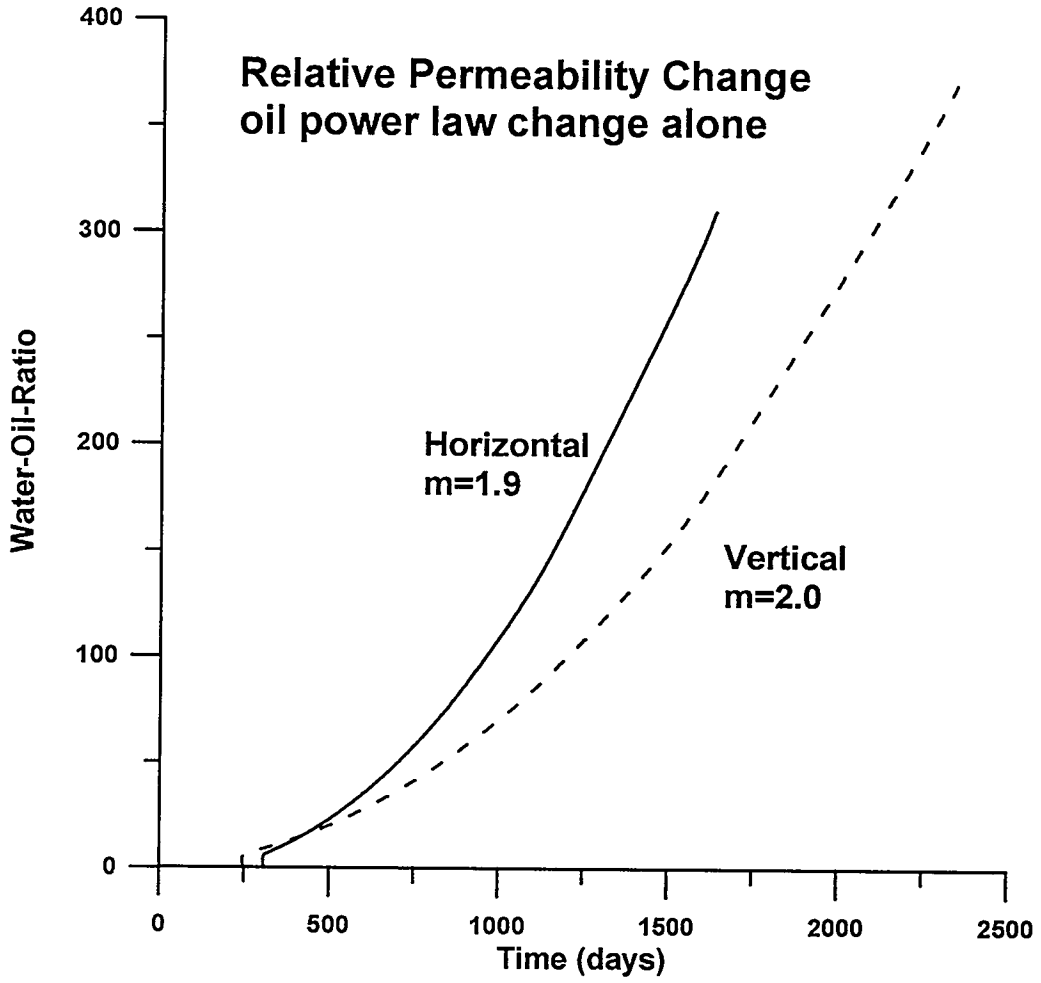

Figure 30. WOR versus time, same simulator run as in Figure 29. Although breakthrough occurs earlier in the vertical relative permeability model, the water-oil-ratio does not increase as fast as in the horizontal simulation run.

Summary

Very slight changes in relative permeability functions can create distinct differences in predicted oil and water recovery as a function of time. At this point in the project, only the slope of the oil relative permeability curve has been varied to demonstrate results consistent with the observations of relative permeability anisotropy measurements. The lower slope on a vertical than a horizontal core simulation creates the desirable characteristic of lower water-oil ratio at late times in the flood. In most mature waterfloods, the "most limiting" factor on production is high water cuts. When over 99% water cut is reached (a water-oil ratio of 99 bbl water per bbl of oil), many floods become uneconomic due to the costs of handling and recycling water in the field. If a slightly lower water-oil ratio could be achieved, then waterflooding economics could be greatly enhanced.

Future Plans

Reservoir simulations will continue, in an attempt to reach consistency with the ongoing observations of relative permeability anisotropy laboratory measurements. In particular, simulations to match the trend of producing a higher fraction of the recovered oil prior to water breakthrough will be attempted. This is another factor critical in practice, as it greatly impacts economics. Oil recovered at the beginning of a flood is more valuable than late oil due to time-value-money discount factors and operating expenses. Low water-oil ratios are also desirable as described above, but not necessarily at the expense of loosing early oil production. A balance must be achieved to optimize the economics of waterflooding. Some rough economic factors will be added to simulation runs as we relate our results to field operations now in progress in Tensleep oil producing reservoirs in Wyoming.

RELATIVE PERMEABILITY AND IMAGE ANALYSIS

Relative permeability measurements on the core plugs collected during the first year of the contract are complete. Table 1 summarizes the status of all samples used to date in the measurement of relative permeability. Thirty-four plugs from the first contract year were collected and successfully measured for relative permeability. Thin section billets were cut from these plugs for the scanning electron microscope (SEM) image analysis study.

Core plugs for the remainder of the relative permeability measurements were taken during this summer's field season (1995), to supplement the plugs from last years field work. Twenty six plugs were taken from outcrops in the Wind River and Bighorn Basins. These plugs were chosen to represent the range of sedimentologic features found in the Tensleep (see Figure 31). They are currently being prepared for relative permeability testing. Table 3 summarizes the sedimentologic features that will be examined in the relative permeability measurements. As with the plugs whose testing is completed, the plugs obtained this summer will also be made into thin sections for SEM image analysis studies.

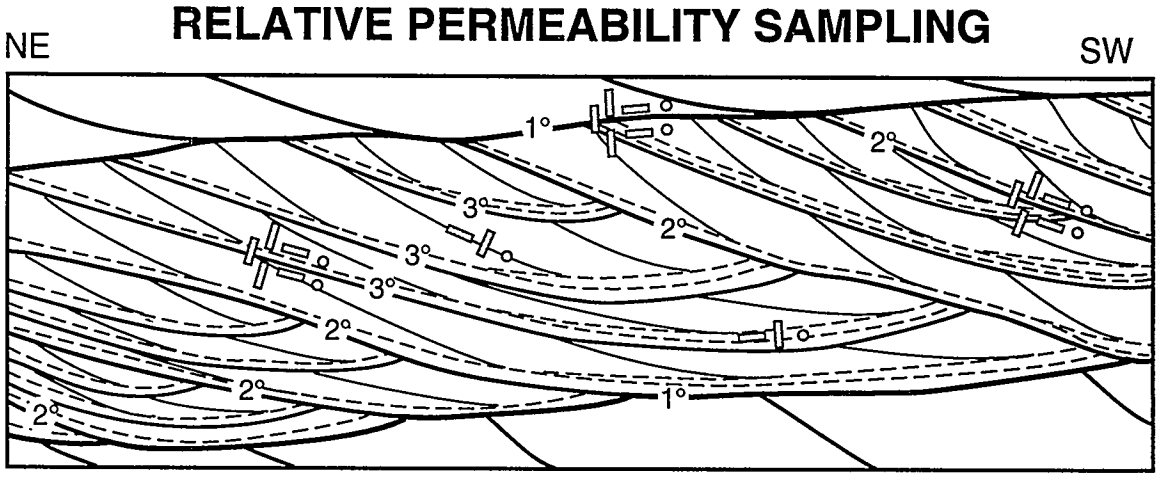

Figure 31. Schematic diagram of internal stratification and sampling scheme for the relative permeability study. Sampling in 1994 concentrated on determining the relative permeability of stratification types, such as wind-ripple and grainflow laminae. In 1995 different types of erosional bounding surfaces were sampled.

By the completion of this study, a minimum of sixty plugs will have been evaluated for relative permeability. Because of the substantial number of cores that are omitted due to channeling, cracks, or sampling problems and the need to produce a usable and unbiased database, sample collection of plugs from subsurface cores will continue through the fall.

Also during this summer's field season, samples were collected for use in the SEM image analysis study only. Samples were taken of specific sedimentologic features that, when a relative permeability prediction algorithm is developed, will better define the effects of each fabric on fluid flow. These samples have been prepared for and are being made into thin sections for the study (Table 4).

Early in the study, it was recognized that plucked grains can greatly change the pore size distribution seen in image analysis (Figure 32). To avoid these effects, precautions have been taken in the preparation of the thin section billets. Work by Pittman (1991) points out that during the preparation of thin sections, grains may be plucked from the billet

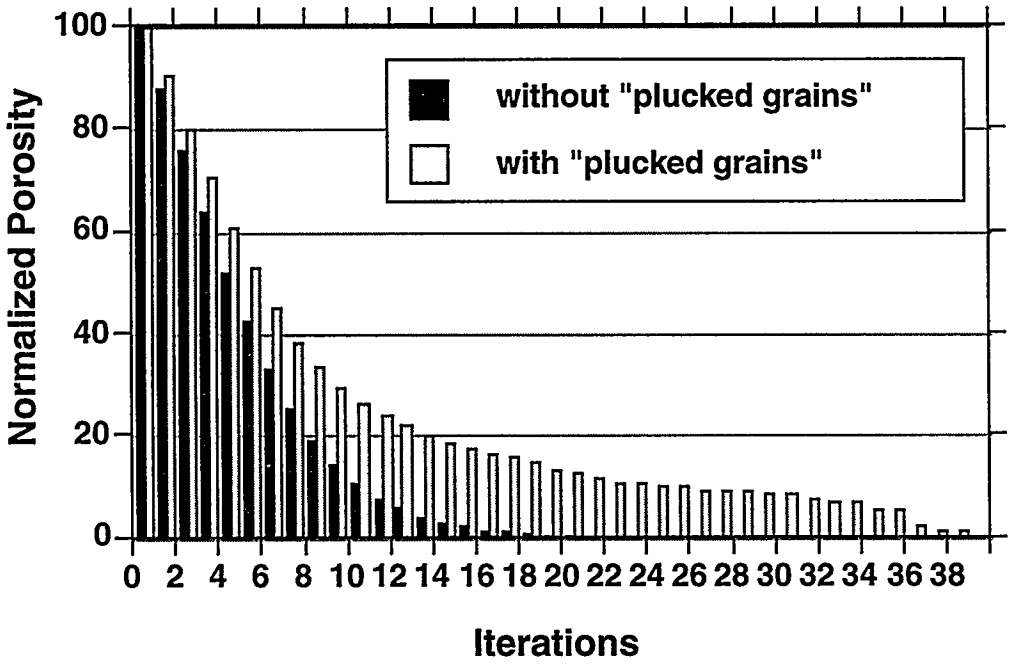

Figure 32. Comparison from Wertz 133 horizontal sample at 6872', showing the effect of plucked grains on pore-size distribution.

faces. The void left by the plucked grains may later falsely be interpreted as oversized or moldic pores. Pittman recommends that the "damage zone " be removed through grinding the billet, states that grinding the billet to a depth equal to one grain diameter is sufficient to remove the damage zone.

All of the billets were pressure impregnated with epoxy and ground at the University of Wyoming before being made into thin sections. Because the average grain size of the Tensleep Sandstone is between 100 and 150 microns, it was determined that grinding .5 mm (more than three grain diameters) from the face of the billet would be sufficient to avoid artifact porosity. By removing all artifact porosity, we get an accurate representation of the pore size distribution in the Tensleep and a true understanding on how pore size distribution effects relative permeability.

SUMMARY

As more relative permeability measurements are collected and the relative permeability prediction algorithm is built, the trend in relative permeability anisotropy and heterogeneity will become more clearly defined. These trends will then be applied to the reservoir simulation model to better design efficient production techniques. Additional samples will be added to insure both usable database and to continue verification of the observed trends of relative permeability.

Table 3. Samples collected in second year for relative permeability measurements.

Sample	Core Orientation	Surface Type or Stratification	Location Name
MB-NNB1a	across surface	3° bounding surface	Mahogany Butte
MB-NNB1b	parallel to surface, above	3° bounding surface	Mahogany Butte
MB-NNB1c	parallel to surface, below	3° bounding surface	Mahogany Butte
SC-21.1a	across surface	3° bounding surface	Sinks Canyon
SC-21.1b	perpendicular to surface, above	3° bounding surface	Sinks Canyon
SC-21.1c	perpendicular to surface, below	3° bounding surface	Sinks Canyon
MB-45a	perpendicular to stratification	wind-ripple laminae	Mahogany Butte
MB-45b	parallel to stratification	wind-ripple laminae	Mahogany Butte
MB-45c	parallel to stratification	wind-ripple laminae	Mahogany Butte
CC-50a	perpendicular to stratification	wind-ripple laminae	Canyon Creek
CC-50b	parallel to stratification	wind-ripple laminae	Canyon Creek
CC-50c	parallel to stratification	wind-ripple laminae	Canyon Creek
MB-65a	across surface	2° bounding surface	Mahogany Butte
MB-65b	perpendicular to surface, above	2° bounding surface	Mahogany Butte
MB-65c	perpendicular to surface, below	2° bounding surface	Mahogany Butte
SC-22c	across surface	2° bounding surface	Sinks Canyon
SC-22f	across surface	2° bounding surface	Sinks Canyon
SC-22g	perpendicular to surface, below	2° bounding surface	Sinks Canyon
MB-NNB3a	across surface	1°bounding surface	Mahogany Butte
MB-NNB3b	perpendicular to surface, above	1°bounding surface	Mahogany Butte
MB-NNB3c	perpendicular to surface, below	1°bounding surface	Mahogany Butte
HR-75a	across surface	1°bounding surface	Holland Ranch
HR-75b	perpendicular to surface, above	1°bounding surface	Holland Ranch
CC-NNB2a	perpendicular to stratification	grainflow laminae	Canyon Creek
CC-NNB2b	parallel to stratification	grainflow laminae	Canyon Creek
CC-NNB2c	parallel to stratification	grainflow laminae	Canyon Creek

Table 4. Samples collected in second year for SEM image analysis studies

Sample	Surface Type or Stratification	Location Name
MB-18	3° bounding surface	Mahogany Butte
MB-40	3° bounding surface	Mahogany Butte
SC-22	2° bounding surface	Sinks Canyon
SR1-3	wind-ripple laminae	Slip Road
MB-70	3° bounding surface	Mahogany Butte
MB-30	wind-ripple laminae	Mahogany Butte
MB-20	3° bounding surface	Mahogany Butte
MB-60	2° bounding surface	Mahogany Butte
MB-35	wind-ripple laminae	Mahogany Butte
CC-45	1° bounding surface	Canyon Creek
SC-80	2° bounding surface	Sinks Canyon

TASK 3.0 - CO_2 FLOOD - FORMATION ALTERATION AND WELLBORE DAMAGE

Ryoji Shiraki - Task Leader

OBJECTIVES

The work of this task is to establish criteria for the susceptibility of Tensleep reservoirs to formation alteration resulting in changes in absolute or relative permeability, and to establish possible characterization technology to be used to optimize recovery efficiency. This task includes (a) flow experiments on core material to examine the effects of CO_2 flooding on the fluid and rock system, (b) examination of regional trends in water chemistry, (c) examination of local water chemistry trends at field scale, and (d) chemical modeling of both reservoir and experimental systems in order to scale the experiments to reservoir conditions.

SUMMARY

We have compiled water chemistry data on 417 Tensleep, 191 Madison, and 208 Phosphoria Formation water samples and have found that those waters can be classified into four types on the basis of chemistry: Ca-Mg-HCO_3, Ca-(Mg)-SO_4, Na-SO_4, and Na-SO_4-Cl types. These water chemistries were probably formed by (1) dissolution of dolomite and anhydrite, (2) precipitation of calcite, (3) Na-Ca ion-exchange reaction with clay minerals and alteration of feldspar, (4) dissolution of halite, and (5) mixing with other formation waters. We also found a characteristic distribution of each water type in the Bighorn Basin, and these distributions may reflect the effect of hydrology on formation water chemistry in the Bighorn Basin.

We found through computer simulation that formation water chemistry does not greatly affect the potential for carbonate scale formation, unless water-rock interaction takes place. However, simulation suggests that dolomite dissolution raises the potential for aragonite scale formation considerably, and that anhydrite precipitation lowers the potential due to consumption of Ca when the solution is saturated or supersaturated with respect to anhydrite.

In two CO_2 core flooding experiments, we confirmed that dolomite dissolved into acidic solution with high concentration of CO_2 gas. As we used a solution that was initially saturated with respect to anhydrite, the Ca concentration remained constant during the runs, despite dolomite dissolution, suggesting anhydrite precipitated at the same time. These observations are consistent with the results of computer simulation of scale formation. Our experiments, however, reproduced the conditions only near the injection well, so the experimental solutions remained undersaturated with respect to scale forming minerals. Thus, we need to be able to accurately estimate how fast the CO_2 flood plus formation water reaches saturation with respect to the scale minerals, and we need to acquire kinetic data on mineral-water reactions for adequate forward modeling of scale formation accompanying CO_2 flooding.

FUTURE PLANS

Next year, we will focus on understanding the regional water chemistry and chemical modeling of Tensleep Formation waters using the data we have compiled. We will try to understand petrographic and porosity features, and to establish evaluation criteria for risk of scaling and formation damage accompanying CO_2 treatment. We will pursue two additional CO_2 flooding experiments next year. In these runs, we will use a brine that is initially undersaturated with respect to anhydrite. We have found through prior experiments that the Ca content of a solution was kept constant due to precipitation of anhydrite despite dolomite dissolution when the solution was initially saturated with respect to anhydrite. The computer simulation confirmed these results and also indicated that the dissolution of both dolomite and anhydrite into a solution that is undersaturated with respect to anhydrite will raise the potential of aragonite scale formation above the potential in a solution saturated with respect to anhydrite. This simulation result needs to be confirmed experimentally. In addition, we will run experiments on rock-oil-water-CO_2 systems in order to further examine the effect of oil on CO_2-water systems.

By synthesizing those understandings, we have to establish evaluation criteria for risk due to scaling and formation damage accompanying CO_2 treatment in the Tensleep Formation.

FORMATION WATER CHEMISTRY

During the first contract year, we compiled water chemistry data on 90 Tensleep Formation water samples in the Bighorn Basin and showed that they can be classified into two groups, termed Type A and Type B, in terms of fraction of the chemical equivalent of chloride. We saw that Type A waters are distributed mainly in the eastern side of the basin, whereas Type B waters are mainly distributed in the western side of the basin. During the second year, we located and compiled 327 additional Tensleep Formation water chemistry analyses in the Bighorn Basin, for a total of 417 water chemistry analyses compiled. We also compiled 191 water analyses of Madison and 208 analyses of Phosphoria Formation waters in the Bighorn Basin, and compared them with those of the Tensleep Formation waters.

(1) Tensleep Formation water chemistry

Figure 33 shows the water chemistry of Types A and B Tensleep Formation waters on Piper diagrams, respectively. Type A waters have the equivalent fraction of chloride, X_{Cl} (see definition below), smaller than 0.1, whereas Type B waters have X_{Cl} greater than 0.1. As shown in Figure 33, we classified Type A waters into three sub-types, termed Types A1, A2, and A3. Type A1 waters are Ca-Mg-HCO_3 type waters. Type A2 waters are Ca-Mg-SO_4 type waters. Type A3 waters are rich in SO_4, as Type A2 water are, but the major cations are not Ca and Mg but the alkalis Na and K. These are thus our Na-SO_4 type waters. Type B waters are rich in NaCl and KCl compared with Type A3 water, but

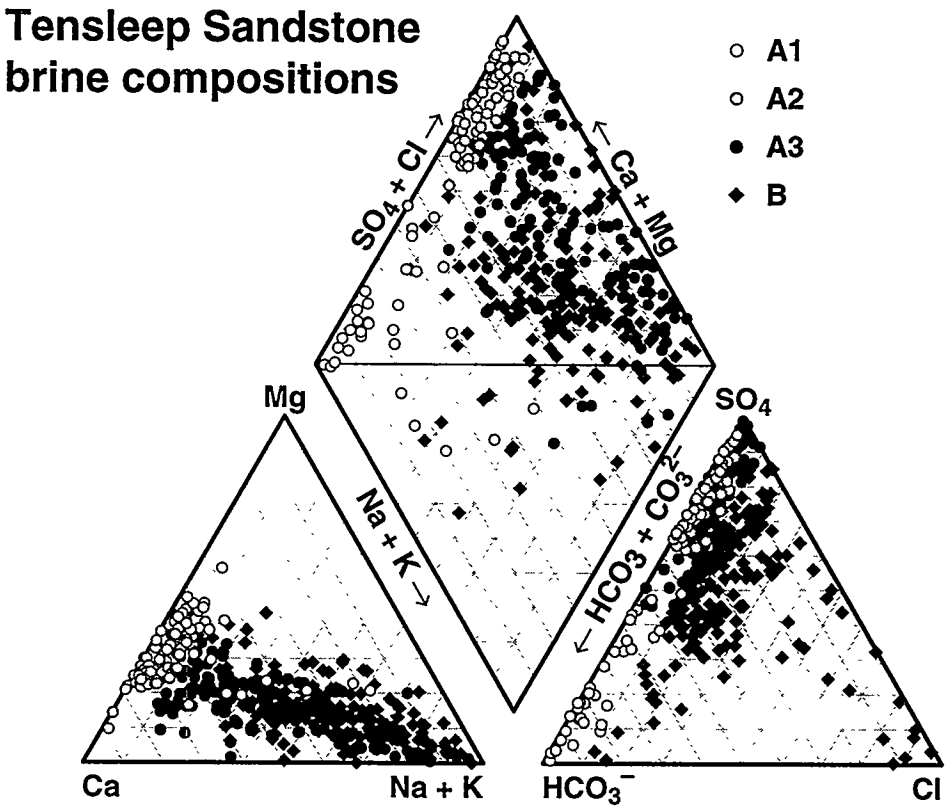

Figure 33. Chemical composition of Tensleep Formation waters.

the major anion in most Type B waters is SO4. These are our Na-SO4-Cl type waters. Our definition of each type of water is as follows:

Type A1: $X_{Cl} < 0.1$, $X_{SO_4} < 0.5$, and $X_{Na+K} < 0.1$

Type A2: $X_{Cl} < 0.1$, $X_{SO_4} > 0.5$, and $X_{Na+K} < 0.1$

Type A3: $X_{Cl} < 0.1$, $X_{SO_4} > 0.5$, and $X_{Na+K} > 0.1$

Type B: $X_{Cl} < 0.1$, no further definition

where $X_{Cl} = M_{Cl} / (M_{HCO_3} + M_{Cl} + 2M_{SO_4})$

$X_{SO_4} = 2M_{SO_4} / (M_{HCO_3} + M_{Cl} + 2M_{SO_4})$

$X_{Na+K} = M_{Na+K} / (M_{Na+K} + 2M_{Ca} + 2M_{Mg})$

where X is the equivalent fraction and M is molar concentration.

The chemical trends seen in Figures 33 are similar to major-ion evolution sequences (Chevotarev, 1955; Freeze and Cherry, 1979) and to dedolomitization, which is dissolution of dolomite and precipitation of calcite caused by the dissolution of anhydrite (Back and Hanshaw, 1970; Hanshaw and Back, 1979; Back et al., 1983; Busby et al., 1990; Plummer et al., 1990). Therefore, we also chose dissolved sulfate as a reaction-progress variable to examine water chemistry. Figures 34 and 35, which plot the relations between Ca, Mg, and SO4 in Types A1 and A2 waters, show a systematic increase in Ca and Mg as SO4 increases. As the Tensleep Formation is cemented by dolomite and anhydrite (e.g., Todd, 1966; Mankiewicz and Steidtman, 1979), these trends suggest that the water chemistry is controlled by dissolution of dolomite and anhydrite. These reactions are expressed by the following equations:

$$CaMg(CO_3)_2 = Ca^{2+} + Mg^{2+} + 2\,CO_3^{2-} \quad (1)$$

$$CaSO_4 = Ca^{2+} + SO_4^{2-} \quad (2)$$

Figure 36 shows the relation between HCO3 and SO4 in Types A1 and A2 waters. The concentration of HCO3 is almost equal to alkalinity because of the pH of the solutions (below 9, CO3 contents are negligible). Previous work on dedolomitization in carbonate aquifers has shown that alkalinity in most waters decreases as SO4 increases due to precipitation of calcite (e.g. Plummer et al., 1990). However, Type A1 waters show systematic increase in alkalinity with increasing SO4, suggesting that calcite precipitation as expressed by the equation

$$Ca^{2+} + CO_3^{2-} = CaCO_3 \quad (3)$$

does not take place. Type A2 waters also show increase in alkalinity as SO4 increases. The alkalinity of this type water is, however, much smaller than that of Type A1 water.

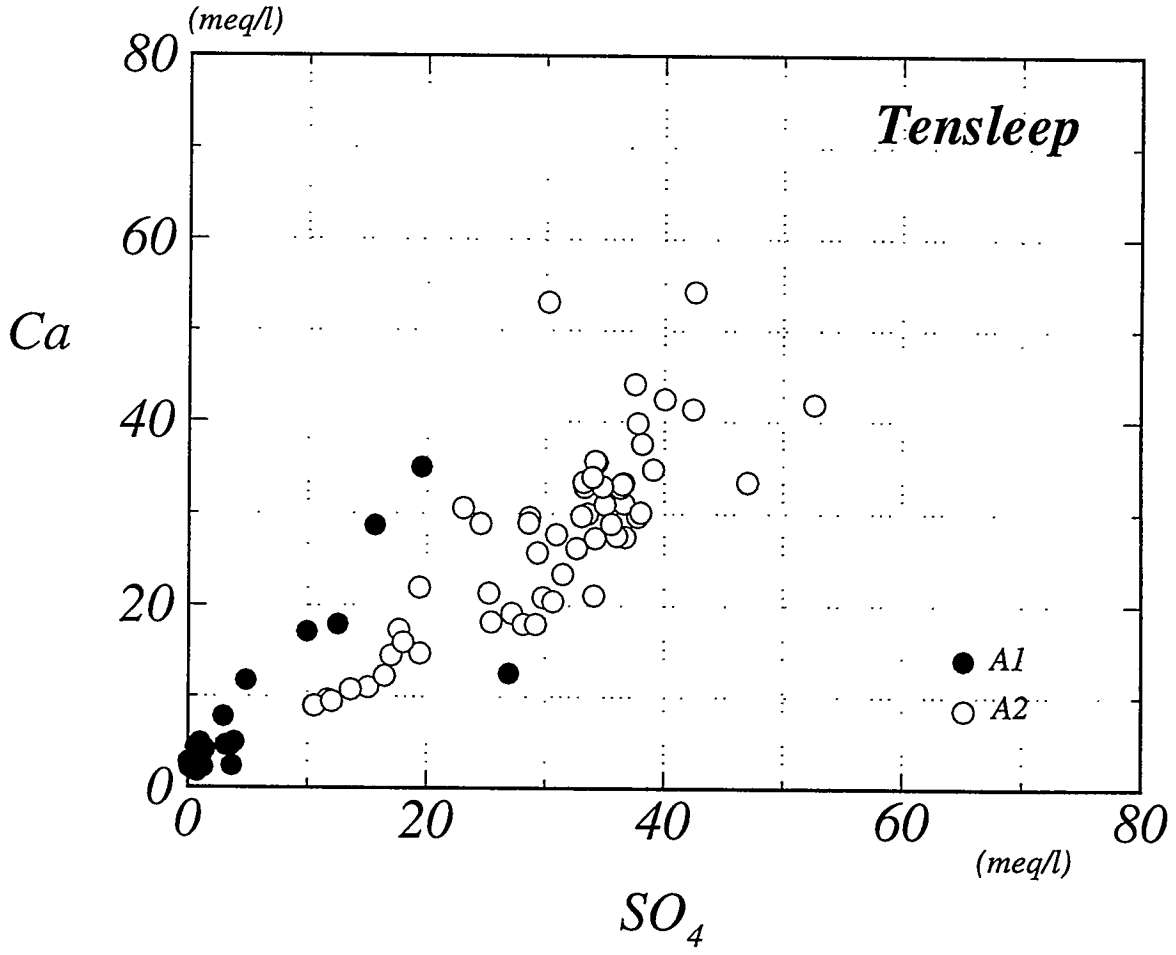

Figure 34. Ca vs. SO_4 for Types A1 and A2 of Tensleep Formation waters

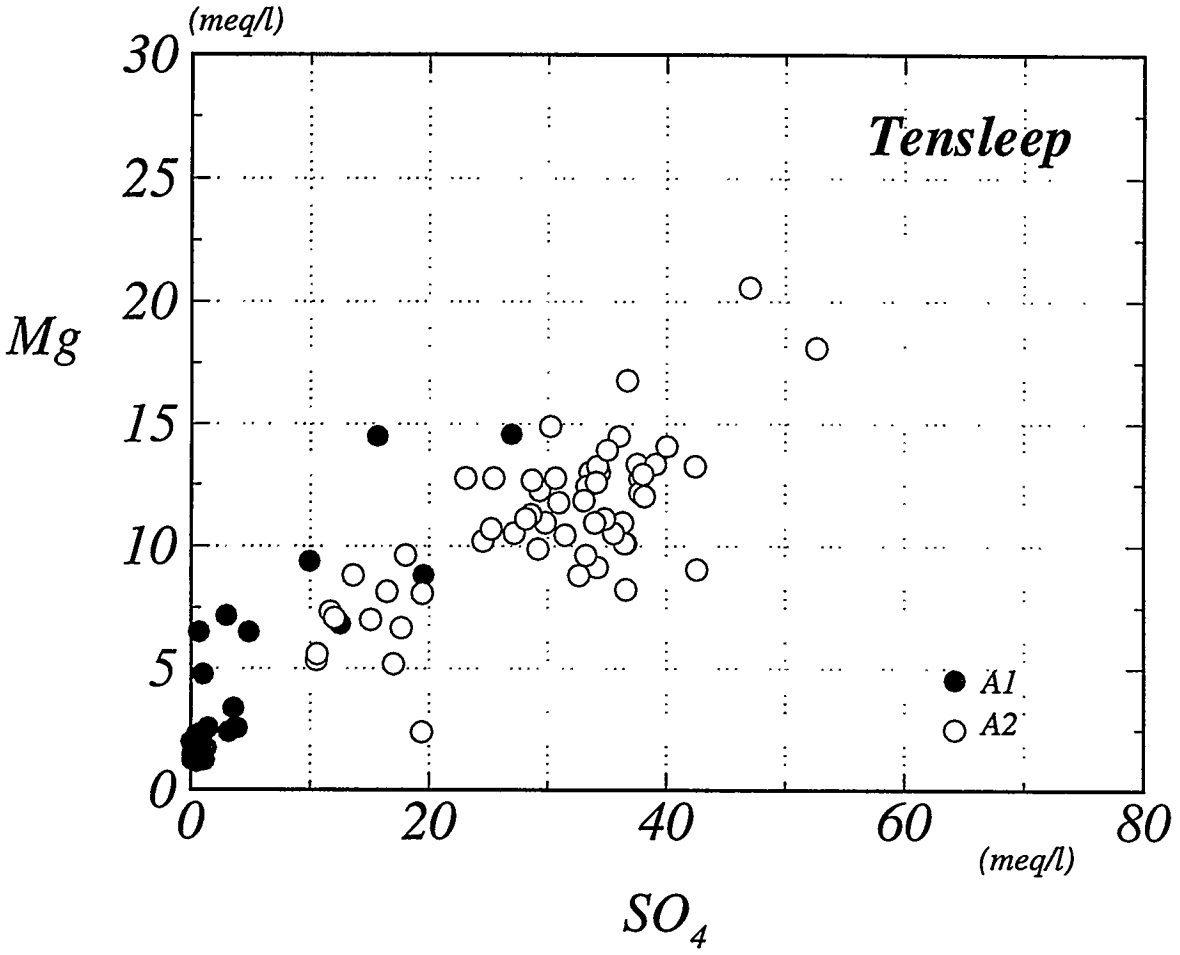

Figure 35. Mg vs. SO_4 for Types A1 and A2 of Tensleep Formation waters

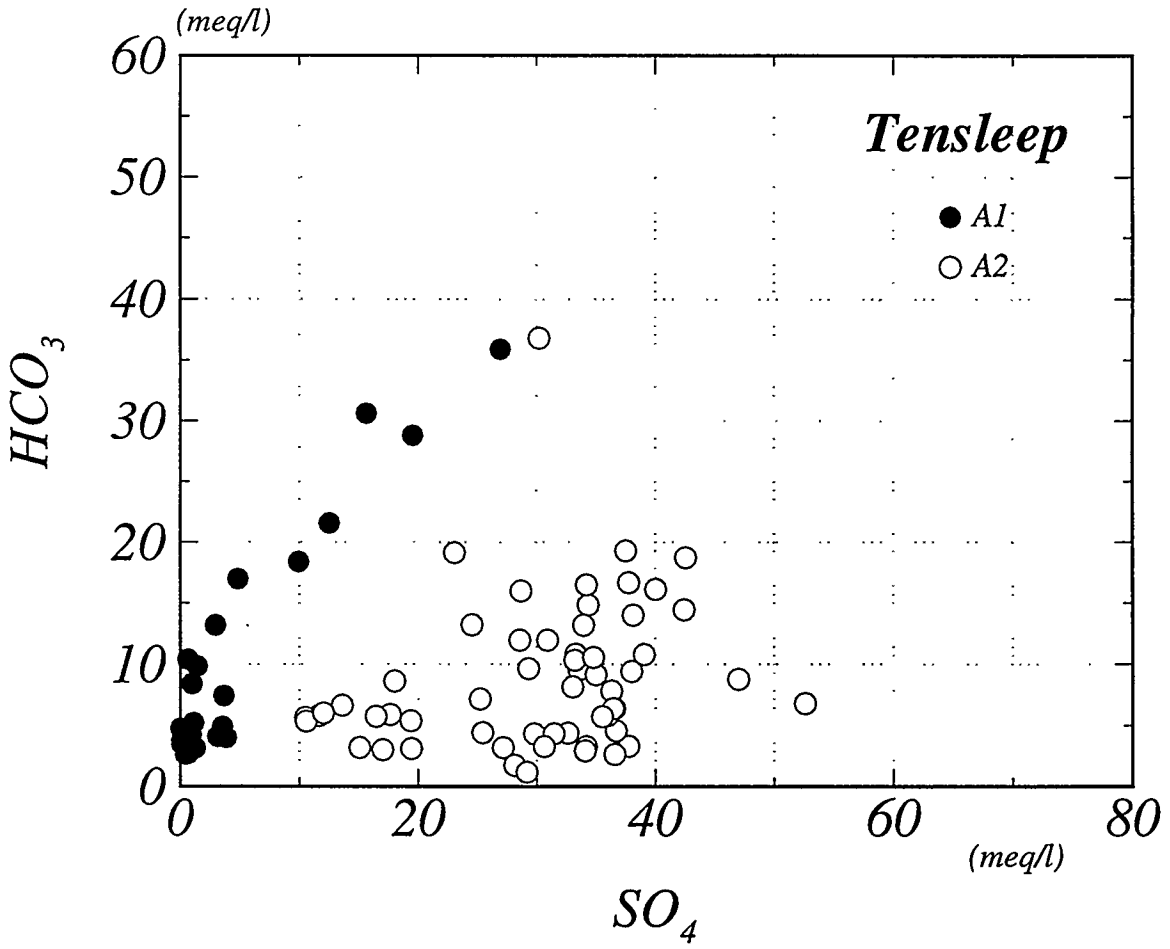

Figure 36. HCO_3 vs. SO_4 for Types A1 and A2 of Tensleep Formation waters

Thus, Type A2 water chemistry might be controlled by calcite precipitation as well as dissolution of dolomite and anhydrite [Equations (1) and (2)].

Figure 37 shows a good correlation between alkali (Na + K) and SO_4 in Types A3 and B waters. This relation can be explained by the following reactions:

$$Na - clay + Ca^{2+} = Ca - clay + 2Na^{+} \quad (4)$$

$$Ca^{2+} + 2NaAlSi_3O_8 + 2H_2O + CO_2 = CaCO_3 + Al_2Si_2O_5(OH)_4 + 4SiO_2 + 2Na^{+} \quad (5)$$

Equation (4) shows an ion exchange reaction between the Ca^{2+} released by reactions (1) and (2) and Na^{+} (+ K^{+}) in clay minerals. Equation (5) shows the alteration of feldspar to form calcite, kaolinite, and quartz; this reaction consumes Ca^{2+} and produces Na^{+}, as well. Sakai and Matsubaya (1974) reported a reaction similar to Equation (5) to explain the origin of Na-Cl-SO_4 type thermal waters in the Green-Tuff region of Japan. The alkali content of Type B waters is slightly higher than that of Type A3 waters at constant SO_4 content, suggesting these waters are formed by dissolution of halite into Type A3 waters or mixing of connate seawater with Type A3 waters.

Figure 38 shows the distribution of each water type of the Tensleep Formation in the Bighorn Basin. The map shows that Types A2 and A3 waters are distributed along the eastern margin of the basin, whereas Type A1 waters are distributed along the southeastern edge of the basin, and that most Type B waters are distributed on the western side of the basin.

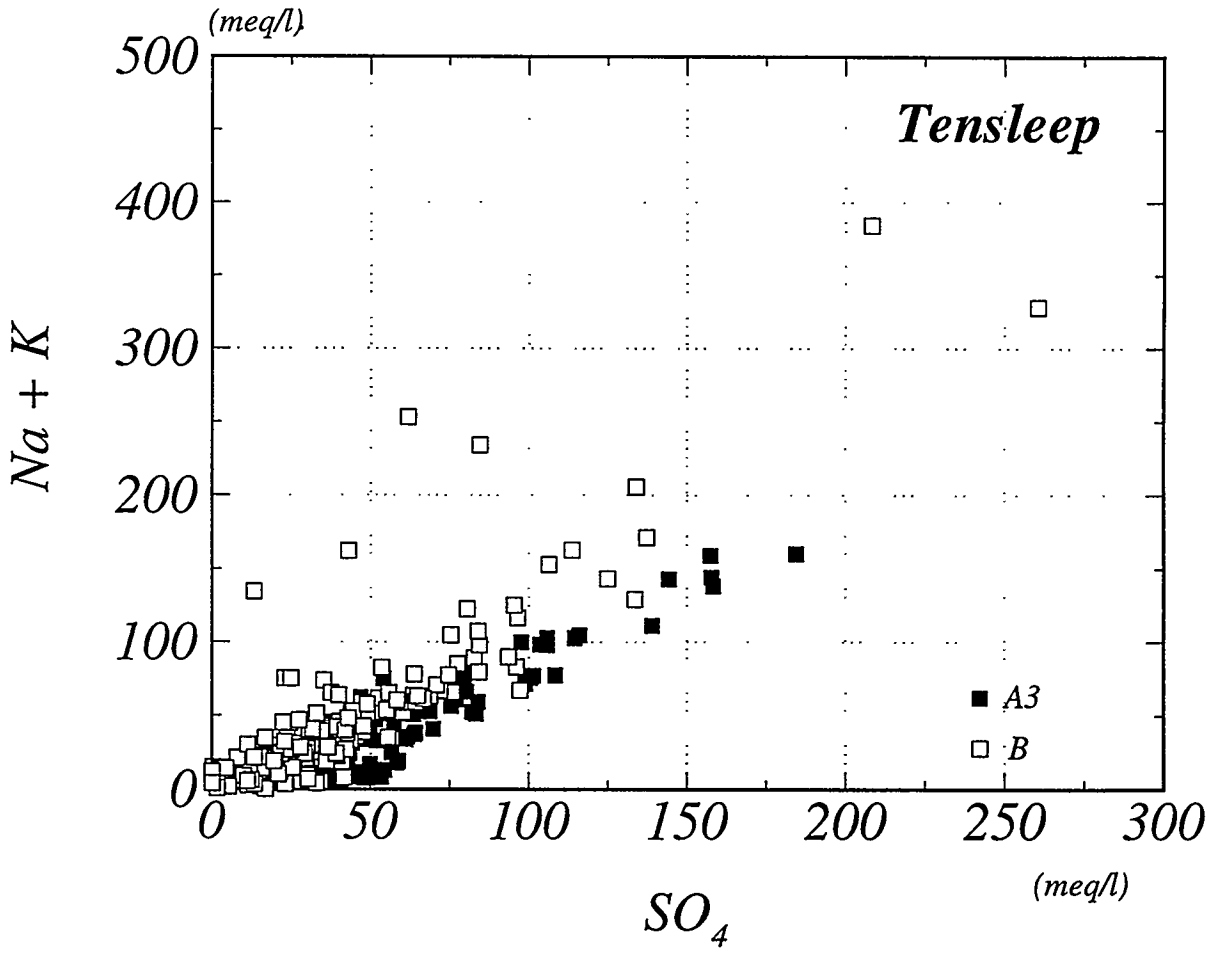

Figure 37. Na + K vs. SO_4 for Types A3 and B of Tensleep Formation waters

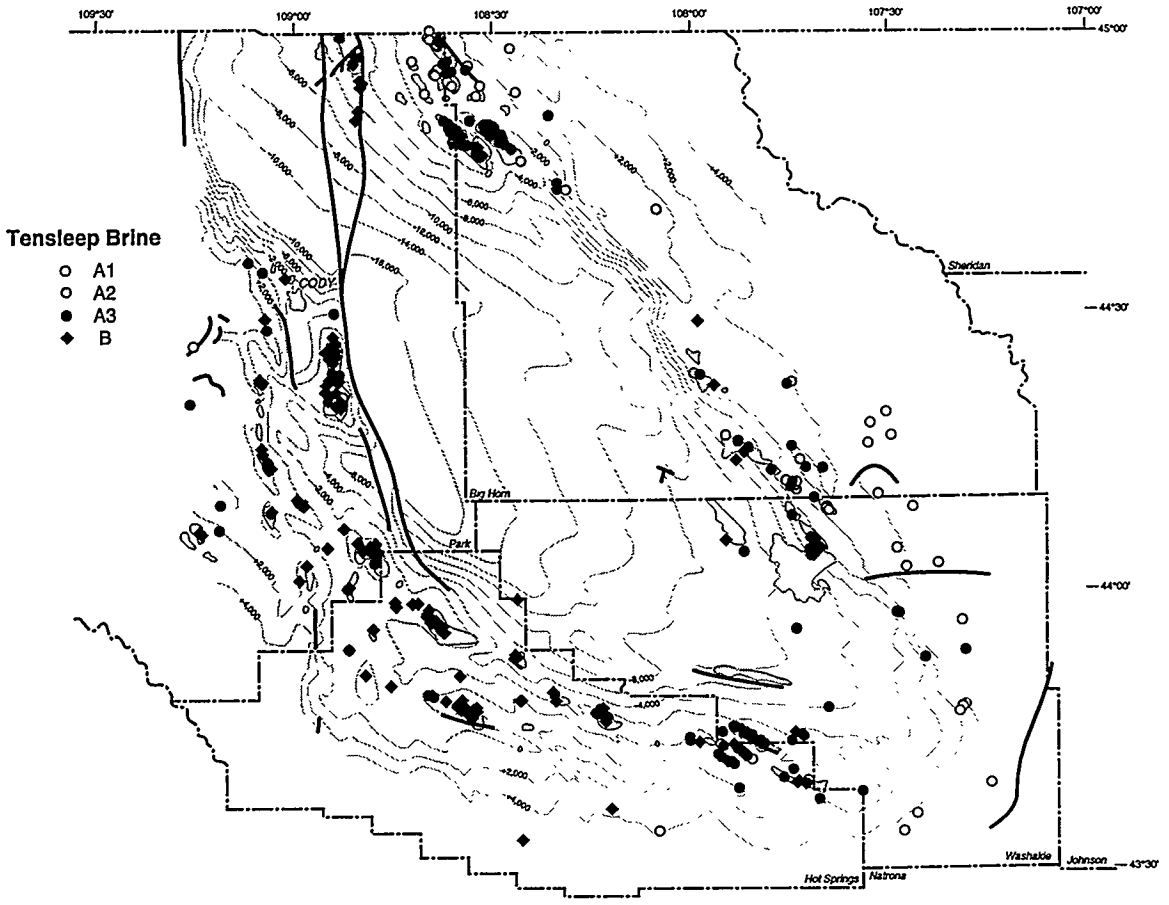

Figure 38. Distribution of Tensleep Formation waters in the Bighorn basin. Contours and shaded areas show the top of the Permo-Pennsylvanian Phosphoria and Minnelusa Formations and Tensleep oil fields, respectively, (WGA, 1989).

(2) Tensleep Formation water chemistry at Teapot Dome oil field

In November 1994, we (Drs. Ryoji Shiraki and Thomas L. Dunn) collected six water samples from the Tensleep Formation and one sample from the Madison Formation at Teapot Dome oil field. This oil field was chosen as a sampling site because of its primary production from the Tensleep and Madison Formations.

All samples were collected at the well-heads. Four of the water samples (three Tensleep, one Madison) were filtered, and their pH and alkalinity were measured on site by a combination pH electrode and titration with H_2SO_4, respectively. The measurements on

the other three samples were carried out at the University of Wyoming next day. Chemical analyses were performed at the University of Wyoming by ICP and atomic absorption spectrometry for cations and by ion chromatography for anions, organic acids, and sulfides.

Figure 39 shows the major element composition of the seven water samples collected on a Piper diagram. The six Tensleep Formation waters and the Madison Formation water have quite similar compositions, although the Madison Formation water has slightly less (Na + K) and Cl than the Tensleep Formation waters. All the waters are classified Type B in terms of our definition. The range of total dissolved solids (TDS) of

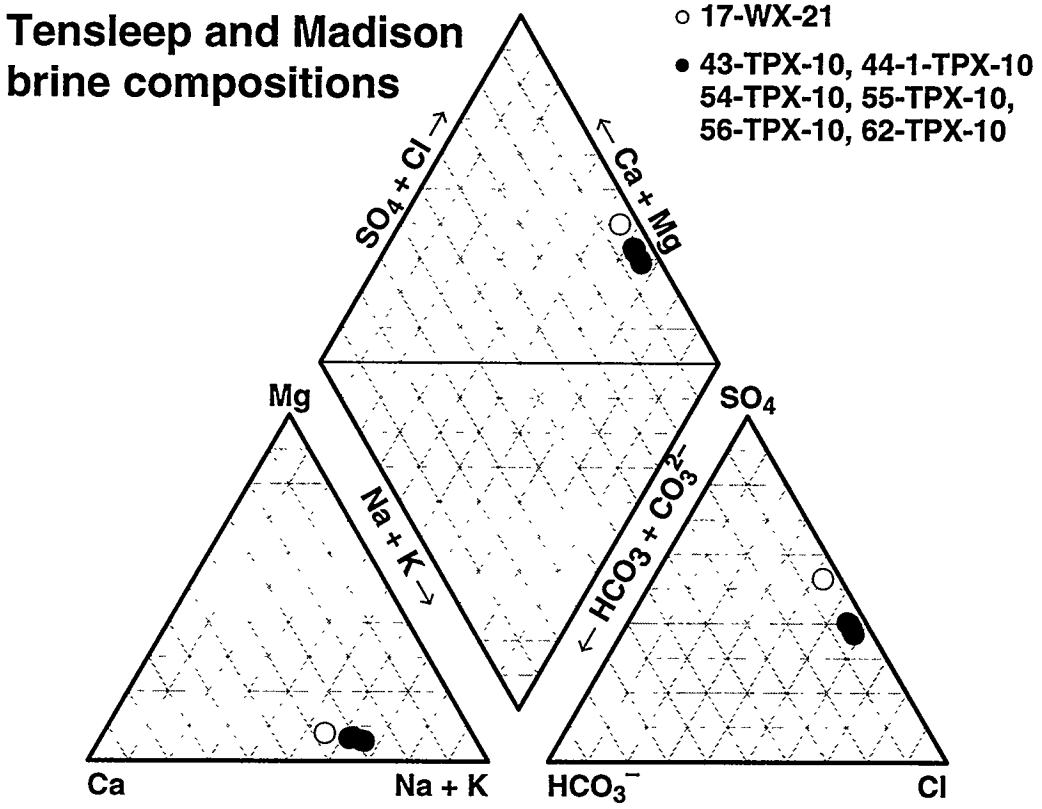

Figure 39. Chemical composition of Tensleep and Madison Formation waters at Teapot Dome oil field.

Tensleep Formation waters was from 3120 to 3448 mg/l, and the TDS of the Madison Formation water was 2832 mg/l. The concentration of hydrogen sulfide and organic acids (oxalate, formate, acetate, propyonate, and butyrate) were all below their detection limits.

Table 5 summarizes the results of chemical modeling of these waters using the *SOLMINEQ.88* computer program (Kharaka et al., 1988). A reservoir temperature of 92.2^{o}C was adopted for all wells; that was the highest bottom-hole temperature (BHT) obtained from logs of those wells. Pressure was calculated from the perforation depth (PD) under the assumption that all the wells are normally pressurized. The perforation

Table 5: Saturation index of minerals of Tensleep and Madison Formation waters at Teapot Dome oil field, Wyoming

Sample	anhydrite	gypsum	barite	celestite	calcite	aragonite	dolomite	quartz
43-TPX-10	0.265	0.517	0.108	0.418	0.476	0.382	1.04	0.144
44-1-TPX-10	0.255	0.508	0.102	0.429	0.685	0.590	1.42	0.142
54-TPX-10	0.248	0.501	0.067	0.408	0.612	0.518	1.30	0.141
55-TPX-10	0.255	0.509	0.057	0.471	0.655	0.560	1.37	0.157
56-TPX-10	0.247	0.500	0.040	0.537	0.685	0.591	1.42	0.203
62-TPX-10	0.242	0.495	0.073	0.417	0.563	0.468	1.19	0.158
17-WX-21	0.157	0.409	0.035	0.528	0.424	0.329	0.936	0.113

Sample 17-WX-21 is from the Madison the rest are Tensleep samples.

depths of the Tensleep Formation wells were between 5360 and 5492 ft, and that of the Madison Formation well was 5616 ft. In the end, hydrostatic pressures for those wells used for chemical modeling were from 160 to 168 bars.

The model calculation showed that Tensleep Formation waters are nearly saturated with respect to anhydrite, barite, and quartz at the assumed reservoir T-P conditions. The TDS values of these Tensleep Formation waters are greater than 3000 mg/l, and the fact that these waters are nearly saturated with respect to anhydrite is consistent with the saturation index of anhydrite of the Tensleep Formation waters in the Bighorn Basin, which we compiled during the first contract year (see Figure 24; Dunn, 1994). Saturation

with respect to barite of all solutions is probably due to the low solubility product of this mineral.

These waters are also highly supersaturated with respect to carbonate minerals, in particular to dolomite. Much water vapor was released from the water samples when they were collected at well heads in the field. Therefore, a fair amount of carbon dioxide must have outgassed from the sample solutions at that time, and increase of pH of the solutions must have resulted. Sholkovitz (1973) reported that the saturation indices of carbonate minerals are quite sensitive to solution pH. Thus, the calculated saturation indices of carbonate minerals may be overestimated.

(3) Madison Formation water chemistry

Figure 40 shows the Madison Formation water chemistry in the Bighorn Basin on a Piper diagram. We applied our classification of water chemistry for Tensleep Formation waters (i.e., Types A1, A2, A3, and B) to Madison Formation waters as well. The figure suggests that Madison Formation waters also can be classified into these types. Figures 41 and 42 show Ca and Mg vs. SO_4 and alkalinity vs. SO_4 of Types A1 and A2 Madison Formation waters, respectively. Both Ca and Mg increase as SO_4 increases, and this trend is quite similar to that of Types A1 and A2 Tensleep Formation waters (see Figures 34 and 35). The alkalinity of Madison Formation waters, however, decreases as SO_4 increases, which is the reverse trend of Tensleep Formation waters (see Figure 36). This difference can be explained by the fact that the Madison Formation is a carbonate aquifer whose main mineral constituent is calcite. Dissolution of dolomite and anhydrite shown by Equations (1) and (2) may result in supersaturation with respect to calcite. Supersaturation with respect to calcite causes precipitation of the mineral, resulting in a decrease of alkalinity and further dissolution of dolomite and anhydrite. This is a typical mechanism of dedolomitization in carbonate rocks (Back and Hanshaw, 1970; Hanshaw and Back, 1979; Back et al., 1983; Busby et al., 1990; Plummer et al., 1990).

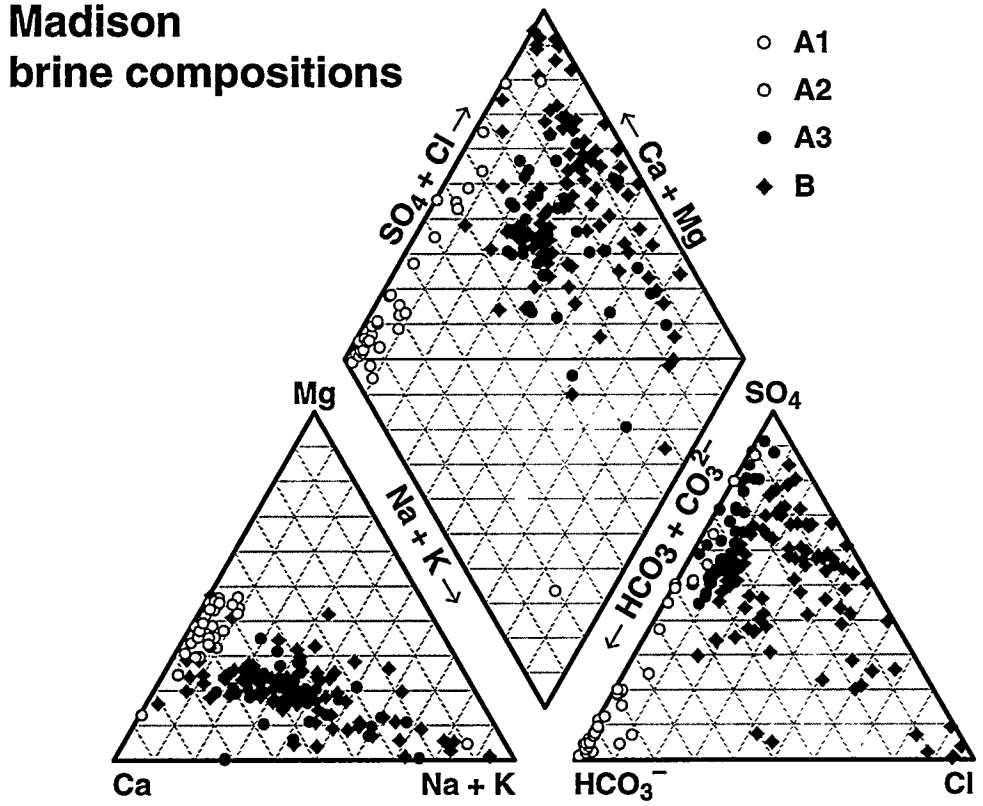

Figure 40. Chemical composition of Madison Formation waters.

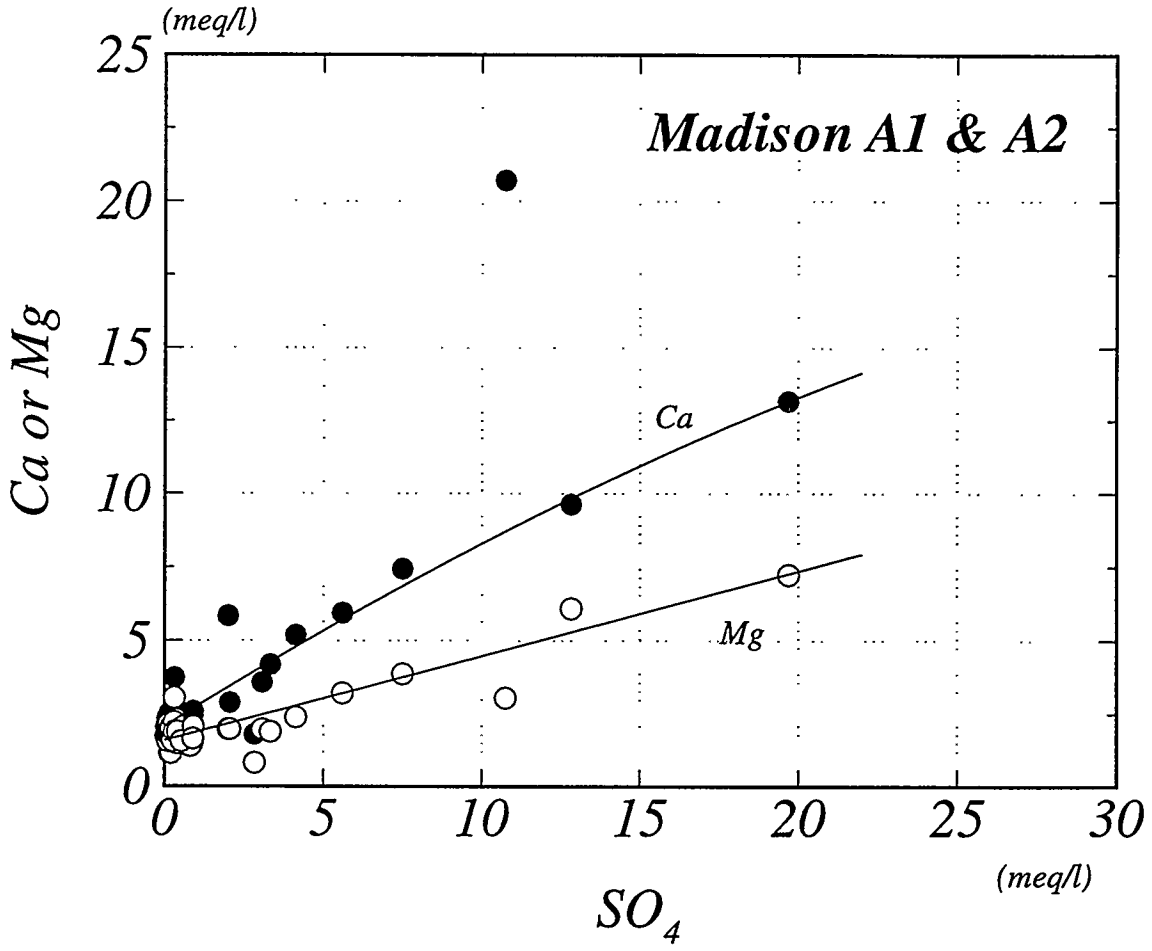

Figure 41. Ca or Mg vs. SO_4 for Types A1 and A2 of Madison Formation waters

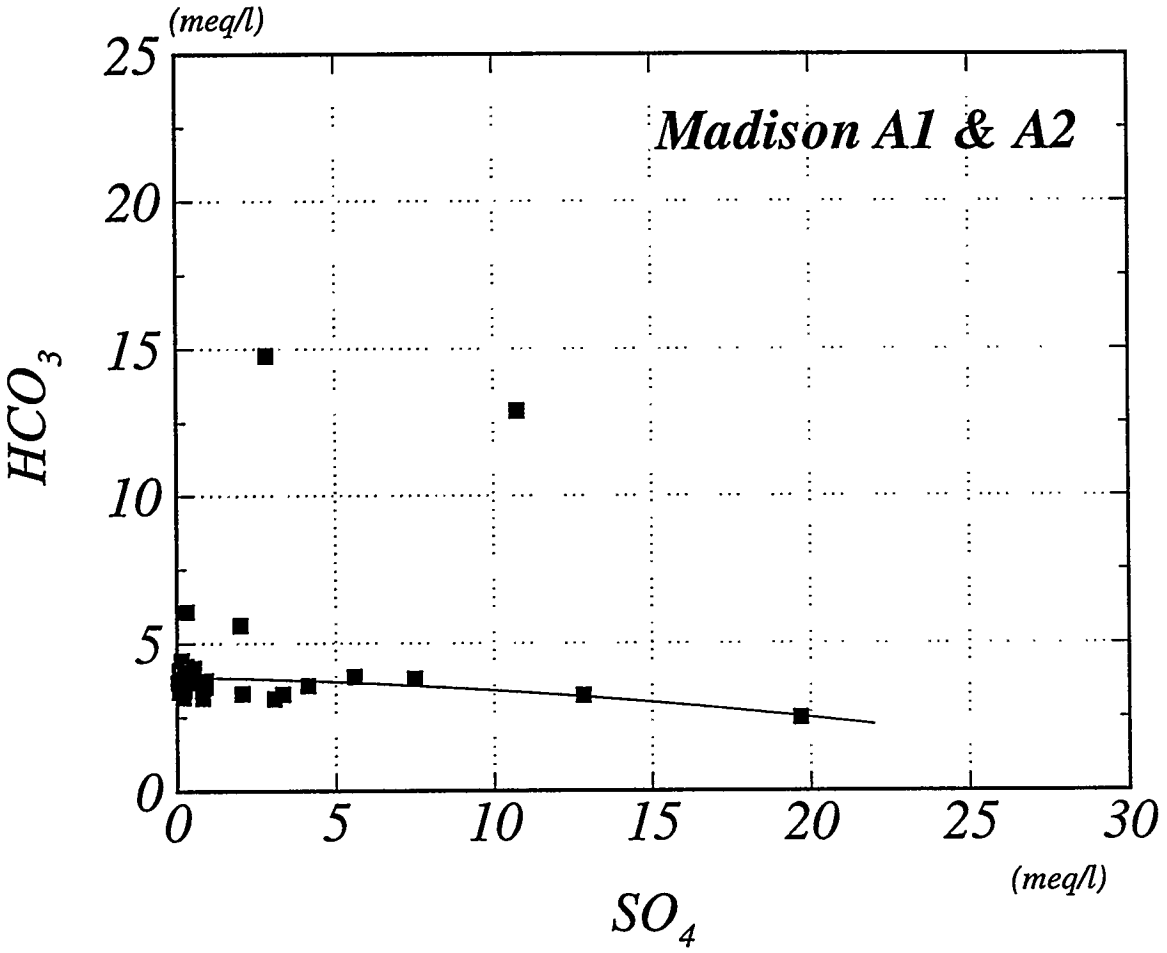

Figure 42. HCO_3 vs. SO_4 for Types A1 and A2 of Madison Formation waters

Figure 43 shows the distribution map of each water type of the Madison Formation in the Bighorn Basin. Type A1 waters of the Madison Formation are distributed mainly on the northeastern margin of the basin, whereas Type A1 waters of the Tensleep Formation are distributed on the southeastern margin of basin. Distribution of the other water types is similar to that of Tensleep Formation (see Figure 38).

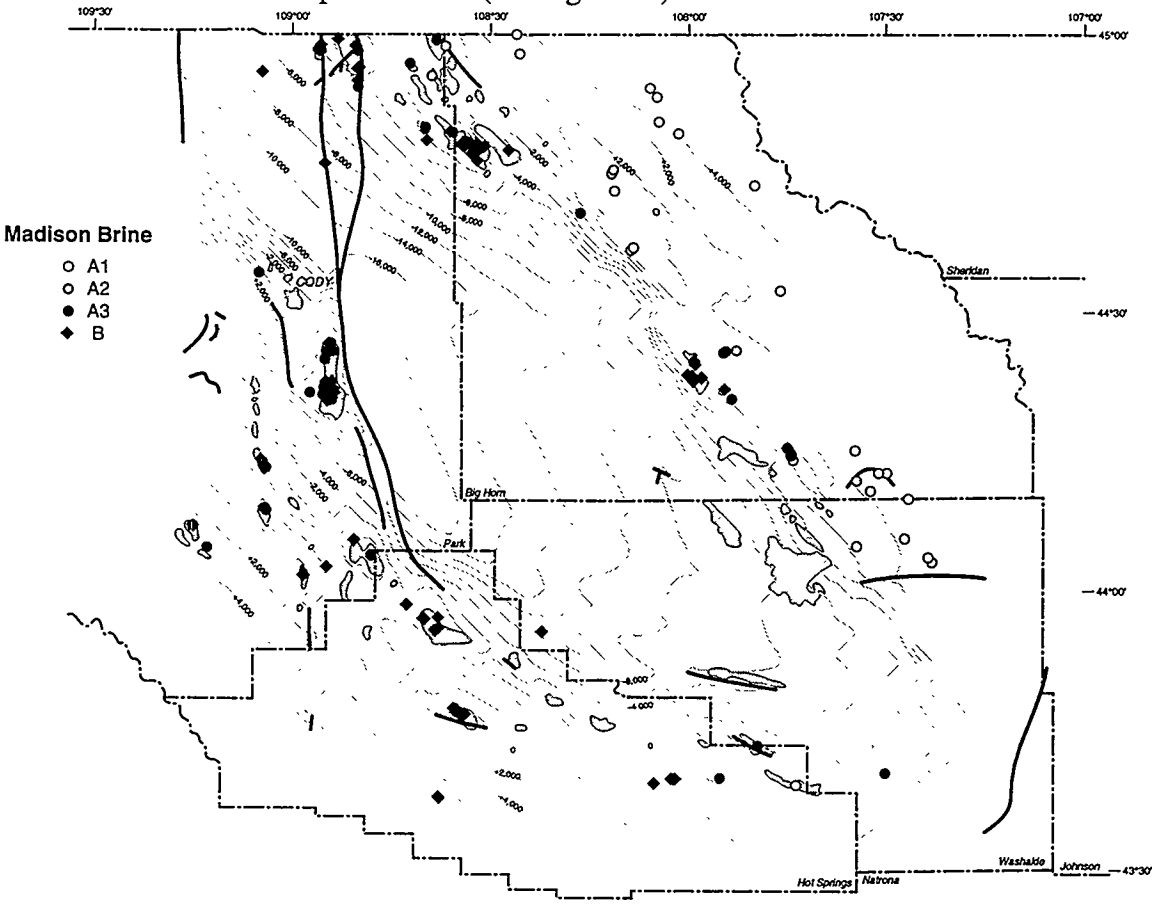

Figure 43. Distribution of Madison Formation waters in the Bighorn basin. Contours and shaded areas show the top of the Permo-Pennsylvanian Phosphoria and Minnelusa Formations and Tensleep oil fields, respectively, (WGA, 1989).

(4) Phosphoria Formation water chemistry

Figure 44 shows the water chemistry of Phosphoria Formation waters on a Piper diagram; most of those waters are classified Types A3 and B. The figure uses a different symbol for Type B waters having TDS (total dissolved solids) greater than 30,000 mg/l. These waters have X_{Cl} greater than 0.5 except for two water samples.

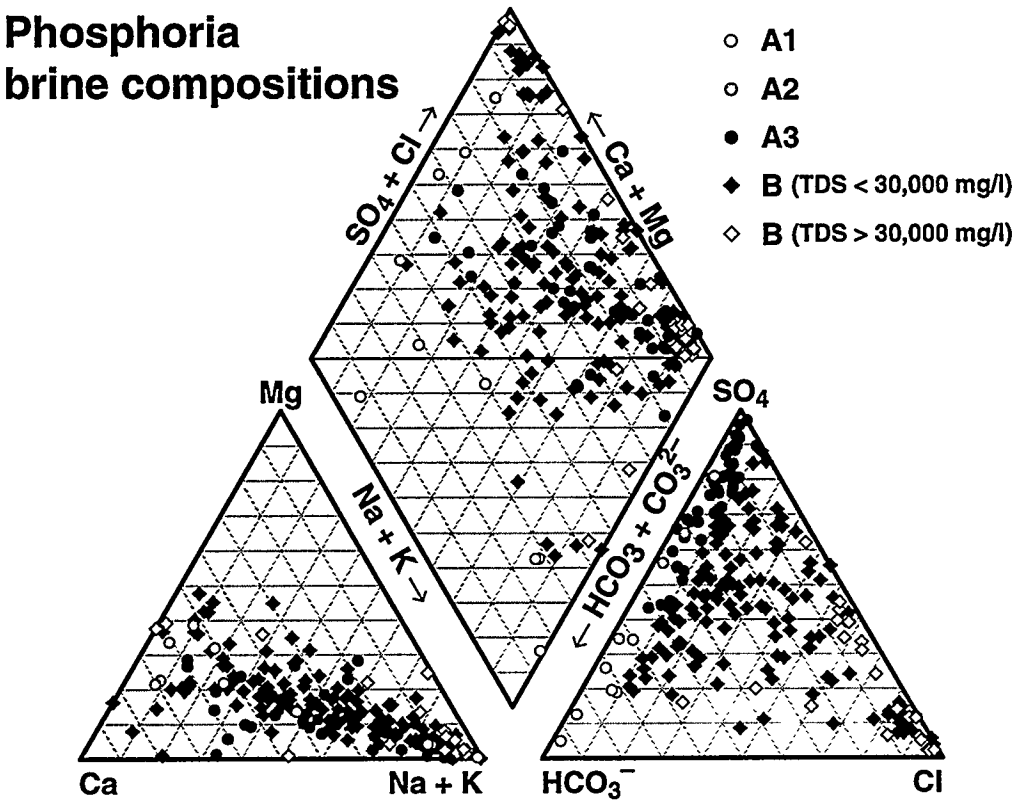

Figure 44. Chemical composition of Phosphoria Formation waters.

Figure 45 shows the relation between Na + K and SO_4 of the Type A3 and B Phosphoria Formation waters. High correlation can be seen for Type A3 waters and Type B waters having TDS smaller than 30,000 mg/l. Type B waters generally have slightly

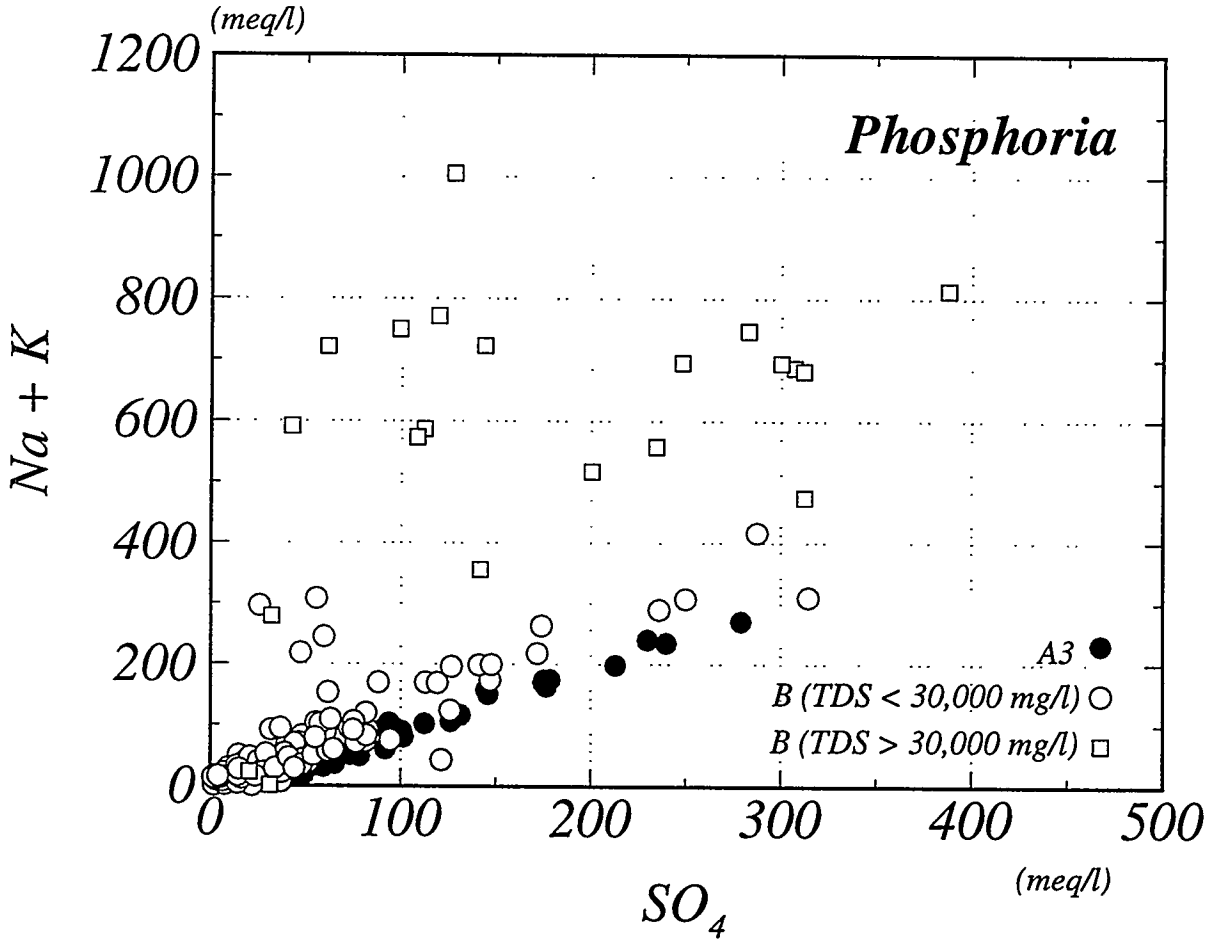

Figure 45. Na + K vs. SO_4 for Types A3 and B of Phosphoria Formation waters

higher Na + K concentration than Type A3 waters of similar SO_4 concentration, suggesting addition of Na(+K)Cl into Type A3 waters. Type B waters having TDS greater than 30,000 mg/l, however, have much higher alkali concentration than Type A3 and Type B with TDS < 30,000 mg/l. The fact that most of these waters are distributed near the Cottonwood and Black Mountain oil fields in the southeastern basin suggests either that mixing with high-NaCl water of other formations has occurred or that formation water around this area is stagnant (Dickey, 1969).

Figure 46 shows a distribution map of each type water of the Phosphoria Formation in the Bighorn Basin. The distribution trend of Type A3 and B waters is quite similar to that of the Tensleep Formation.

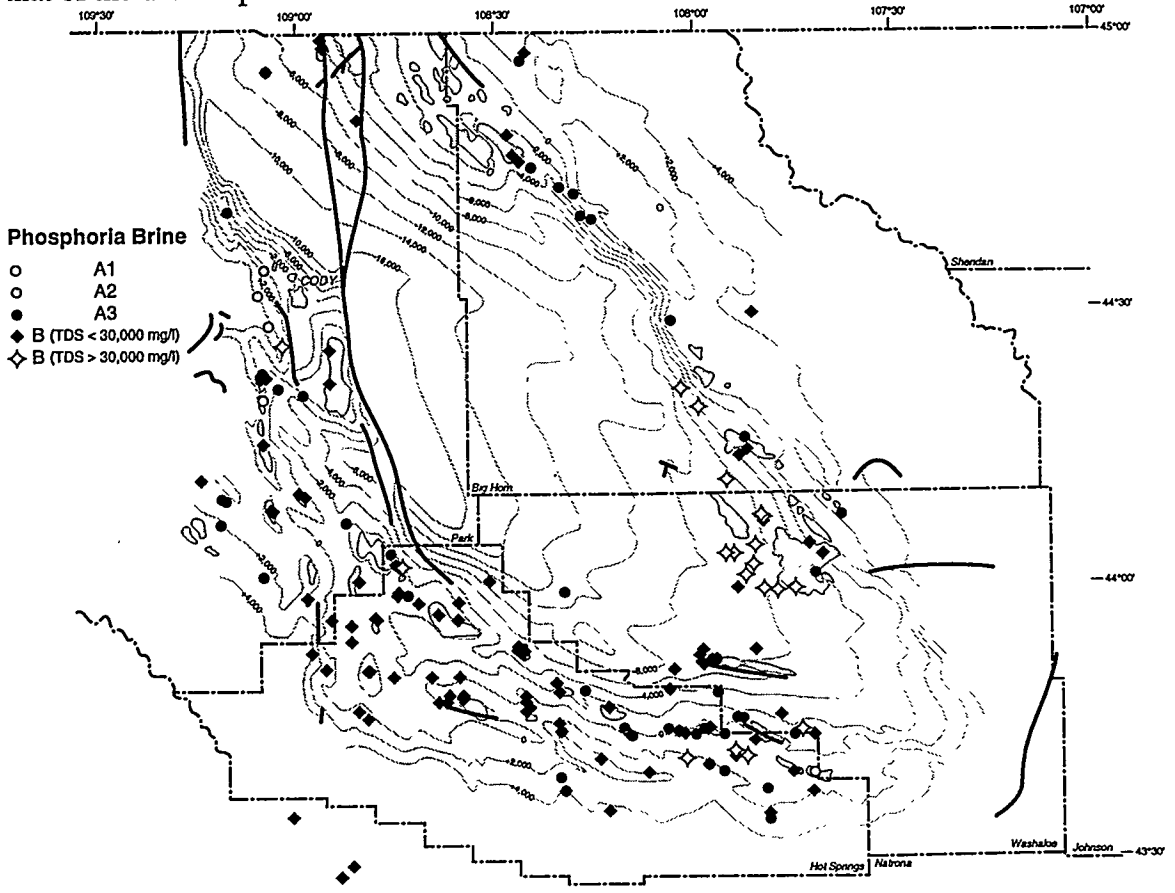

Figure 46. Distribution of Phosphoria Formation waters in the Bighorn basin. Contours and shaded areas show the top of the Permo-Pennsylvanian Phosphoria and Minnelusa Formations and Tensleep oil fields, respectively, (WGA, 1989).

Figure 47 shows histograms of total dissolved solids in Tensleep, Madison and Phosphoria Formation waters. Most Tensleep and Madison Formation waters have TDS ranging from 1,000 to 10,000 mg/l, whereas Madison Formation waters give a small peak around 300 to 400 mg/l — these are mostly Type A1 waters. Phosphoria Formation waters, however, have much higher TDS values than Tensleep and Madison Formation waters. This fact might reflect the lower permeability of the Phosphoria Formation (mainly shale) than that of the Tensleep and Madison Formations. The mean values of TDS in three formation waters are 4506 mg/l (Tensleep), 3504 mg/l (Madison), and 12,323 mg/l (Phosphoria).

COMPUTER SIMULATION OF ARAGONITE SCALE FORMATION DUE TO CO_2 FLOODING

Aspects of CO_2 -flooding

Figure 48 shows a schematic well-to-well CO_2 flooding and a pressure profile between the injection and production wells. In a CO_2 treatment, CO_2 gas is injected into an injection well and then brine is injected in order to push the gas phase toward the production wells; this process is then repeated periodically (e.g., Beeson and Orthloff, 1959; Holm and Josendal, 1974). Figure 48 shows sets of CO_2 gas and brine migrating in a reservoir from an injection well toward a production well. The initial pressure decreases rapidly near the injection well, and the middle area (between the injection and the production well) has about half the initial pressure. Near the production wells, the pressure drops rapidly (Thomas et al., 1992).

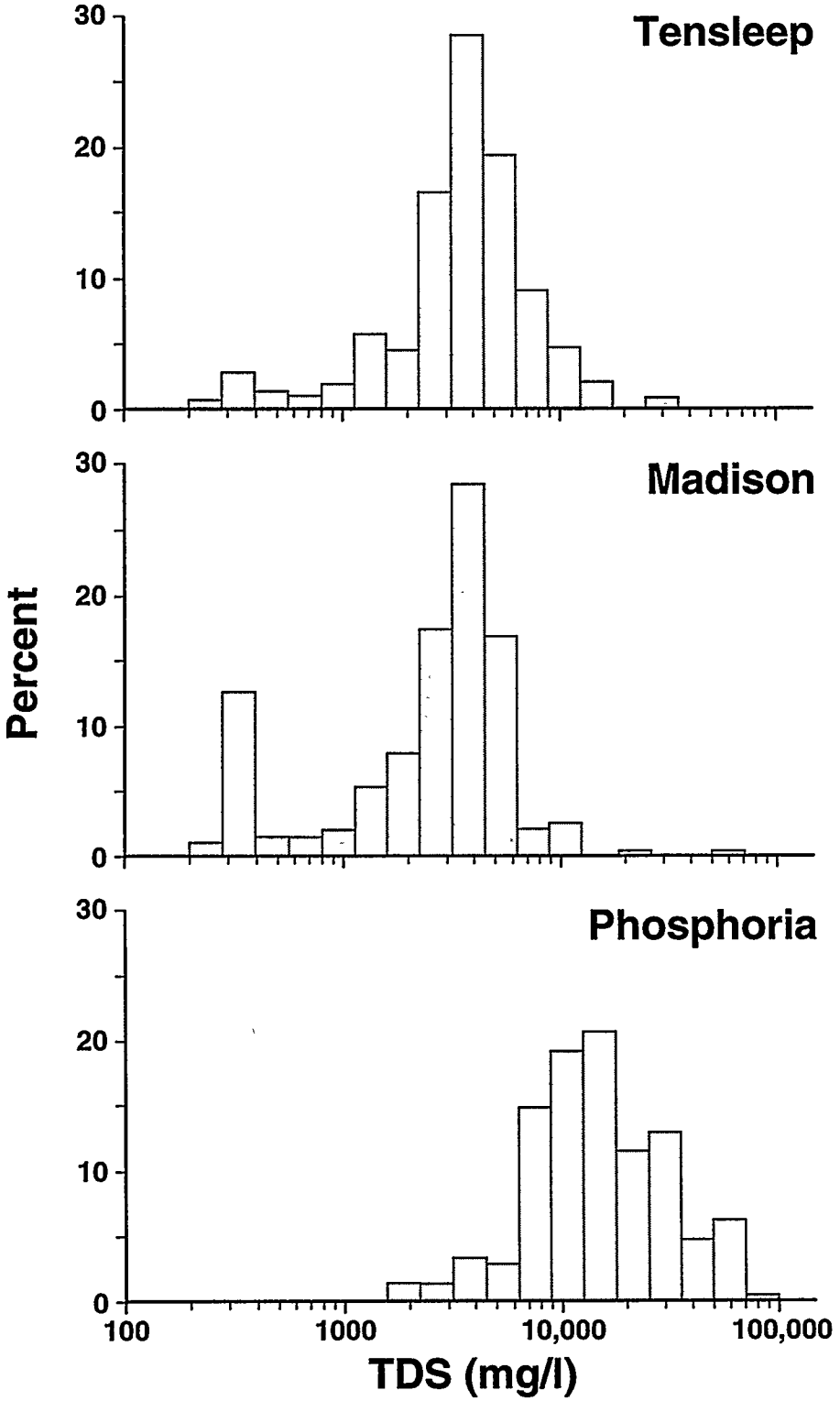

Figure 47. Histograms of total dissolved solids (TDS) for Tensleep, Madison, and Phosphoria.

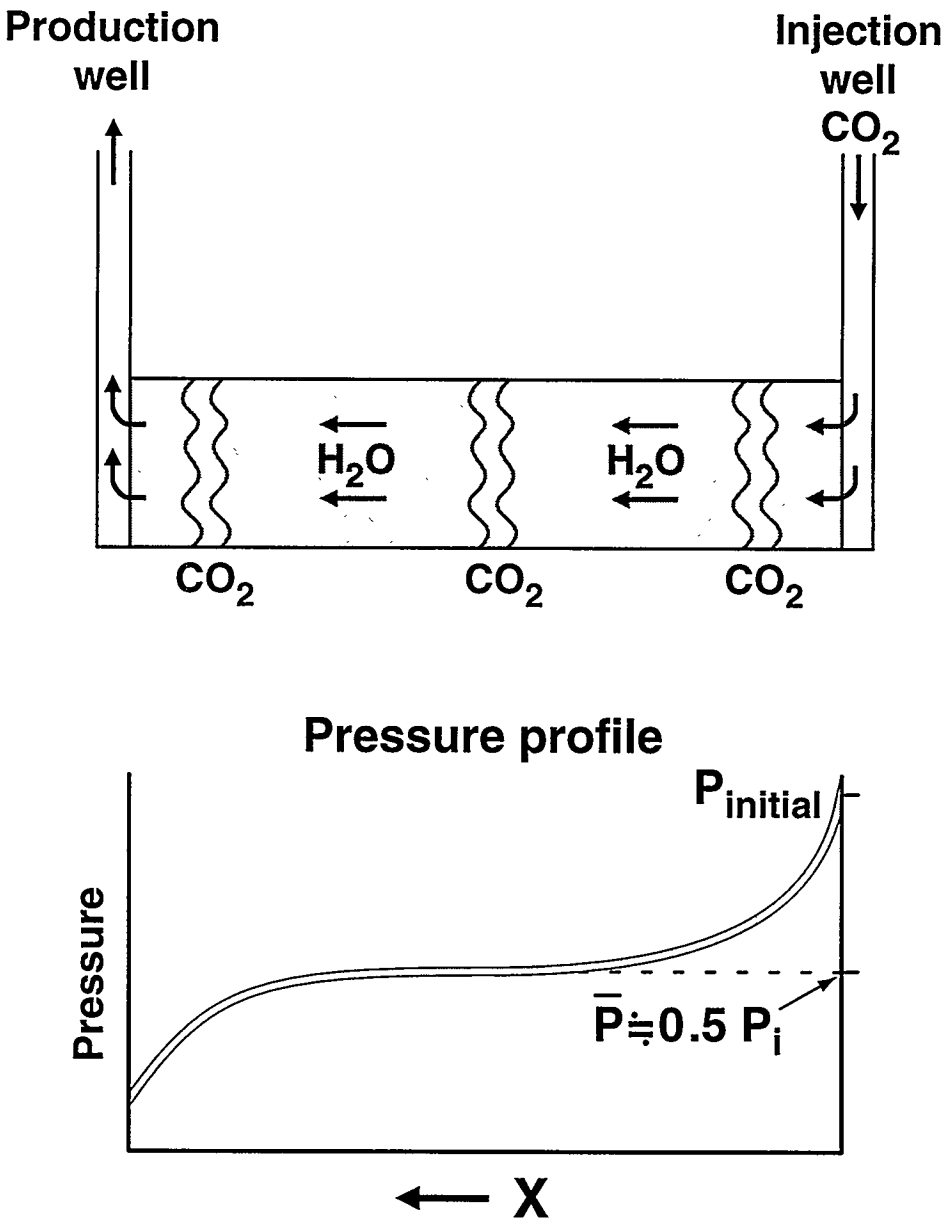

Figure 48. Schematic representations of well-to-well CO2 flooding and pressure profile between the injection and the production wells.

Method of simulation

Our simulation is a thermodynamic calculation of the saturation index of aragonite as a function of P_{CO2} and the extent of dissolution/precipitation of cement minerals in the formation. We adopted 80°C and 166 bars (= 2400 psi) as the T-P conditions for initial CO_2 injection — these are the conditions of an actual CO_2 flood at the Big Sand Draw oil field, Wind River Basin, Wyoming (Smith, 1993). First, a unit volume of formation water was pressurized by CO_2 up to 166 bars at 80°C. This procedure represents CO_2 and brine injection at an injection well. Then, P_{CO2} was decreased to 1 bar (the relation $P_{CO2} = P_{total}$ was held throughout the simulation), and we checked how the saturation index of aragonite (as well as those of dolomite and anhydrite) changed as a function of P_{CO2}. We also checked the effect of dolomite dissolution and the dissolution or precipitation of anhydrite on the saturation index of aragonite. The effects of dissolution and precipitation of these minerals were checked by adding or subtracting constituents of dolomite and anhydrite (Ca, Mg, CO_3, SO_4) in solution. Thus, our simulation represents the whole process of CO_2 flooding. Table 6 shows the chemical composition of Tensleep Formation waters used in the simulation, which are Type A1 and B waters, reported previously.

Table 6. Chemical composition of Tensleep Formation waters used in simulation, mg/l.

Constituent	A1	B
Na	14	2471
K	5	0
Ca	98	564
Mg	58	479
SO_4	47	4029
Cl	36	2926
HCO_3	512	525

The *SOLMINEQ.88* computer program (Kharaka et al., 1988) was used for the simulation. Table 7 summarizes the thermodynamic data for the speciation we adopted, as a function of pressure.

Table 7: Thermodynamic data (log K) for speciation at 80°C

		P (bars)	1	10	40	83	166
aqueous species:							
$CO_{2(g)} = CO_{2(aq)}$			- 1.84	- 1.84	- 1.84	- 1.84	- 1.84
$H_2CO_3 = H^+ + HCO_3^-$			- 6.34	- 6.33	- 6.32	- 6.30	- 6.26
$HCO_3^- = H^+ + CO_3^{2-}$			- 10.13	- 10.13	- 10.11	- 10.09	- 10.05
$CaHCO_3^+ = Ca^{2+} + HCO_3^-$			- 1.51	- 1.51	- 1.51	- 1.51	- 1.51
$CaCO_3 = Ca^{2+} + CO_3^{2-}$			- 3.93	- 3.93	- 3.93	- 3.93	- 3.93
$CaSO_4 = Ca^{2+} + SO_4^{2-}$			- 2.58	- 2.58	- 2.58	- 2.58	- 2.58
$MgHCO_3^+ = Mg^{2+} + HCO_3^-$			- 1.25	- 1.24	- 1.23	- 1.20	- 1.16
$MgCO_3 = Mg^{2+} + CO_3^{2-}$			- 3.31	- 3.30	- 3.30	- 3.28	- 3.26
$MgSO_4 = Mg^{2+} + SO_4^{2-}$			- 2.62	- 2.62	- 2.61	- 2.60	- 2.58
$H_2O = H^+ + OH^-$			- 12.60	- 12.60	- 12.59	- 12.57	- 12.54
minerals:							
$CaMg(CO_3)_2 = Ca^{2+} + Mg^{2+} + 2CO_3^{2-}$	*dolomite*		- 18.62	- 18.60	- 18.54	- 18.46	- 18.30
$CaCO_3 = Ca^{2+} + CO_3^{2-}$	*aragonite*		- 8.88	- 8.87	- 8.84	- 8.80	- 8.72
$CaSO_4 = Ca^{2+} + SO_4^{2-}$	*anhydrite*		- 5.02	- 5.01	- 4.98	- 4.95	- 4.88
$CaSO_4 2(H_2O) = Ca^{2+} + SO_4^{2-} + 2H_2O$	*gypsum*						- 4.77*
$SrSO_4 = Sr^{2+} + SO_4^{2-}$	*celestite*						- 6.62*
$BaSO_4 = Ba^{2+} + SO_4^{2-}$	*barite*						- 9.45*
$CaCO_3 = Ca^{2+} + CO_3^{2-}$	*calcite*						- 8.83*

These data were used for speciation of sample solutions of CO_2 core-flooding experiments. The saturation indices of minerals of interest are given by the following equations:

$$S.I.(aragonite) = log\left(\frac{a_{Ca^{2+}} a_{CO_3^{2-}}}{K_{sp}}\right) \quad (6)$$

$$S.I.(dolomite) = log\left(\frac{a_{Ca^{2+}} a_{Mg^{2+}} (a_{CO_3^{2-}})^2}{K_{sp}}\right) \quad (7)$$

$$S.I.(anhydrite) = log\left(\frac{a_{Ca^{2+}} a_{SO_4^{2-}}}{K_{sp}}\right) \quad (8)$$

where K_{sp} is the solubility product of the corresponding mineral, which is the activity product shown in the denominator of each equation at equilibrium. Therefore, the following important relations hold:

for supersaturation	S.I. > 0
at equilibrium	S.I. = 0
for undersaturation	S.I. < 0

A solution has potential for aragonite scale formation when it is supersaturated with respect to the mineral (i.e., S.I. > 0).

Results and Discussion

Figure 49 shows the relation between the saturation index of dolomite and P_{CO2} for Type B water. At P_{CO2} = 166 bars, the solution is highly undersaturated with respect to dolomite (S.I. = -3.88) as the pH of the solution declines due to dissolution of CO_2 gas. The saturation index of dolomite becomes greater as P_{CO2} decreases, and the solution becomes saturated with respect to dolomite at P_{CO2} = 2 bars, if dolomite dissolution does not take place. The saturation index of dolomite is a nearly linear function of log [P_{CO2}].

Because of high undersaturation with respect to dolomite at high P_{CO2}, dolomite should dissolve into solution in a real CO_2 flood within a Tensleep reservoir. The figure shows the saturation index of dolomite when 2.5, 5.0, and 10.0 mmol/kg of dolomite

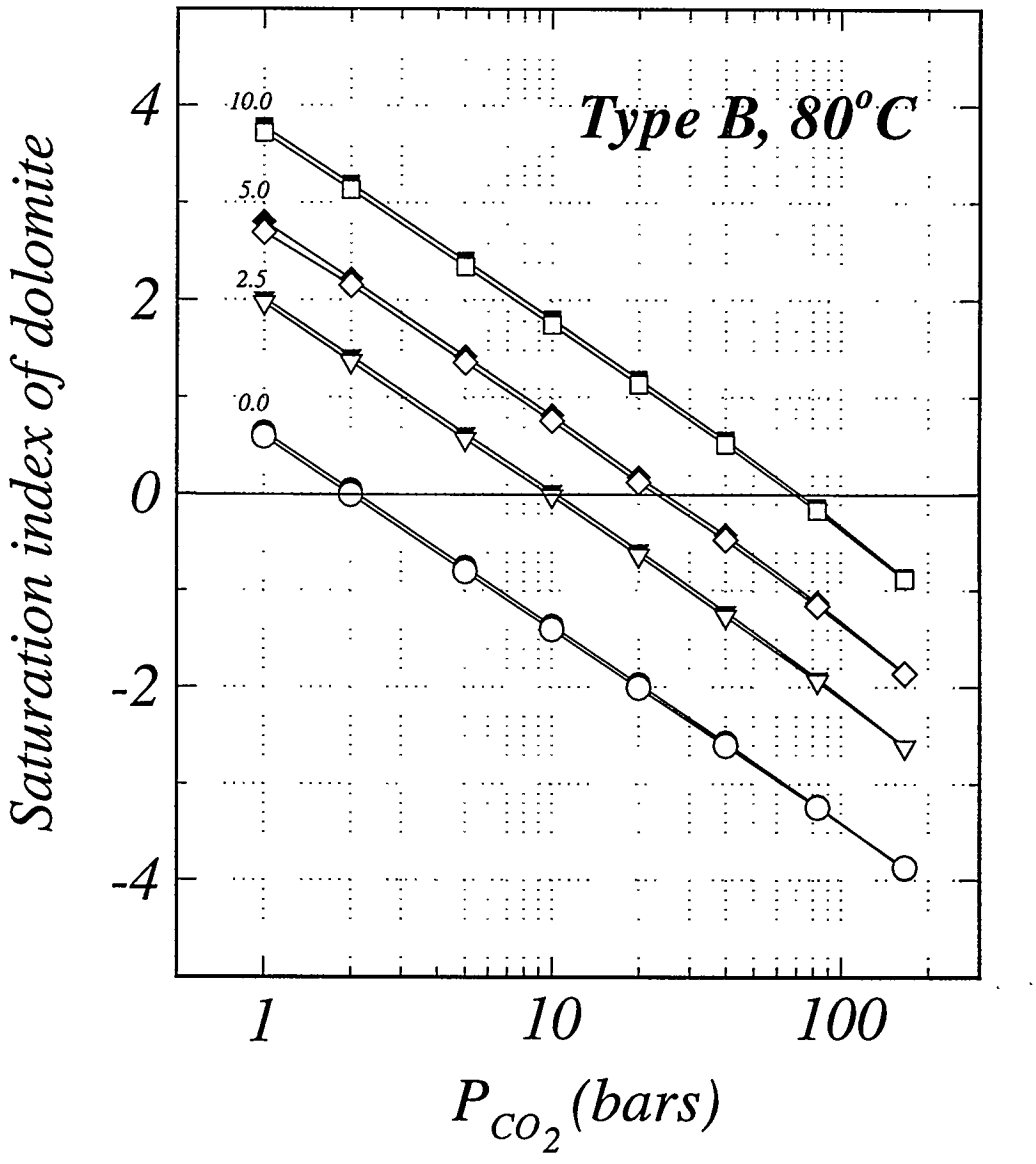

Figure 49. Saturation index of dolomite as a function of P_{CO2} obtained by simulation for a Type B Tensleep Formation water. Numbers in the figure show the amount of dolomite dissolved (mmole/kg). Open and filled sympols show results without and with adjusting solution compositin to achieve anhydrite saturation, respectively

were dissolved in solution. The figure shows clearly that the saturation index of dolomite increased as the amount of dissolved dolomite increased. The saturation index of dolomite at P_{CO2} = 166 bars, for example, changed from -3.88 to -2.61 to -1.85 to -0.87 as 2.5, 5.0, and 10.0 mmol/kg dolomite were dissolved. The changes in the saturation index of dolomite with decreasing P_{CO2} after dolomite dissolution, however, were quite similar to the changes in the solution with no dissolved dolomite; i.e., the graphs of the functions in Figure 49 are nearly parallel.

Figure 49 also shows the results of simulations in which anhydrite precipitation was caused until the solution reached saturation with respect to anhydrite. As the solution was supersaturated with respect to anhydrite in the calculation above, except at P_{CO2} = 166 without dolomite dissolution, the effect of anhydrite precipitation was checked. The figure shows that the effect of anhydrite precipitation on the saturation index of dolomite was small.

Figure 50 shows the saturation index of aragonite as a function of P_{CO2} for cases of dolomite dissolution of 0.0, 2.5, 5.0, and 10.0 mmol/kg with and without anhydrite precipitation. The figure shows that the saturation index of aragonite is a linear function of log [P_{CO2}] and also greatly depends on the amount of dolomite dissolved; this is due to the addition of both Ca and alkalinity (i.e., CO_3^{2-} or pH increase) to the solution. The effect of anhydrite precipitation on aragonite saturation index is still small, but is slightly greater that effect on the dolomite saturation index (Figure 49). A solution has potential for aragonite scale formation when the saturation index of aragonite is positive, and this result suggests that the dissolution of dolomite during CO_2 gas and brine mixture migration is an important factor controlling the potential of aragonite scale formation.

This result is shown in another way in Figure 51. The figure shows the relation between the amount of dolomite dissolved into solution and the P_{CO2} at which the solution is saturated with respect to aragonite. The figure shows that the P_{CO2} of aragonite saturation increases quadratically with respect to the amount of dolomite dissolved,

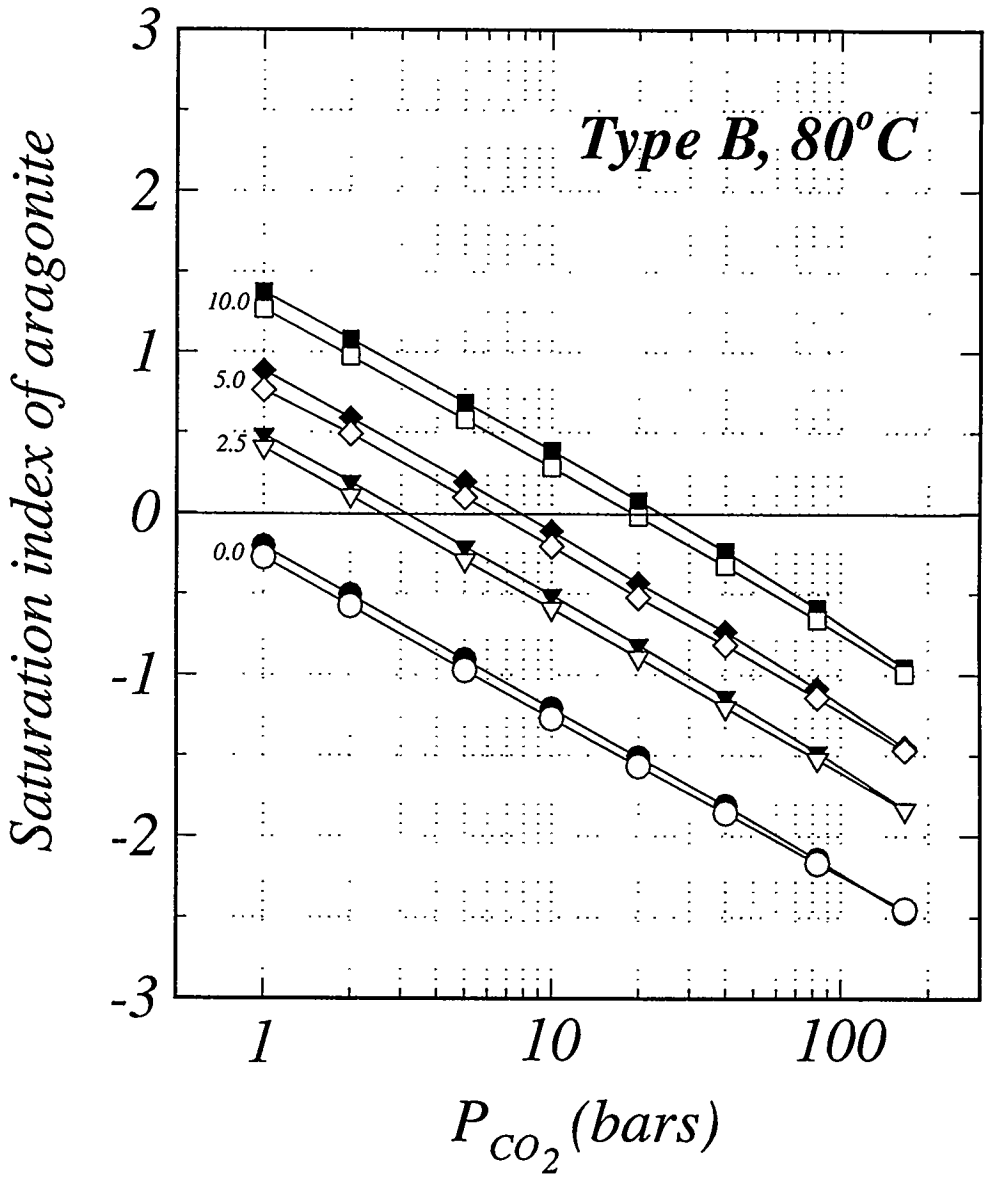

Figure 50. Saturation index of aragonite as a function of P_{CO2} obtained by simulation for a Type B Tensleep Formation water. Symbols used are same as those in Figure 49.

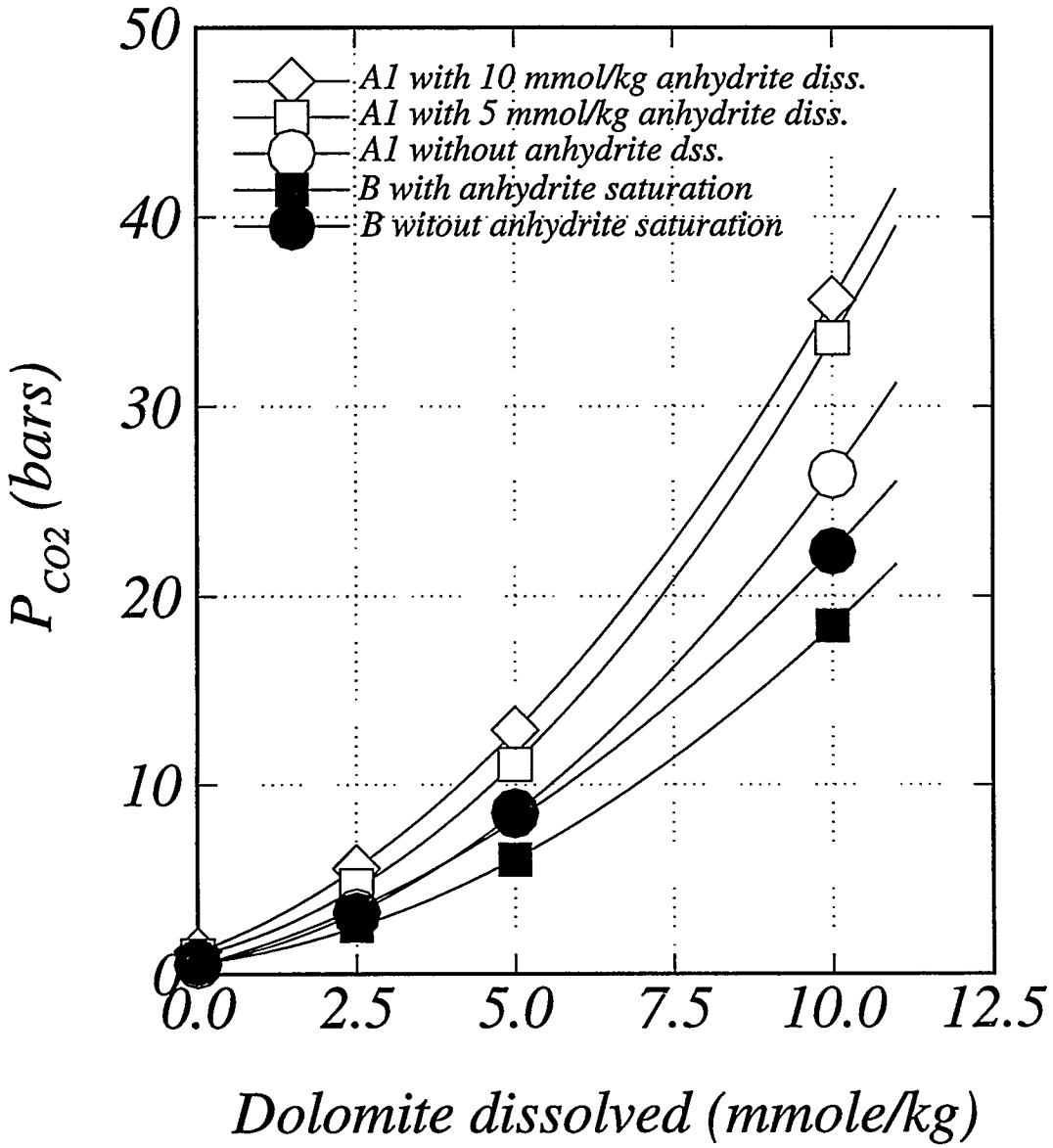

Figure 51. Relation between P_{CO2} at which solution gets saturatiton with respect to aragonite and the amount of dolomite dissolved.

suggesting that dolomite dissolution raises the potential of aragonite scale formation considerably.

Figure 51 also shows the results of simulation of a Type A1 brine. When only dolomite dissolved into the solution, the P_{CO2} at which the solution is saturated with respect to aragonite is close to that of Type B water, but is slightly higher. In this case, however, the solution was highly undersaturated with respect to anhydrite, even after the dolomite was dissolved, suggesting anhydrite should dissolve into an A1 solution as well as dolomite. We calculated the cases in which 5.0 and 10.0 mmol/kg anhydrite were dissolved into solution. Unlike the anhydrite precipitating in Type B water, the result of the dissolution of anhydrite in Type A1 brines were increased potential for aragonite scale formation, through addition of Ca into solution. The effect was, however, not so great as that of dolomite dissolution.

The simulation showed that solution made acidic by the dissolution of CO_2 gas should cause dolomite dissolution in the Tensleep Formation reservoirs, and that this mineral dissolution considerably raises the potential for aragonite scale formation. Aragonite is a common scale mineral in the field due to real CO_2 treatment. This simulation shows that aragonite should precipitate when a solution is supersaturated with respect to the mineral, slightly reducing the potential of aragonite scale formation. However, the simulation was based only on thermodynamic considerations, and did not take into account the rate of dolomite dissolution.

CO_2 CORE-FLOODING EXPERIMENT

During the second contract year, two CO_2 core-flooding experiments (*Runs 2 and 3*) were carried out at the Petroleum Technology Center, Marathon Oil Company, Littleton, Colorado. Experimental apparatus and techniques were quite the same as those adopted in an earlier experiment (*Run 1*), which was run during the first contract year (Dunn, 1994).

Experimental

Run 2 was a blank test for contamination from the apparatus, run without cores using the same artificial Tensleep Formation water (Type A2) as that used in Run 1. In Run 3, three subsurface cores from Oregon Basin oil field and an artificial Type B water were used as starting materials. The chemical composition of these nutrient solutions are shown in Table 8.

Table 8: Chemical composition of nutrient solutions used in CO_2 core-flooding experiment, mmol/l.

Constituent	Run 1, 2	Run 3
Na	8.48	86.3
K	0.0	0.02
Ca	11.5	15.8
Mg	5.14	17.5
SO_4	20.5	30.6
Cl	0.0	93.3

After equilibrium was attained with CO_2 gas in solution at 80°C and 166 bars, these solutions were flowed into the core assemblage at a flow rate of 7.5 ml/h, and then sampled at constant time intervals. The volume of CO_2 degassed out of the samples was measured. pH and alkalinity (in Run 3) were measured with a pH electrode and titration with HCl on-site, and the samples were then acidified to keep all ions in solution for later chemical analyses. Cations and silica concentration were determined by ICP, and Cl and SO_4 were measured with ion chromatography (IC). The porosity and air permeability of the cores were measured before and after the runs. Speciation of the sample solutions was carried out using *SOLMINEQ.88* (Kharaka et al., 1988); the thermodynamic data used in speciation are shown in Table 6.

Results and Discussion

The results of Run 1 reported in the First Annual Report were recalculated to take Fe released from the apparatus into account, and are reported here with those of Run 3.

Figure 52 shows the concentration change of Ca, Mg, and SO_4 in the effluent solutions with time during Runs 1 and 3. The concentrations of Ca in the first samples from Runs 1 and 3 were 30% and 18% larger than those of the nutrient solutions, respectively. Those concentrations decreased with time, and returned to nearly those of the nutrient solutions. The concentration of Mg increased with time, although the first sample from Run 1 had 28% less than the nutrient solution. SO_4 concentration in both runs monotonously decreased with time, from 20.5 to 16.4 mmol/l in Run 1, from 32.5 to 28.9 (second last sample) mmol/l in Run 3, although the concentration of SO_4 of the first sample from Run 1 dropped abruptly to 3.69 mmol/l, like Mg.

Figure 53 shows change of solution pH and concentration change of SiO_2 and K in the effluent solutions with time during Runs 1 and 3. The solution pH of the first samples jumped from the initial value of 3.10 for the nutrient solution to 4.54 and 4.15 in Runs 1 and 3, respectively. The values of pH of the third sample of Run 1 and second samples of Run 3 dropped down to 4.00 and 4.15, respectively, and then gradually increased with time. The silica and K concentrations jumped in the first samples of both runs and then decreased monotonously with time, although more silica dissolved in Run 3 (0.86 and 2.56 mmol/l in Runs 1 and 3, respectively).

The immediate, sharp increase in concentration of Ca and silica in the first samples from both runs suggests a hydrolysis reaction in the silica phase (quartz and amorphous silica) and plagioclase by hydrogen ions. Similar reactions have been observed in experiments on volcanic rock-seawater interaction at high temperatures (e.g., Bischoff and Dickson, 1981; Mottle and Holland, 1978; Hajash and Chandler, 1981; Seyfried and Bischoff, 1981; Shiraki et al., 1987). Bischoff and Seyfried (1978) showed that Mg and SO_4 ions precipitate to form $MgO \cdot n\ MgSO_4 \cdot nH_2O$ when sea water is heated to high

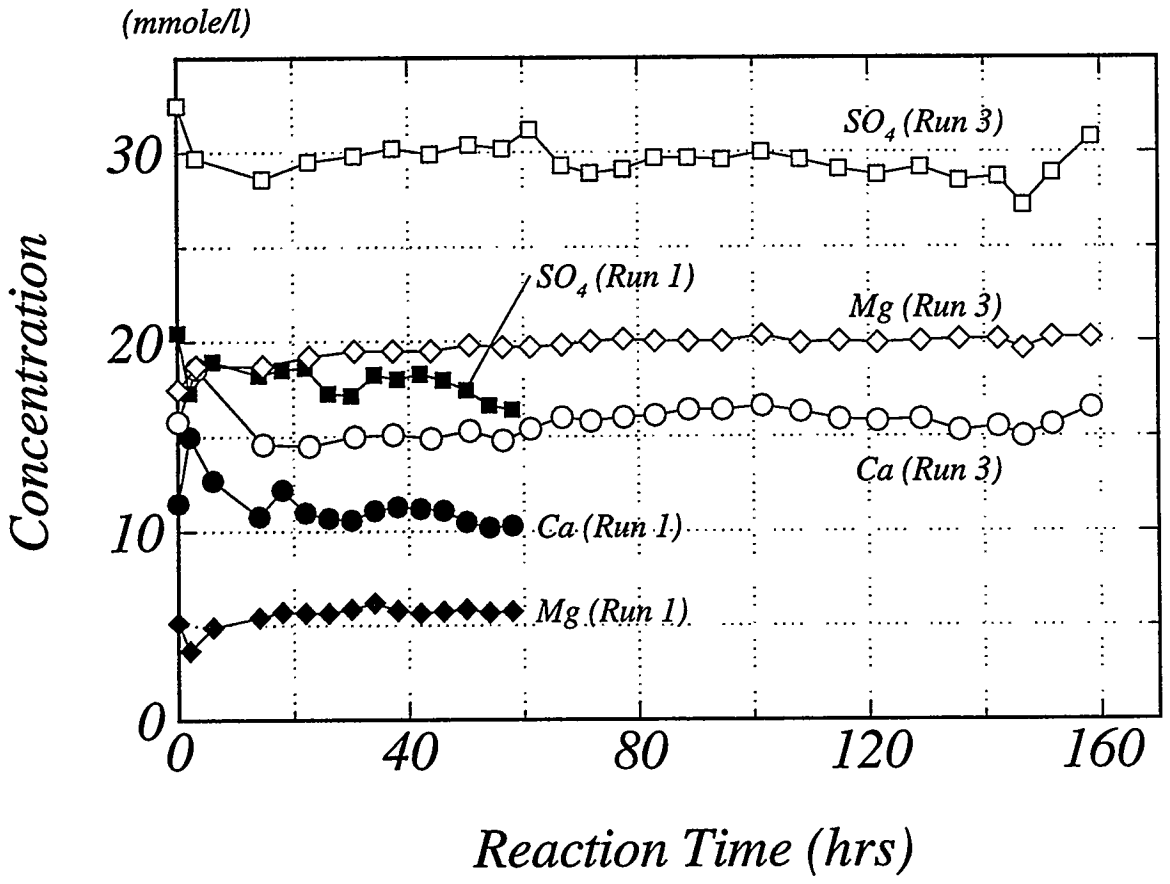

Figure 52. Concentrations of Ca, Mg, and SO_4 vs. reaction time of CO_2 core flooding experiments

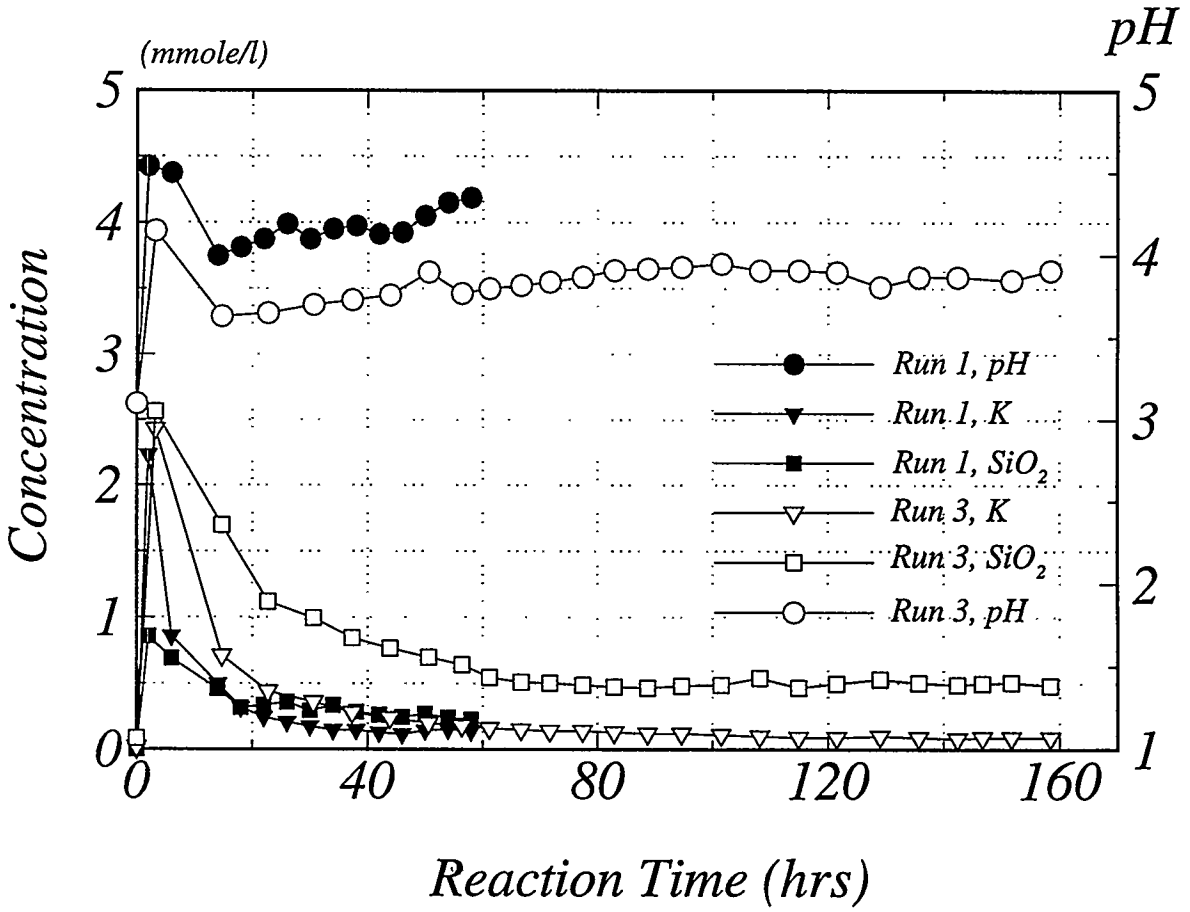

Figure 53. Solution pH and concentrations of SiO_2 and K vs. reaction time of CO_2 core flooding experiments

temperature. The decrease in Mg and SO_4 in the first sample from Run 1 (Figure 52) may be due to the same reaction. The nutrient solution was in contact with the rock phase when the system attained experimental temperature in Run 3, whereas the solution was introduced into cores after the system reached experimental temperature in Run 1. Dolomite dissolution (discussed in detail below) probably countered this decrease in Mg in the first sample from Run 3 due to longer reaction time. A higher silica content in the first sample in Run 3 was probably caused by same reason.

Figure 54 shows the calculated saturation indices of dolomite, anhydrite, and quartz in the effluent solutions. In both Runs 1 and 3, the solution was saturated with respect to anhydrite throughout the runs. The first samples had the highest saturation indices of quartz (0.28 and 0.75) and the values decreased steadily with time. The first solution from Run 3 was nearly saturated with respect to amorphous silica. Quartz overgrowth and quartz veins, including microcrystalline quartz and quartz showing wavy extinction, were observed in core sample under the microscope. The high content of silica in the early samples was probably due to dissolution of grains having high surface energy, as well as feldspar dissolution.

On the other hand, the solutions were highly undersaturated with respect to dolomite throughout the runs. The first two samples from Run 1 and the first sample from Run 3 had relatively high saturation indices compared with other sample solutions. This may be because the higher pH of the these solutions caused a hydrolysis reaction of the silicate phase by hydrogen ions. After a quick drop, the saturation index of dolomite gradually increased with time. The saturation indices of dolomite at the last stages of the runs were -2.58 (average of last five samples) in Run 1 and -3.54 (average of last eight samples) in Run 3, respectively. The saturation index of dolomite in Run 1 is about one index unit greater than that in Run 3, whereas the patterns of change with time are quite similar. This may be due to the fact that the cores used in Run 1 contained more dolomite cement that those used in Run 3.

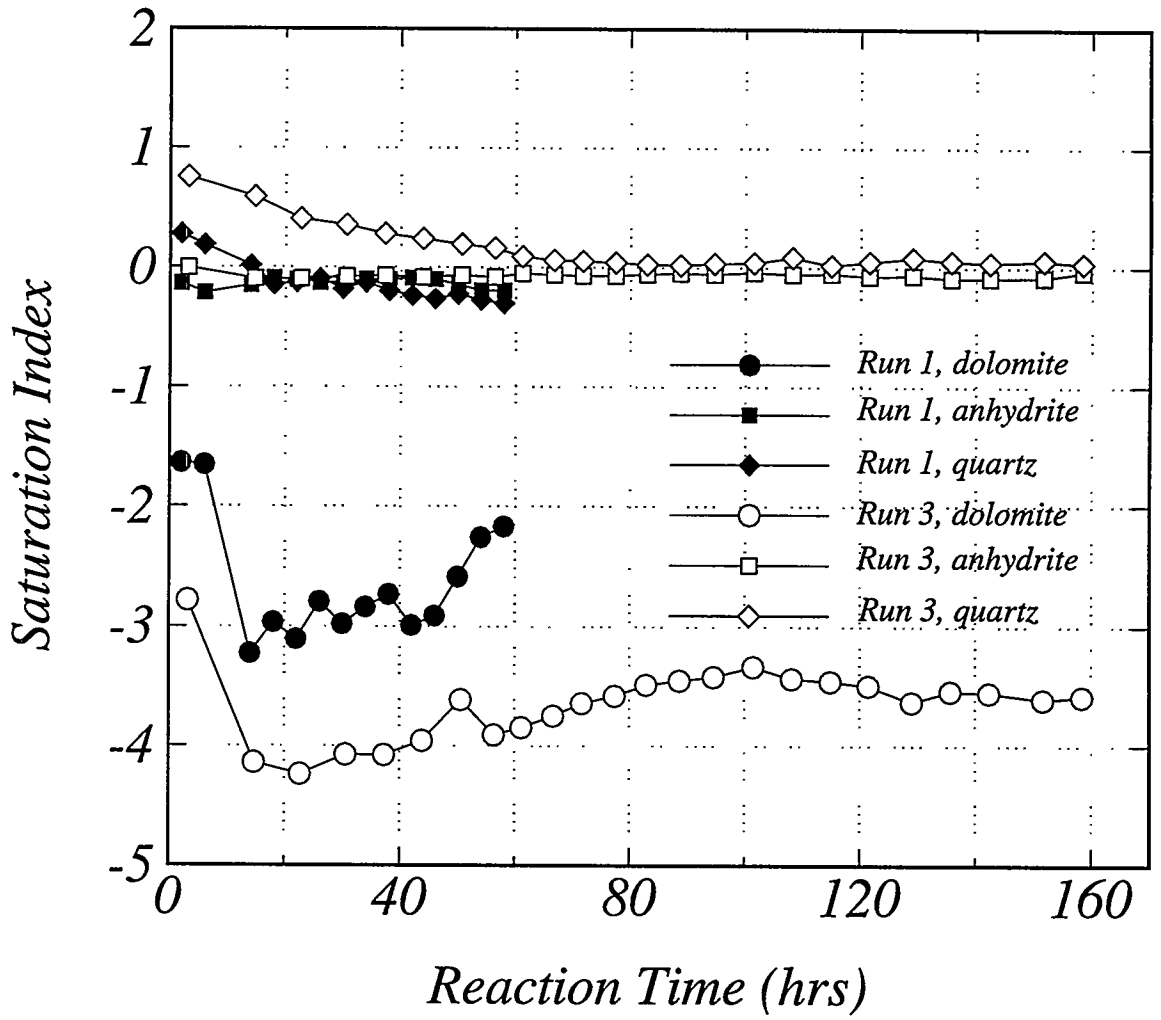

Figure 54. Saturation indices of dolomite, anhydrite, and quartz vs. reaction time of CO_2 core flooding experiments

Figure 55 shows the change of the saturation indices of celestite and barite with time during Runs 1 and 3. The solutions of both runs were saturated with respect to barite throughout the runs, whereas they were undersaturated with respect to celestite.

The observations above suggest that dolomite dissolved in solutions made acidic by dissolution of CO_2 gas, which is simply expressed by Equation (1), following rapid hydrolysis reactions of silica and silicate phases. This reaction should cause increase in Ca concentration as well as Mg concentration. However, the Ca concentration was almost constant through both runs, outside of an abrupt increase at the earliest stage due to the hydrolysis reactions. In light of the decrease in SO_4 concentration with time, we can conclude that anhydrite precipitation probably took place and took up some of Ca released from the dolomite phase. This is the reverse reaction of Equation (2). Under this argument, the case of dolomite dissolution with anhydrite precipitation in our simulation is more plausible.

The stoichiometry in Equation (1) and the reverse reaction of Equation (2) suggest that the increase in Mg concentration (ΔMg) should have been equal to the decrease in SO_4 concentration ($\Delta SO4$), if the steady-state concentrations are controlled by these two reactions, because the nutrient solution was saturated with respect to anhydrite at run temperature. This was, however, not the case. Results from Run 3 showed that more SO_4 was consumed than Mg supplied ($\Delta SO4$ = - *3.6 mmol/l*, ΔMg = *2.5 mmol/l*). This suggests that another sulfate mineral(s) might have precipitated, as well as anhydrite. If this is true, barite is the most plausible mineral, because solutions were saturated with respect to barite throughout both runs (Figure 55).

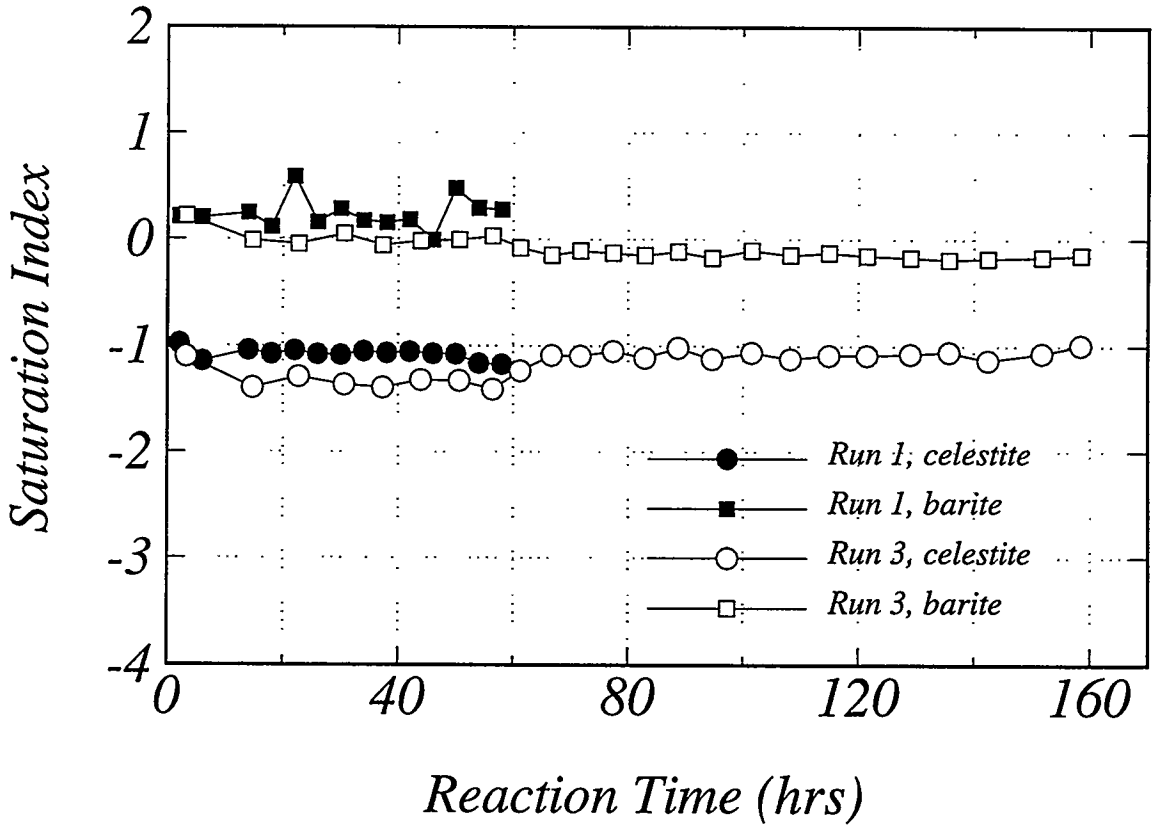

Figure 55. Saturation indices of celestite and barite vs. reaction time of CO_2 core flooding experiments

Figures 56 and 57 show the changes in the saturation indices of dolomite and aragonite in both runs, as well as the results of simulations for nutrient solutions of Run 3 similar to those of Tensleep Formation waters reported in the previous section. As some amount of carbonate species diffused through the Teflon, aluminum foil (only in Run 1), and rubber tubing that wrapped the cores during solution flow initial, P_{CO2} - calculated from $a_{H_2CO_3}$ using the relation $P_{CO_2} = a_{H_2CO_3}/k_H$, where k_H is Henry's law constant, was lowered from 166 bars to 86.7 and 68.7 bars in Runs 1 and 3, respectively. Figures 56 and 57 show clearly that the saturation index of aragonite was raised due to dissolution of dolomite; this fact, in turn, suggests a measure of the potential for aragonite scale formation. It is necessary to understand how quickly a solution will reach saturation with respect to aragonite. To predict scale formation, however, depends on kinetics of dolomite dissolution under local T-P conditions.

Table 9 summarizes changes in porosity and air permeability of the cores during the experimental runs. No change in porosity was observed. However, the permeability of cores used in Run 3 decreased considerably (79 to 84%), whereas the permeability of cores used in Run 1 increased (103 to 136%). The permeability of rocks depends both on porosity and on the geometry of pores. As the porosity of the cores used in these experiments did not change through runs, the observed changes in permeability might suggest change in the geometry of pores, due to water-rock interaction during the runs.

Table 9: Porosity and permeability before and after runs of cores used in CO_2 core flooding experiment

Run	Core	Porosity (%)			Air permeability (md)		
		Before	After	A/B*	Before	After	A/B*
Run 1	core 1	9.4	9.3	0.99	56.92	71.95	1.26
	core 2	11.7	11.6	0.99	97.42	99.92	1.03
	core 3	8.3	8.3	1.00	53.53	72.55	1.36
Run 3	core 1	14.6	14.6	1.00	61.84	48.56	0.79
	core 2	14.2	14.3	1.01	64.59	53.68	0.83
	core 3	14.8	14.3	1.01	76.04	64.20	0.84

*A/B = ratio of either porosity or air permeability after run to that before run

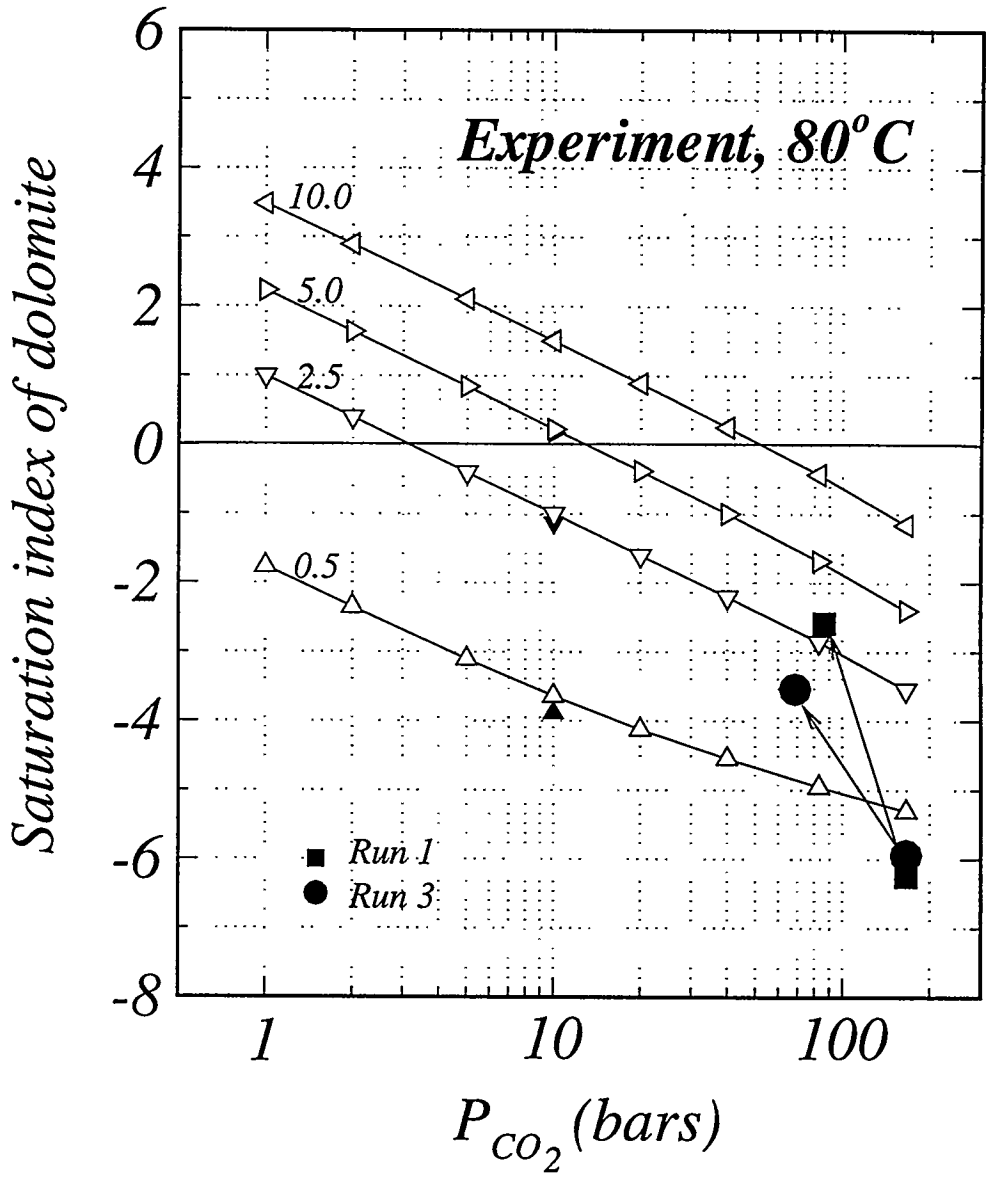

Figure 56. Change of saturation index of dolomite through CO_2 core flooding experiments. Results of simulation for the nutrient solutions are also shown in same manner as Figure 49.

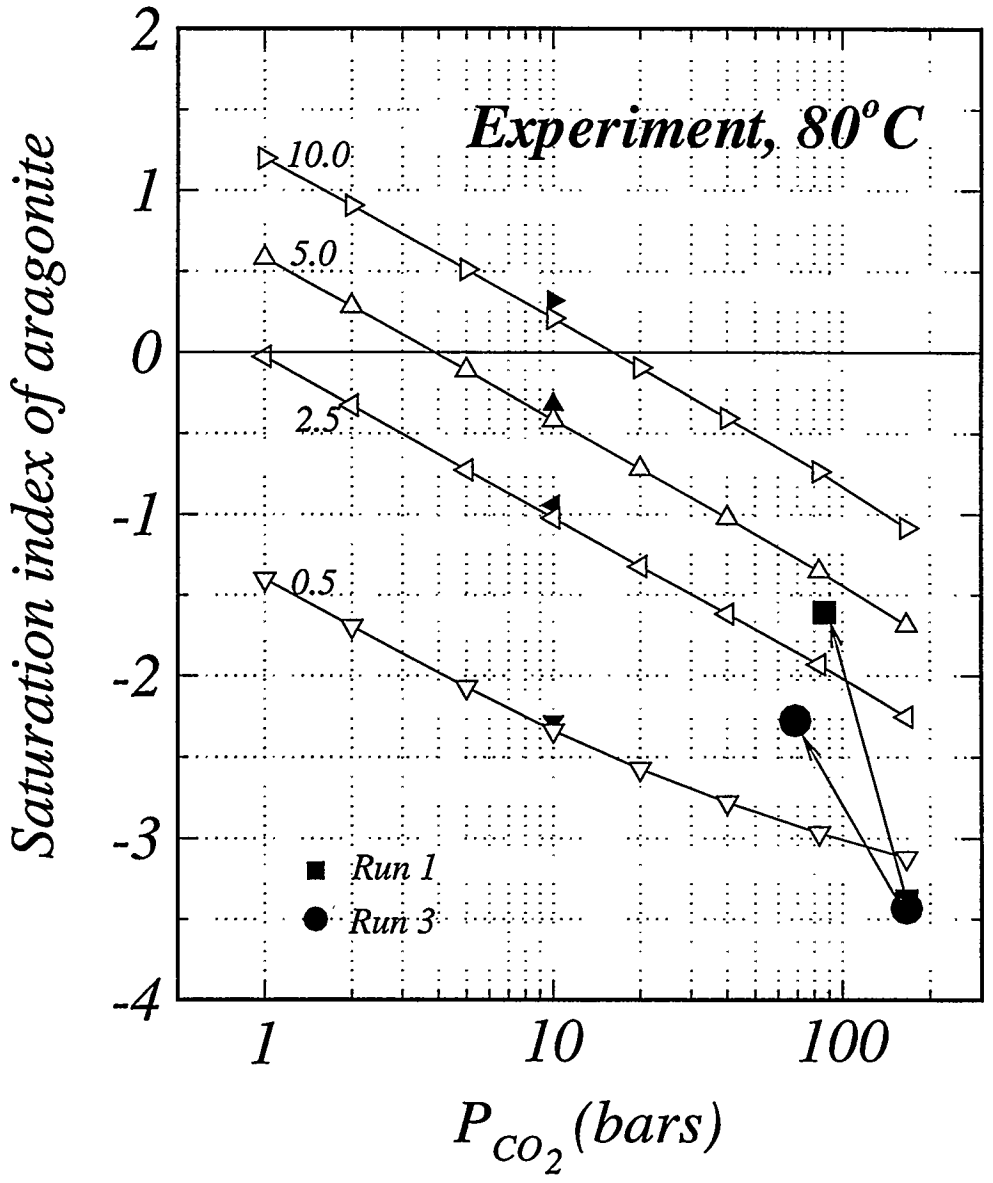

Figure 57. Change of saturation index of aragonite through CO_2 core flooding experiments. Results of simulation for the nutrient solutions are also shown in same manner as Figure 49.

TASK 4.0 - PROJECT MANAGEMENT AND TECHNICAL TRANSFER

Thomas L. Dunn - Task Leader

OBJECTIVES

This task incorporates efforts to achieve a high level of success in this interdisciplinary project. This administrative task provides for effective coordination and integration of the project's research tasks. The program manager is responsible for ensuring that the task workers meet on a frequent and regular basis to exchange information and discuss results. The program manager is responsible for the coordination and timely reporting of results to its Industry Advisor/Mentors, the Department of Energy, and the scientific and engineering communities.

The task was fully staffed during the second year. Professor William Iverson, Task 2.0 leader left the University of Wyoming at the end of August, 1995. Negotiations are underway to retain him on a consulting basis for the remainder of the contract. Mr. Iraj Adjari graduated, having completed his M.S degree in Petroleum and Chemical Engineering. The Industrial Advisor/Mentors have been consulted through correspondence.

One paper describing the results of the relative permeability measurements has been accepted for presentation at the SPE meeting in Tulsa, OK, April 21, 1996. We will submit several papers to the Wyoming Geological Association Field Conference for 1996 which focuses on the Bighorn Basin, Wyoming. This effort should include a field trip through the Tensleep combining our laboratory work with the regional sedimentological observations.

On September 6, 1995 Mary Crabaugh led a field trip to outcrops of the Tensleep at Alkali Flats and Medicine Lodge, along the western margin of the Bighorn Mountains (Figure 5). The field trip brought together sixteen Marathon Oil Company geologists, engineers and geophysicists to discuss the utility of our process-oriented approach to

reservoir characterization. The trip included outcrop examples of the geometry and scale of heterogeneity, the extent of lateral variability within individual sets of cross-strata, and the vertical discontinuity of the interbedded interdune accumulations. The discussion focused on the varying success of Marathon's horizontal well program. It was clear from the discussion that a characterization similar to our approach was key to a successful infill program.

REFERENCES

Agatston, R.S., 1952, Tensleep Formation of the Bighorn Basin: Wyoming Geological Association Seventh Annual Field Conference Guidebook, p. 44-48.

Agatston, R.S., 1954, Pennsylvanian and Lower Permian of northern and eastern Wyoming: American Association of Petroleum Geologists Bulletin, v. 38, p. 508-583.

Ajdari, A., 1995, Anisotropy of Relative Permeability Within the Tensleep Sandstone: M.S. thesis, University of Wyoming, 106 p.

Andrews, S., and Higgins L.S., 1984, Influence of depositional facies on hydrocarbon production in the Tensleep sandstone, Big Horn Basin, Wyoming; A working hypothesis: Wyoming Geological Association Thirty-fifth Annual Field Conference Guidebook, p. 183-197.

Back, W. and Hanshaw, B.B., 1970, Comparison of chemical hydrogeology of the carbonate peninsulas of Florida and Yucatan: Journal of Hydrology, v. 10, p. 330-368.

Back, W., Hanshaw, B.B., Plummer, L.N., Rahn, P.H., Rightmire, C.T., and Rubin, M., 1983, Process and rate of dedolomitization: Mass transfer and 14C dating in a regional carbonate aquifers: Geological Society of America Bulletin, v. 94, p. 1415-1429.

Beeson, D.M., and Orthloff, G.D., 1959, A laboratory investigation of the water-driven carbon dioxide process for oil recovery: American Institute of Mining Engineers Transactions, v. 216, p. 388.

Bischoff, D.M., and Seyfried, W.E., 1978, Hydrothermal chemistry of seawater from 25°C to 350°C: American Journal of Science, v. 278, p. 838-860.

Bischoff, J.L. and Dickson, F.W., 1975, Seawater-basalt interactions at 200°C and 500 bars: Implication for origin of sea-floor heavy metal deposits and regulation of seawater chemistry: Earth and Planetary Science Letters, v. 25, p. 385-397.

Brainerd, A.E., and Keyte I.A., 1927, New faunal evidence from Tensleep Formation: Journal of Paleontology, v.1, p. 173-174.

Branson, C.C., 1939, Pennsylvanian formations of central Wyoming: Geological Society of America Bulletin, v. 50, p. 1199-1226.

Breed, C.S., Fryberger, S.C., Andrews, S., McCauley, C., Lennartz, F., Gebel, D., and Horstman, K., 1979, Regional studies of sand seas using Landsat (ERTS) imagery. *in* McKee, E.D., ed., A Study of Global Sand Seas: Geological Survey Professional Paper 1052, p. 305-397.

Brookfield, M.E., 1977, The origin of bounding surfaces in ancient eolian sandstones: Sedimentology, v. 24, p. 303-332.

Buckley, S.E., and Leverett, M.C., 1942, Mechanism of fluid displacement in sands: American Institute of Mining Engineers Transactions, v. 146, p. 107-116.

Busby, J.F., Plummer, L.N., Lee, R.W., and Hanshaw, B.B., 1990, Geochemical evolution of water in the Madison aquifer in part of Montana, South Dakota, and Wyoming: U.S. Geological Survey Professional Paper, v. 1273-F, p. 1-89.

Butler, G.P., Harris, P.M., and Kendall, C.G.St.C., 1982, Recent evaporites from the Abu Dhabi coastal flats: Depostional and diagenetic spectra of evaporites, A core workshop: Society of Economic Paleontologists and Mineralogists Core Workshop #3, p. 33-64.

Chevotarev, I.I., 1955, Metamorphism of natural waters in the crust of weathering: Geochimica et Cosmochimica Acta, v. 8, p. 22-48.

Crabaugh, M., 1994, Character and Controls of the Depositional Architecture in a Wet Eolian System, Middle Jurassic Entrada Sandstone, Eastern Utah: Unpublished Ph.D. Dissertation, The University of Texas at Austin, 105pp.

Crabaugh, M., and Kocurek, G., 1993, Entrada Sandstone: An example of a wet aeolian system, *in* K. Pye, ed., The Dynamics and Environmental Context of Aeolian Sedimentary Systems: Geological Society Special Publication No. 72, p. 103-126.

Crowell, J.C., and Frakes L.A., 1972, Late Paleozoic galciation: Part V, Karroo Basin, South Africa: Geological Society of America Bulletin, v. 83, p. 2887-2912.

Dickey, P.A., 1969, Increasing concentration of surface brines with depth: Chemical Geology, v. 4, p. 361-370.

Dunn, T.L., 1994, Anisotropy and spatial variation of relative permeability and lithologic character of Tensleep sandstone reservoirs in the Bighorn and Wind River basins, Wyoming: Department of Energy Contract No, DE-AC22-93BC14897: Annual Report DOE/BC/14897-6, 76 p.

Dykstra, H., and Parsons, R.L., 1950, The prediction of oil recovery by waterflood, in Secondary Recovery of Oil in the United States: American Petroleum Institute Bulletin, p. 160-74.

Freeze, R.A. and Cherry, J.A., 1979, Groundwater: Englewood Cliffs, New Jersey: Prentice Hall, 604 p.

Goggin, D.J., Chandler, M.A., Kocurek, G., Lake, L.W., 1988, Patterns of permeability in eolian deposits: Society of Petroleum Engineering, Formation Evaluation, v. 3, p. 532-534.

Hajash, A. and Chandler, G.W., 1981, An experimental investigation of high temperature interaction between seawater and rhyolite, andesite, basalt, and peridotite: Contributions to Mineralology and Petrology, v. 78, p. 240-254.

Hanshaw, B. and Back, W., 1979, Major geochemical processes in the evolution of carbonate-aquifer systems: Journal of Hydrology, v. 43, p. 287-312.

Henbest. L.G., 1954, Pennsylvanian formaminifera in Amsden Formatin and Tensleep Sandstone, Montana and Wyoming: Billings Geological Society, Fifth Annual Field Conference Guidebook, p.50-53.

Henbest, L.G., 1956, Foraminifera and correlation of the Tensleep Sandstone of Pennsylvanian age in Wyoming: Wyoming Geological Association, Eleventh Annual Field Conference Guidebook, p. 58-63.

Hoare, R.D., and Burgess J.D., 1960, Fauna from the Tensleep Sandstone in Wyoming: Journal of Paleontology, v. 34, p. 711-716.

Holm and Josendal, 1974, Mechanism of oil displacement by carbon dioxide: Journal of Petroleum Technology, v. 26, v. 1472.

Kerr, D.R., 1989, Sedimentology and Stratigraphy of Pennsylvanian and Lower Permian Strata (Upper Amsden Formation and Tensleep Sandstone) in North-Central Wyoming: Ph.D. dissertation, University of Wisconsin, Madison, 382p.

Kerr, D.R., Wheeler, D. M., Rittersbacher, D.J., and Horne J. C., 1986, Stratigraphy and sedimentology of the Tensleep Sandstone (Pennsylvanan and Permain), Bighorn Mountains, Wyoming: Wyoming Geological Association, Earth Science Bulletin, v. 19, pt. 2, p. 61-77.

Kharaka, Y.K., Gunter, W.D., Aggarwal, P.K., Perkins, E.H., and De Braal, J.D., 1988, SOLMINEQ.88: A computer program code for geochemical modeling of water-rock interactions. U.S.Geological Survey, Water Resources Investigation Report 88-4227, p.

Kocurek, G., 1981, Significance of interdune deposits and bounding surfaces in aeolian dune sands: Sedimentology, v. 28, p. 753-780.

Kocurek G., and Havholm, K., 1993, Eolian sequence stratigraphy--a conceptual framework, *in* P. Weimer and H. Posamentier, eds., Recent Advances in and Applications of Siliciclastic Sequence Stratigraphy: American Association of Petroleum Geologists Memoir 58, p. 393-409.

Mankiewicz, D., and Steidtmann, J.R., 1979, Depositional environments and diagenesis of the Tensleep Sandstone, eastern Big Horn Basin, Wyoming; *in* P. Scholle, and P. Schluger, eds., Aspects of Diagenesis: Society of Economic Paleontologists and Mineralogists Special Publication 26, p. 319-336.

Mottl M., and Holland, H.D., 1978, Chemical exchange during hydrothermal alteration of basalt by seawater: I. Experimental results for major and minor components of seawater: Geochimica et Cosmochimica Acta, v. 42, p. 1105-1115.

Parrish, J.T., and Peterson, F., 1988, Wind directions predicted from global circulation models and wind directions determined from eolian sandstones of the western United States - A comparison, *in* G. Kocurek, ed., Late Paleozoic and Mesozoic Eolian Deposits of the Western Interior of the United States: Sedimentary Geology, v. 56, p. 261-282.

Peterson, F., 1988, Pennsylvanian to Jurassic eolian transportation systems in the western United States; *in* G. Kocurek, ed., Late Paleozoic and Mesozoic Eolian Deposits of the Western Interior of the United States: Sedimentary Geology, v. 56, v. 207-260.

Pittman, E.D., 1992, Artifact porosity in thin sections of sandstones: Journal of Sedimentary Geology, v. 62, p. 734-737.

Plummer, L.N., Busby, J.F., Lee, R.W., and Hanshaw, B.B., 1990, Geochemical modeling of the Madison aquifer in parts of Montana, Wyoming, and South Dakota: Water Resources Research, v. 26, p. 1981-2014.

Ramsbottom, W.H.C., 1979, Rates of transgression and regression in the Carboniferous of NW Europe: Geological Society of London Journal, v. 136, p. 147-153.

Rhodes, F.H.T., 1963, Conodonts from the topmost Tensleep Sandstone of the eastern Big Horn Mountains, Wyoming: Journal of Paleontology, v. 37, p. 401-408.

Rubin, D.M., and Hunter, R.,E., 1982, Bedform climbing in theory and nature: Sedimentology, v. 29, p. 121-138.

Rubin, D.M. and Hunter, R.E., 1983, Reconstructing bedform assemblages from compound cross-bedding, *in* M.E. Brookfield and T.S. Ahlbrandt, eds., Eolian Sediments and Processes: Developments in Sedimentology, v. 38, p. 407-427.

Rubin, D.M., 1987, Cross-bedding, bedforms and paleocurrents: Society of Economic Paleontologists and Mineralogists, Concepts in Geology, v. 1, 187p.

Sakai, H., and Matsubaya, O., 1974, Isotope geochemistry of the thermal waters from Japan and its bearing on the Kuroko ore solutions. Economic Geology, v. 69, p. 974-991.

Scotese, C.R., Bamback, R.K., and Barton, C., Van der Voo, R. and Ziegler, A.M., 1979, Paleozoic base maps: Journal of Geology, v. 87, p.217-277.

Seyfried, W.E., and Bischoff, J.L., 1981, Experimental seawater-basalt interaction at 300°C, 500 bars, chemical exchange, secondary mineral formation and implications for the transport of heavy metals: Geochimica et Cosmochimica Acta, v. 45, p. 123-134.

Shiraki, R., Sakai, H., Endoh, M., and Kishima, N., 1987, Experimental studies on rhyolite- and andesite-seawater interactions at 300°C and 1000 bars: Geochemical Journal, v. 21, p. 139-148.

Sholkovitz, E., 1973, Interstitial water chemistry of the Santa Barbara basin sediments: Geochimica et Cosmochimica Acta, v. 37, p. 2043-2073.

Smith, L.K., 1993, Aspects of oilfield water chemistry: Part A. Induced diagenetic alteration, and Part B. The effect of organic alkalinity on cation ratios. Ph.D. dissertation, University of Wyoming, Laramie, 290 p.

Stiles, W.E., 1949, Use of permeability distributions in water-flood calculations: American Institute of Mining Engineers Transactions, v. 186, p. 9-13.

Thomas, C.E., Mahoney, C.F., and Winter, G.W., 1992, Chapter 44: Water-injection pressure maintenance and waterflood processes. *in* Petroleum Engineering Handbook: Society of Petroleum Engineers.

Todd, T. W. (1964) Petrology of Pennsylvanian rocks, Bighorn Basin, Wyoming. Bulletin, American Association of Petroleum Geologists. v. 48, p.1063-1090.

Vail, P.R., Mitchum, R.M., and Thompson III, S., 1977, Seisic stratigraphy and global changes of sea level, Part 4 - Global cycles of relative changes of sea level, *in* C.E Payton, ed., Seismic Stratigraphy- Applications to Hydrocarbon Exploration; American Assocation of Petroleum Geologists, p. 83-97.

Verville, G.J., 1957, Wolfcampian fusulinids from the Tensleep Sanstone in the Big Horn Mountains, Wyomings: Journal of Paleontology, v. 31, p. 349-352.

Verville, G.J., Sanderson, G.A., and Rea, B.D., 1970, Missourian fusulinids from the Tensleep Sanstone, Bighorn Mountains, Wyoming: Journal of Paleontology, v. 44, p. 478-479.

Wanless, H.R., and Shepard, F.P., 1936, Sea level and climatic changes related to late Paleozoic cycles; Geological Society of America Bulletin, v. 47, p. 1176-1206.

Wheeler, D., 1986, Stratigraphy and sedimentology of the Tensleep Sandstone, southeast Bighorn Basin, Wyoming; Unpublished Masters Thesis, Colorado School of Mines, Golden, 169 p.

Willhite, G. P., 1986, Waterflooding: Society of Petroleum Engineers Textbook Series, v. 3, 326 p.

☆U.S. GOVERNMENT PRINTING OFFICE: 1996 - 760-032/40001